Julius-Maximilians-Universität Würzburg

Lehrstuhl für Physik und Astronomie

Masterarbeit

vorgelegt von
Michael Kreter

Search for neutrinos from flaring blazars
- A time dependent point source analysis -

Verantwortlicher Hochschullehrer:	Prof. Dr. Matthias Kadler
Zweitgutachter:	Prof. Dr. Gisela Anton
Abgabetermin:	21. August 2015

Abstract

Active galactic nuclei (AGN) are one of the most fascinating astrophysical objects in the universe. While they emit photons over the whole electromagnetic spectrum, AGN are also promising candidates to be the sources of the recently discovered high-energy extraterrestrial neutrino flux.

ANTARES (*Astronomy with a Neutrino Telescope and Abyss Environment RESearch*) is a large volume deep-sea water Cherenkov telescope in the Mediterranean Sea located $42\,\mathrm{km}$ from Toulon in France. Is is optimized for the detection of muons from high-energetic neutrinos, which can be produced in the atmosphere or by extraterrestrial accelerators. As the ANTARES detector is optimized for up-going muons, this means that it is "looking downwards" through the Earth. Thus, neutrino telescopes located on the northern hemisphere are most sensitive to the observation of southern astronomical objects.

The TANAMI program (*Tracking Active Galactic Nuclei with Austral Milliarcsecond Interferometry*) is a multiwavelength program to monitor relativistic jets in active galactic nuclei of the southern sky. It consists of a radio Very Long Baseline Interferometry (VLBI) monitoring program, as well as a high-energy multiwavelength program. As theoretical models predict a correlation of γ-ray and neutrino emission generated in the same processes within an AGN jet, the performance of a multi-messenger analysis using γ-ray light-curves could result in a significant decrease of background in a neutrino point source analysis and thus increase the sensitivity of an analysis to a neutrino signal from AGN.

Within this thesis, I perform a time dependent neutrino point source search analysis using the ANTARES neutrino telescope. An unbinned maximum likelihood method is applied to maximize the probability of a neutrino detection from TANAMI sources. *Fermi* γ-ray light-curves are used for an effective neutrino background rejection, which results in a significant gain in sensitivity. The usage of different Monte Carlo generation methods leads to a precise description of environmental conditions in the deep sea.

Zusammenfassung

Aktive Galaxienkerne (AGN) sind bei weitem eines der interessantesten astronomischen Objekte im Universum. AGN emittieren Photonen innerhalb des gesamten elektromagnetischen Spektrums. Zudem sind sie vielversprechende Kandidaten zur Erklärung des kürzlich detektierten hochenergetischen Neutrino Flusses. Zur Detektion eines extra-terrestrischen Neutrino Signals werden große Neutrinoteleskope benötigt.

ANTARES (*Astronomy with a Neutrino Telescope and Abyss Environment RESearch*) ist ein Cherenkov Detektor, welcher sich im Mittelmeer vor der Küste von Toulon befindet. Dieser ist auf die Detektion hochenergetischer Myonen optimiert. Diese Teilchen können durch die Wechselwirkung hochenergetischer Neutrinos erzeugt werden. Da sich ANTARES auf der nördlichen Halbkugel befindet, ist es für Neutrinos des Südhimmels optimiert, da diese die Erde durchlaufen.

TANAMI (Tracking Active Galactic Nuclei with Austral Milliarcsecond Interferometry) ist ein multiwellenlängen Programm zur Beobachtung relativistischer Jets aktiver Galaxienkerne des Südhimmels. Verschiedene theoretische Modelle gehen von einer simultanen Erzeugung hochenergetischer Photonen sowie Neutrinos innerhalb eines AGN-Jets aus. Eine Multi-Messenger Analyse, basierend auf der Korrelation von ANTARES Daten und *Fermi* γ-ray Lichtkurven, könnte zu einer massiven Unterdrückung des Neutrino Untergrundes führen. Dies würde in einer gesteigerten Sensitivität einer Neutrino Punktquellensuche resultieren.

In dieser Arbeit befasse ich mich mit einer zeitabhängigen Neutrino Punktquellensuche mithilfe des ANTARES Teleskops. Mit TANAMI Quellen führe ich eine "unbinned maximum likelihood method" durch, um die Wahrscheinlichkeit einer Neutrinodetektion zu steigern. Durch die Verwendung von *Fermi* Lichtkurven ist eine signifikante Unterdrückung des Untergrundes möglich. Die Verwendung unterschiedlicher Monte Carlo Methoden führt zu einer präzisen Beschreibung variabler Umweltbedingungen in der Tiefsee.

Contents

1 Introduction

Using tiny particles to discover hidden secrets of the universe is the idea of neutrino astronomy. Recent results by the IceCube Collaboration (IceCube Collaboration 2013) have shown evidence for a high-energy extraterrestrial neutrino signal. Two PeV neutrino events have been detected which can not be explained by a pure atmospheric hypothesis. Nevertheless, no clear extragalactic neutrino point source has been identified so far.

Neutrino astronomy deals with questions starting from the very beginning of our universe, over the search of dark matter, to the sources of high-energy cosmic rays. It combines classical astronomy with high-energy particle physics, leading to a more precise description of fundamental physical concepts in the universe.

Neutrinos have first been postulated by Wolfgang Pauli, who studied β-decays. While within the standard model of particle physics, neutrinos are assumed to be massless. It was the discovery of neutrino oscillation from solar neutrinos that gave evidence for neutrino masses (Fukuda et al. 2001).

As neutrinos are only affected by the weak force, they do not interact with e.g. dust layers or get absorbed like photons. Thus, they can escape from even dense environments in the universe. Neutrinos are non-charged particles, so they are not deflected by intergalactic magnetic fields and travel on straight trajectories from their origin. Because of the unique properties of neutrinos, they are perfect messengers for the study of fundamental physical concepts in astronomical objects. Due to their small interaction cross sections, neutrino astronomy is mainly limited by statistics.

As has been shown in Krauß et al. 2014, Active galactic nuclei (AGN) are a promising candidate for the sources of the high-energy extraterrestrial neutrino flux.

While the presence of the high-energy peak in the spectral energy distribution (SED) of AGN is believed to be dominated by inverse compton scattering, hadronic models (Mannheim 1993) provide an alternative explanation for the generation of high-energy γ-rays.

ANTARES (Astronomy with a Neutrino Telescope and Abyss Environment RESearch) is a large volume deep-sea water Cherenkov telescope in the Mediterranean Sea located 42 km from Toulon in France (Ageron et al. 2011). In order to reduce background from neutrinos generated in the atmosphere, ANTARES is optimized for up-going muons. This means, the detector is "looking downwards" through the Earth, most sensitive to observe southern astronomical objects.

The multiwavelength monitoring program TANAMI (Tracking Active Galactic Nuclei with Austral Milliarcsecond Interferometry) is monitoring relativistic jets in AGN of the southern sky (Ojha & Kadler, 2010; Kadler et al., 2015). While TANAMI consists of a radio Very Long Baseline Interferometry (VLBI) monitoring program, it also performs a high-energy lightcurve monitoring program, using several telescopes. As ANTARES is most sensitive to the southern sky, TANAMI sources are the ideal candidates for a neutrino point source analyses.

Diffuse flux analyses as well as point source analyses have been performed with the ANTARES telescope. While the majority of analyses have to deal with an enormous amount of background (see Adrián-Martínez et al. 2012c), the assumption that neutrinos and photons are generated and reach Earth simultaneously (Mücke et al. 2003) reduces the relevant time intervals and thus the amount of background significantly.

Within this analysis, *Fermi* γ-ray light-curves are used to identify promising flaring periods of selected TANAMI sources, leading to a reduced number of time intervals and an effective background suppression. Beside that, other time dependent neutrino point search analyses have been performed within ANTARES (Adrián-Martínez et al. 2015), taking other sources distributed over the whole sky into account.

Within this thesis, I will give an overview of active galactic nuclei, as well as possible radiation processes leading to the generation of high-energy photons and neutrinos. In addition, an introduction to the TANAMI program and the ANTARES detector will be given. Afterwards, I will focus on Monte Carlo simulations and event reconstruction, as well as the source selection criteria and the different analyses steps. Finally, results of this analysis are presented and an outlook is given.

2 Active Galactic Nuclei

Active Galactic Nuclei (AGN) are among the most fascinating objects in the universe. While the term "active" refers to the inner region of a galaxy, being up to four orders of magnitude brighter then "usual" galaxies this class seems to be scarce in the universe. Only a humble fraction of 3% of all identified galaxies are known to host an AGN (Terzian et al. 1999). This inner nucleus causes a high luminosity, which cannot be explained by stellar emission from the surrounding galaxy. One characteristic feature of AGN is their ability to produce powerful, broadband emission, which can be described by a power law indicative of a non-thermal emission process. AGN can emit over the whole electromagnetic spectrum and sometimes show high variability on timescales of minutes to months.

2.1 Overview

In the following, a brief overview of the general structure of an AGN will be given. Figure 2.1 illustrates a schematic model of a radio loud AGN. If not stated explicitly, all information of this chapter are based on on the textbooks Beckmann 2012, Krolik 1999, G.B. Rybicki 1985 and Schneider 2008.

2.1.1 Supermassive-Black-Hole and Mass Accretion

An active galactic nucleus is "powered" by a *supermassive black hole* (SMBH) that is accreting matter. Accretion is nowadays the generally accepted process to convert energy, so that luminosities on the order of 10^{45} ergs^{-1} can be reached in a compact region of $< 1\text{kpc}^3$ (Shakura & Sunyaev 1973). The accretion process dominates the structure of an AGN, as it leads to orbiting of gas and dust around the SMBH. Differential velocities, that are caused by friction and turbulence of the orbiting matter cause a transport of angular momentum outwards while a stream of matter is attracted to the center of the disk. Material, which moves to the center transfers its potential energy of the gravitational field into kinetic and thermal energy.

The bolometric luminosity L of the accretion process is proportional to the accretion rate $\dot{M}$. It is limited by the Eddington Limit, which describes a hydrostatic balance of radiation pressure and gravitation. An emitting process causes a radiation pressure on in-coming matter which counteracts the accretion process. Under the assumption of a stationary accretion rate and isotropic radiation, this limit is given by the Eddington Luminosity

$$L_{\text{Edd}} = \frac{4\pi G M_\odot m_p c}{\sigma_T} \propto 1.3 \times 10^{38} \left(\frac{M}{M_\odot} \right) \frac{\text{erg}}{\text{s}} . \tag{2.1}$$

Here G stands for the gravitational constant, c for the speed of light, m_p for the mass of a proton, σ_T for the Thomson cross section, $M_\odot$ for the solar mass and M for the mass of the emitting source. It is important to point out that the Eddington approximation is only a rough estimation on the correlation between measured luminosity and the black hole mass. More precise measurements can be achieved by reverberation mapping (Peterson, 1993; Collin et al., 2006).

The concentration of matter around the SMBH forms the *accretion disk*. The spectrum of the accretion disk can be described as a black body spectrum with a radial temperature dependence. Measurements of this spectrum indicate a correlation between the activity of an AGN and the amount of accreted matter.

Close to the SMBH at distances of about 0.1 pc to 1 pc the *broad line region* (BLR) is located. Matter in this region has to be concentrated into clouds, as otherwise Thomson scattering
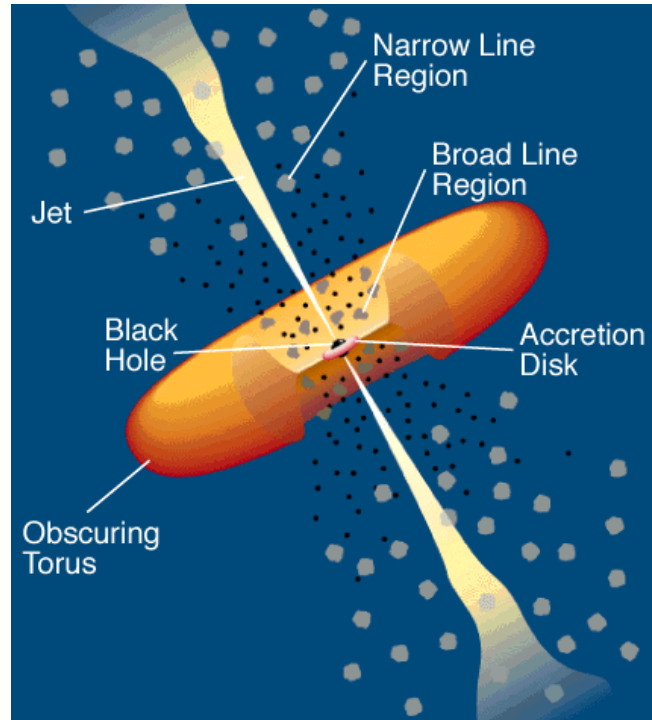
Figure 2.1: Schematic sketch of a radio loud AGN. A SMBH is accreting matter and thus forming an accretion disk. Perpendicular to that disk a relativistic particle outflow (jet) is formed. Radio-quiet AGN show no jets. Credit: Urry & Padovani 1995

would make this region optically thick. The occurrence of broad lines can be explained via a turbulent motion of the clouds and a high velocity.

At distances of about 100 pc the *narrow line region* (NLR) is characterized by the observation of narrow (forbidden) lines. The accumulation of matter here is believed to be much colder and less dense, compared to the BLR. The accretion disk is surrounded by a *dust torus*, that is able to absorb emission lines, long-wavelength radio emission and soft γ-rays.

2.1.2 Jets

In a fraction of all AGNs, perpendicular to the accretion disk collimated highly relativistic particle outflows from the nucleus, the so called *jets* are observed. These outflows can become very large, reaching up to Mpc-scales. AGN that show such a two-sided jet configuration in the radio band, where the second jet is labeled as counterjet, are known as radio-loud AGN. It is generally assumed that the two-sided configuration is valid for all AGN, while the appearance of the jet and counterjet is varying due to relativistic beaming. A morphological classification of radio-loud AGN is given by Fanaroff and Riley (Fanaroff B.L. 1974). If no jets are detected, the AGN is known as radio-quiet. Where the outflows interact with the intergalactic medium, they are decelerated and produce radio lobes at the end of the jets. Hadronic particle acceleration models predict AGN jets to be one source of cosmic ray and extragalactic neutrinos (Stecker et al. 1991). Further information on jet acceleration models can be found at Gaisser 1990.

2.2 AGN Taxonomy

During the last decades, multiwavelength observations have discovered a broad range of different AGN types. The nowadays accepted classification scheme is based on optical or radio observations, as this kind of objects have been measured first in these spectral ranges.
In the following a brief description of the most common AGN types is given. For further information see Lawrence 1987.

Seyfert galaxies: Carl Seyfert (Seyfert 1943) first discovered a class of mostly spiral galaxies, which contain a bright quasi-stellar point-like nucleus. Optical observations indicated this class of galaxies to show broad as well as narrow (forbidden) lines caused by Doppler broadening (Khachikyan É.Y. 1971). Based on their spectral properties, Seyfert galaxies have been further divided into two subclasses. While *Seyfert 1* galaxies show broad as well as narrow (forbidden) lines, *Seyfert 2* galaxies are defined by having only narrow (forbidden) lines. Seyfert galaxies played an important role in the development of the unified model, as polarized broad emission lines have been detected in Seyfert 2 galaxies (Antonucci 1985), giving first evidence of a central engine and a hidden broad line region.

Radio galaxies: Radio galaxies are classified according to their emission properties in the radio band and show a strong radio emission from the central region. Radio galaxies can be divided into *broad line radio galaxies* (BLRG) and *narrow line radio galaxies* (NLRG). A characteristic feature of radio galaxies is their extended radio emission, which can reach up to Megaparsecs away from the central nucleus.
Fanaroff & Riley (Fanaroff B.L. 1974) defined an classification scheme that is based on the radio morphology, not on the optical properties of the galaxy. *Fanaroff-Riley Typ 1* (FR1) galaxies are characterized by a dominating bright core and two jets, emanating from the core on both sides. The luminosity decreases along the jets with increasing distance. On the other hand *Fanaroff-Riley Typ 2* (FR2) galaxies are dominated by bright radio lobes and a less bright central nucleus. The luminosity increases along the jets with increasing distance to the black hole. FR2 galaxies usually show only single-side jets, which are relatively weak compared to FR1 galaxies.

Quasars: Quasars (Quasi Stellar Objects) or QSOs are strong radio sources with unresolved (star-like) optical counterparts. They are among the brightest objects and typically found at high redshifts. Quasars show broad optical emission lines and a point like morphology. Nowadays Quasars are classified as compact objects, with a Seyfert-like optical spectrum. As Quasars are not qualified according to their radio properties, both radio-loud and radio-quiet objects can be found.

Blazars: Blazars are the most luminous sources of all AGN that emit light across the whole spectrum up to the highest energies. They are found to be compact, highly variable objects, that show strong γ-ray emission. Typically their broadband spectrum is dominated by non-thermal emission, while often no optical emission lines are found. Blazars combine BL Lac objects, as well as Flat-Spectrum Radio Quasars (FSRQ). While the spectra of BL Lacs are dominated by featureless non-thermal continuum, FSRQs typically show a compact radio structure and flat radio spectra.
Blazars typically exhibit relativistic jets and show several characteristic effects. The effect of *superluminal motion* can easily be explained by a projection of a constant and finite light evolution (see Figure 2.2). Let's consider a bright feature propagating along the jet axes with velocity $\vec{v}$, which is seen under the small inclination angle ϕ. Two distinct light signals
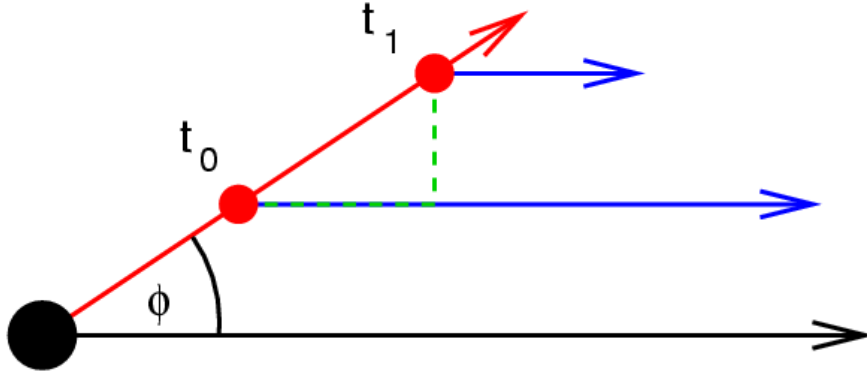
Figure 2.2: Sketch of the projection effect of superluminal motion. A bright feature propagates along the jet axes (red) with velocity $\vec{v}$. The jet is seen under the inclination angle ϕ. The observer only takes projection images of the jet. Credit: M. Kadler

are emitted from the feature at times t_0 and t_1, while propagating along the jet axes. The observer detects the signals separated by:

$$\Delta t = \left(1 - \frac{v}{c} \cos \phi\right) \Delta t_{\text{emit}} \tag{2.2}$$

where Δt_{emit} is the time interval between the emission of both light signals. If one considers the observed distance to be $\Delta x = v \Delta t_{\text{emit}} \sin \phi$, the observed velocity is given by

$$v_{\text{obs}} = \frac{v \sin \phi}{1 - \frac{v}{c} \cos \phi}. \tag{2.3}$$

As the observed velocity strongly depends on the inclination angle ϕ, this angle has to be known to derive the real velocity.

To describe the properties of blazars, further relativistic effects have to be taken into account. The Doppler factor D:

$$D = \frac{v_{\text{obs}}}{v_{\text{emit}}} = \frac{1}{1 + \frac{v_{\text{obs}}}{c} \cos \phi} \tag{2.4}$$

is an important quantity in the description of jet behavior. The effect of Doppler boosting describes the increase/decrease of an observed flux density due to an emitting feature moving at relativistic velocities close to the line of sight. It can be shown, that for a flux density $F_\nu \propto \nu^{-\alpha}$ the quantity $F_\nu \nu^3$ is Lorentz invariant (G.B. Rybicki 1985).

As mentioned before, blazars are highly variable γ-ray emitters. High energy γ-rays can either be produced by inverse compton scattering, where low-energetic photons gain energy via the scattering on highly relativistic electrons (see Sect. 3.2.2) or $p\gamma$-interactions (see Sect. 3.3).

Nevertheless, the time scales of these radiations can vary between minutes and months. This high variability indicates a compact structure of the emission region. Within the standard model of AGN (see Sect. 2.3), blazars are believed to be seen under a small inclination angle with a jet orientated in the light of sight. These assumption, as a consequence would explain the point like morphology and short time variability of blazars.

Blazars typically show two broad peaks in their spectral energy distribution (SED). Figure 2.3 displays the SED of a typical blazar sample. While the low-energy peak can be explained

by synchrotron radiation (see Sect. 3.2.1), the second peak at higher energies is assumed to be dominated by inverse compton scattering. The exact processes responsible for the high-energy peak are yet to be explored, but hadronic models (Mannheim 1993) could provide an alternative approach.

Studies of a complete blazar SED sample (Fossati et al. 1997) found a correlation between the shape of the SED and the source luminosity (see Figure 2.3). Less-luminous sources tend to have a higher low-energy peak than brighter sources. Furthermore, a correlation between both peaks has been found, resulting in a shifting in frequency of the double-humped shape. This shifting seems to depend on the source bolometric luminosity, where a brighter source is linked to a smaller low-energy peak frequency.

The exact mechanisms responsible for the blazar sequence are still a matter of actual research, assuming e.g. two distinct source populations (Meyer et al. 2011).
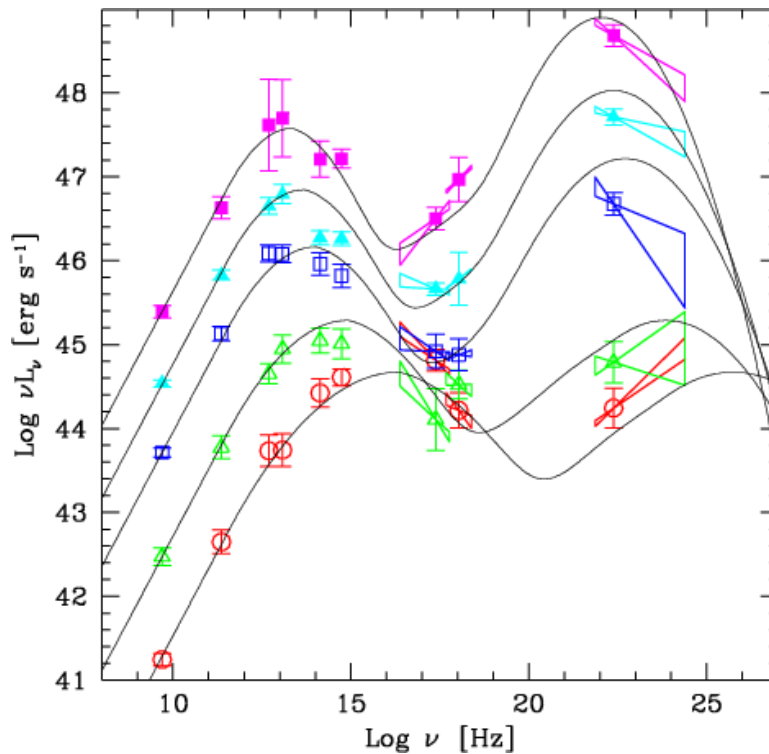
Figure 2.3: Blazar spectral energy distribution (SED) and blazar sequence. A correlated between bolometric luminosities and peak frequencies can be seen.
Credit: Fossati et al. 1997

2.3 A Unified Model

Antonucci 1985, Lawrence 1987 and Urry & Padovani 1995 first suggested that all the different object classes of AGN consists of the same components. To explain the broad variety of observations within this *unified model*, a rotational symmetry and projection effect was assumed.

The subdivision within this model is based on the inclination angle, which is the angle between the line of sight and the rotation axis of the accretion disk or the jet axes. Figure 2.4 visualizes the different AGN classes. While all radio loud AGN consist of the standard components like *supermassive black hole, accretion disk, broad line emission region, narrow line emission region, dust torus and jets*, not all of these features are detectable at any viewing angle. In
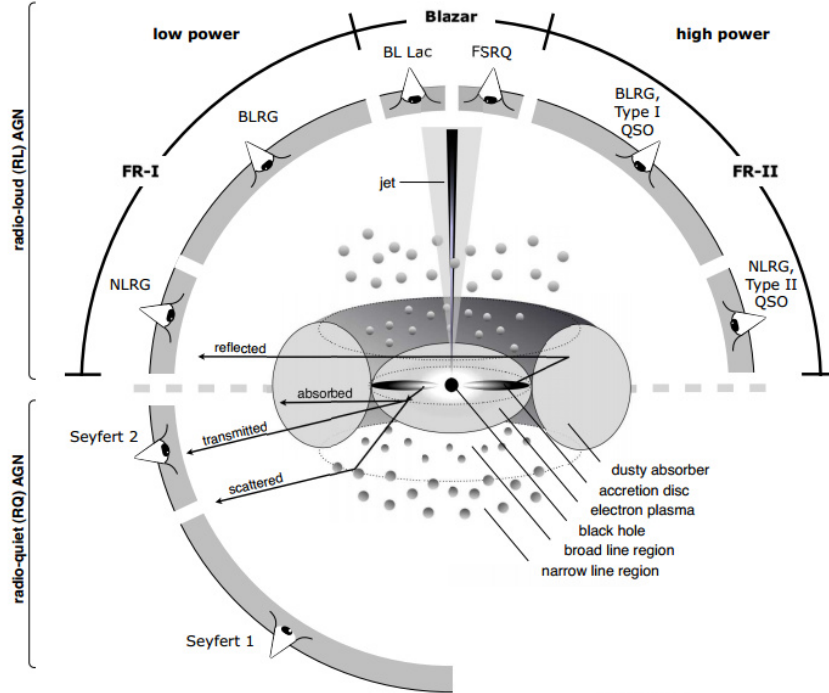
Figure 2.4: Schematic sketch of the unification model of Urry & Padovani. According to
the inclination angle and source luminosity, an AGN consisting of the standard
components like SMBH, accretion disk and jets different classes of objects can be
defined.
Credit: Beckmann 2012

type 2 AGN, which are seen at large inclination angles, broad line emission is absorbed by
the dust torus. This torus is assumed to lie in the plane of the accretion disc and consists of
colder material than the inner parts of the disc. Evidence for the obscuring torus have been
given by polarization measurements (Bianchi et al. 2012).
On the other hand, type 1 AGN are observed at small inclination angles, therefore the inner
region, which is responsible for the broad emission lines is detectable.
For extreme small viewing angles ($\leq 5°$), blazars are believed to be dominated by boosting
effects of the highly relativistic outflows. This boosting can affect the whole detected system,
as it can outshine the other components so that only a bright, star-like object can be seen. In
addition to the inclination angle, radio loudness and source luminosity are used as classifica-
tion parameters. Seyfert 1 and Seyfert 2 galaxies are characteristic candidates for radio-quiet
sources. If jets are present, these galaxies are classified as radio-loud AGN. The amount of
radio emission is correlated to the viewing angle and can be explained by relativistic beaming
effects and Doppler-boosting (see Sect. 2.2). A summary of the unification scheme of Urry &
Padovani can be seen in Table 1. Although this scheme describes the general accepted model
of AGN unification, recent observations indicate that extensions may be needed (Bianchi et al.
2012).

	radio-quiet	**radio-loud**
Type 1	Seyfert 1 radio-quiet quasar	BLRG radio-loud quasar (type 1)
Type 2	Seyfert 2 radio-quiet quasar	NLRG (FR I & II) radio-loud quasar (type 2)

Table 1: Unification scheme after Urry & Padovani 1995.
The inclination angle increases from type 1 to type 2 galaxies.

3 Theoretical Background

This chapter will give an overview of the physical concepts of AGN radiation processes as well as accretion of matter and neutrino generation models. If not labeled explicitly all the information of this chapter are based on the textbooks Beckmann 2012, G.B. Rybicki 1985, Schneider 2008 , Ajit K. Kembhavi 1999 and Stanev 2010.

3.1 Accretion of Matter

The basic mechanism underlaying the AGN central engine and producing luminosities of about $10^{45}\,\mathrm{ergs^{-1}}$ in a compact region of $< 1\mathrm{kpc}^3$ is accretion of matter. Matter falls into a central supermassive black hole, converting gravitational potential energy into radiation. The simplest model one could consider is a spherically symmetric constant accretion flow. This will result in an accretion rate:

$$\dot{M} = \pi r^2 \rho v \tag{3.1}$$

where ρ is the density of the in-falling matter, v its velocity and r the distance from the black hole. This basic model of accretion is generally known as *Bondi - Hoyle accretion.* Under the assumption that the accretion capture radius is correlated to the escape velocity V of a particle at a distance $R = \frac{2GM_{BH}}{V^2}$, the accretion rate becomes:

$$\dot{M} = \frac{4\pi\rho G^2 M_{BH}^2}{V^3} \tag{3.2}$$

Accretion onto a compact object is limited by radiation pressure generated by the in-falling matter. By equating the pressure gradient from in-falling matter

$$\frac{dP}{dr} = \frac{-GM\rho}{r^2} \tag{3.3}$$

with the radiation pressure

$$\frac{dP}{dr} = \frac{-\sigma_T \rho}{m_p c} \frac{L}{4\pi r^2} \tag{3.4}$$

the *Eddington Luminosity* (equation 2.1) is derived.

It is important to point out that the most basic *Bondi - Hoyle accretion* is unlikely to play a major role in powering of AGN. The reason is, that the conversion efficiency from gravitational potential energy into radiation energy is low. While radiation in the accretion flow is based on viscous thermal heating, the basic problem of pure Bondi accretion (which assumes the absence of angular momentum) is, that matter is falling into the central engine before radiating its thermal energy. However, extensions to this quite basic model like assuming a viscous dissipation of the accretion flow are give by Shakura & Sunyaev 1973 or Balbus & Hawley 1991.

3.2 Radiation processes in AGN

3.2.1 Synchrotron Radiation

When charged particles get accelerated by the Lorentz force in a magnetic field $\vec{B}$, they emit radiation. The radiation of non-relativistic particles is known as *cyclotron radiation*, while for relativistic velocties this process is called *synchrotron radiation*.
The Lorentz force is given by:

$$m\gamma\dot{\vec{v}} = \frac{q}{c}\left(\vec{v} \times \vec{B}\right) \tag{3.5}$$

where m is the mass of the electron, $\gamma = \left(1 - \frac{v^2}{c^2}\right)^{-1/2}$ the Lorentz factor, $\vec{v}$ the velocity of the charged particle, $\vec{B}$ the magnetic field and q the charge of the particle. Figure 3.1 illustrates the emission of synchrotron radiation cones of a charged particle moving on a helical path through a magnetic field. A characteristic frequency of the helical motion is the gyration frequency ω_g

$$\omega_g = \frac{qB}{\gamma mc} \tag{3.6}$$

where B and v stand for the absolute value of the vectors $\left(\text{e.g. } \left|\vec{B}\right|\right)$. Synchrotron emission shows a dipole characteristic in the electron rest frame.
The total energy loss of a charged particle getting accelerated in a magnetic field is:

$$\frac{dE}{dt} = -\frac{e^4 B^2}{6\pi\epsilon_0 m^2 c}\frac{v^2}{c^2}\gamma^2 \sin^2\alpha \tag{3.7}$$

where α is the *pitch angle* between the vectors of velocity and the magnetic field. Finally, the radiation power of an electron in a magnetic filed is given as:

$$P = \frac{4}{3}\sigma_T c\beta^2\gamma^2\frac{B^2}{8\pi} \tag{3.8}$$

where $\beta = \frac{v}{c}$. For high relativistic electrons, one can generally assume $\beta \approx 1$. Using the relation $E = \gamma mc^2$ one can show that the radiated energy of a single particle (equation 3.7) is
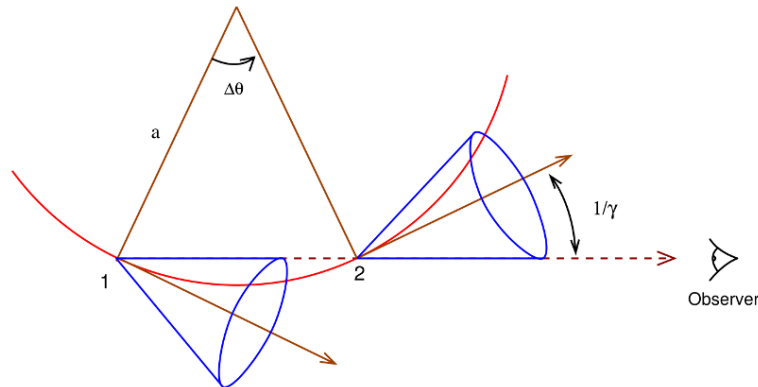
Figure 3.1: Charged particle on its helical path through a magnetic field is emitting synchrotron radiation in a cone.
Credit: G.B. Rybicki 1985
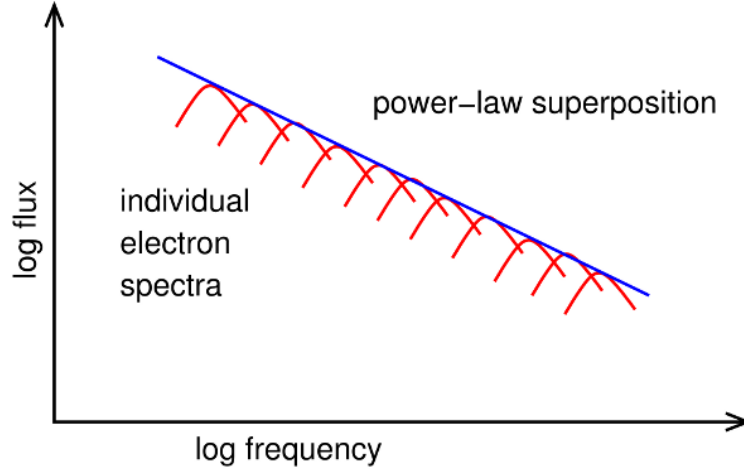
Figure 3.2: Superposition of single electron synchrotron spectra, resulting in a power law ($P_\nu \propto \nu^\alpha$). Credit: Shu 1991

proportional to m^{-4}, so synchrotron radiation of a massive particle is either low or negligible.

Non-thermal synchrotron radiation can be explained by electrons, following a power law spectrum according to:

$$n(\lambda)d\lambda = n_0\gamma^{-p}d\lambda \tag{3.9}$$

where $n(\lambda)$ is a non-thermal electron distribution and p the particle distribution index.
The total emission power is achieved by integrating over the electron distribution n

$$P_\nu = \int_1^\infty P_\nu(\gamma)n(\gamma)d\gamma. \tag{3.10}$$

This equation shows that the integral of an electron power law distribution is again a power law (see Figure 3.2):

$$P_\nu \propto \nu^\alpha \tag{3.11}$$

$$\text{where } \alpha = -\frac{p-1}{2}. \tag{3.12}$$

At low energies, *synchrotron self-absorption* becomes important. A photon emitted by a low energetic electron can again be absorbed by the same electron. Therefore, this changes the proportionality of the total emitted power for low frequencies:

$$P_\nu \propto B^{-\frac{1}{2}}\nu^{\frac{5}{2}} \tag{3.13}$$

Finally, synchrotron self-absorption is characterized by the self-absorption coefficient a_S

$$a_S \propto \nu^{-\frac{p+4}{2}} \tag{3.14}$$

To understand this broken power-law spectrum of synchrotron radiation the optical depth τ_ν has to be defined:

$$\tau_\nu = \int_{s_0}^s a_S(s_1)ds_1 \tag{3.15}$$

where ds_1 is an infinitesimal distance the electron travels. If $\tau_\nu > 1$ the medium is called *optical thick*, while for $\tau_\nu < 1$ it is *optical thin*. The frequency near $\tau_\nu = 1$ is called turnover frequency ν_t, as it defines the kink of the broken power law spectrum:

$$P_\nu \propto \nu^{\frac{5}{2}} \quad \text{for} \quad \nu < \nu_t, \tag{3.16}$$

and

$$P_\nu \propto \nu^{-\frac{p-1}{2}} \quad \text{for} \quad \nu > \nu_t. \tag{3.17}$$

Please note that the slope of the optical thick part of the spectrum does not depend on the energy distribution of the electron, while the optical thin part is a function of the particle distribution index p.

3.2.2 Inverse Compton Scattering

At non-relativistic energies, Compton scattering transfers energy form the photon to the electron. In the case of highly relativistic electrons, *inverse Compton scattering* can lead to an opposite effect: a low frequency photon gets a gain in energy. In this case, the Thomson cross section can be applied.
If one assumes the laboratory frame to be L and the rest frame of the electron to to be $L´$, the energy of the photon in the rest frame of the electron will be small, compared to the rest energy of the electron $h\nu´ \ll mc^2$. Thus, the energy of the photon in $L´$ is given by the relativistic Doppler shift formula:

$$h\nu´ = \gamma h\nu \left(1 + \frac{v_e}{c} \cos(\theta) \right) \tag{3.18}$$

where v_e is the velocity of the relativistic electron and θ is the angle between the direction of the photon and the incoming electron in the laboratory frame L. In the electrons rest frame $L´$, this angle becomes small according to

$$\sin \theta´ = \frac{\sin \theta}{\gamma \left(1 + \frac{v_e}{c} \cos(\theta) \right)}. \tag{3.19}$$

As already mentioned, inverse Compton scattering can be treated as Thomson scattering in the electron rest frame, so one has an elastic scattering with $E_2´ \approx E_1´$. Transferring this into the laboratory frame reads:

$$E_2 \approx \gamma^2 E_1. \tag{3.20}$$

The maximum energy gain of a photon is achieved by calculating the energy conservation in the laboratory frame L:

$$E_2 \le E_1 + \gamma m_e c^2 \tag{3.21}$$

where the maximum change in the photon frequency is:

$$\Delta \nu \le \gamma m_e c^2 h^{-1} \tag{3.22}$$

Finally, the total power of the inverse Compton scattering (also called the Luminosity L_{IC}) logically depends on the density of photons n_{ph} available for scattering:

$$L_{\text{IC}} \propto n_{\text{ph}} \gamma^2 E_1. \tag{3.23}$$

If one then considers a more complex and detailed description (compared to equation 3.23), which includes the energy density function of the photon field U_{ph}, as well as a relativistic Doppler shift, the luminosity becomes:

$$L_{\mathrm{IC}} = \frac{4}{3}\frac{v_e^2}{c}\sigma_T\gamma^2 U_{\mathrm{ph}}. \tag{3.24}$$

In case the condition $h\nu' \ll mc^2$ is not fulfilled in the electron rest frame, the assumed elastic Thomson scattering can no longer be assumed. Consequently, Klein-Nishina effects have to be considered, which include a dependency on the photon energy and scattering angle. Further information about this extended model can be found at Blumenthal & Gould 1970.

3.3 High-energy photons and neutrinos from hadronic processes

High energetic cosmic rays have been known to exist for more than a century, while their origin is still as mystery. Since charged particles are deflected in magnetic fields, their arrival direction does not have to be correlated to their source, except at the very highest energies. On the other hand neutrinos only couple weakly, so they most likely do not scatter on their way to Earth and propagate on straight trajectories.

Neutrinos can be generated in any region of the cosmos, where protons are accelerated to high energies. This acceleration can happen at shock fronts, moving through the interstellar medium. At these shock fronts, particles are accelerated by the so called *first order Fermi mechanism*. In this theory, the particle gains a constant fraction of energy by passing through the shock front. To achieve high energies the particle has to repeat the transition many times. If a charged particle is accelerated by getting deflected (multiple times) at irregularities of a magnetic field inside a moving plasma, this is described by the *second order Fermi mechanism*. For more information about Fermi acceleration please refer to Gaisser 1990.

The accelerated protons now can interact with the ambient matter or radiation fields, producing neutrinos in hadronic showers such as:

$$p + nucleus \rightarrow \pi + X \quad (\pi = \pi^{\pm}, \pi^0) \tag{3.25}$$

$$p + \gamma \rightarrow \Delta^+ \rightarrow \begin{cases} \pi^0 + p \\ \pi^+ + n. \end{cases} \tag{3.26}$$

The resulting decay products further decay into:

$$\pi^0 \rightarrow \gamma + \gamma \tag{3.27}$$

$$\pi^{\pm} \rightarrow \mu^{\pm} + \nu_{\mu} \;(\text{ or } \bar{\nu}_{\mu}) \tag{3.28}$$

$$\mu^+ \rightarrow e^+ + \bar{\nu}_{\mu} + \nu_e \tag{3.29}$$

$$\mu^- \rightarrow e^- + \nu_{\mu} + \bar{\nu}_e. \tag{3.30}$$

Eventually neutrinos are generated via the decay of charged pions. With a probability of more then 99.9%, charged pions decay into muons and (anti)muon-neutrinos. These muons may further decay into electrons, producing two more neutrinos. To estimate the contribution of generated neutrinos, the ratio of of cross sections $\sigma_{\pi^0 p}$ and $\sigma_{\pi^+ n}$ has to be calculated (B. Povh 1999). If one assumes a system $|JM\rangle$ of coupled isospins j_1 and j_2, the probability for the states $|j_1 m_1\rangle$ and $|j_2 m_2\rangle$ is given by the square of the Clebsch Gordan coefficients. For the decay of the Δ^+ this reads:

$$\frac{\Delta^+ \rightarrow \pi^0 + p}{\Delta^+ \rightarrow \pi^+ + n} = 2. \tag{3.31}$$

So neutral pions are two times more likely then charged pions (assuming only decays of leading order). Proton interactions with the surrounding matter lead to a fraction of generated pions of:

$$p + p \rightarrow \begin{cases} p + p + \pi^0 & \text{fraction } \frac{2}{3} \\ p + n + \pi^+ & \text{fraction } \frac{1}{3}. \end{cases} \tag{3.32}$$

If the proton interacts with a neutron n instead of a proton p, negative charged pions π^- as well can be produced. At high energies charged kaons (K^+, K^-) start to contribute to the neutrino production, decaying either to charged pions (28%) or directly into muons (64%). In addition, next to leading order decays contribute to the neutrino production channels. For more information please refer to B. Povh 1999.

3.3.1 Neutrino generation in AGN jets

The kinematic threshold for the process of equation 3.26 is mainly influenced by the photon energies in the radiation field. For ambient UV photons, the threshold is in the range of several PeV. For photons generated by synchrotron radiation, which has a broad spectrum, the threshold is smeared out to much lower energies. This is an important point for neutrino astronomy (Katz & Spiering 2012).
Unfortunately, TeV photons can't just be produced via the decay of a neutral pion, but also by inverse Compton scattering. Most of the measured TeV γ-ray spectra can be explained by inverse Compton scattering. This kind of models are known as *leptonic models*. In a more realistic case, both leptons and hadrons will be accelerated in a jet. Figure 3.3 visualizes possible interactions inside an AGN jet, leading to the production of high-energy photons and neutrinos. While photons produced by synchrotron radiation of electrons serves as target for inverse Compton scattering and proton collision, the occurrence of high energetic PeV photons can't be explained.
An observation of PeV γ-rays produced via the decay of neutral pions therefore would be a proof for the acceleration of protons in so called *hadronic models* and a hint for possible neutrino point sources.
For more details about radiation processes in AGN see Section 3.2. Blazars in addition show high variabilities, leading to an increase of their detected flux by orders of magnitude within hours. For more details about extraterrestrial neutrino production and their accelerators please refer to Katz & Spiering 2012.

3.3.2 Lepto-hadronic models

If both leptons and hadrons are accelerated within an AGN jet, these kind of models are referred to as *lepto-hadronic models* (Stanev 2010).
In these models, the region of proton acceleration and neutrino production is within the AGN jet. The main neutrino generation process is photoproduction on internal synchrotron photons or the thermal UV photon background of the accretion disk. Because of the low matter density in the jet, the proton energy-loss on *pp* interactions and thus the neutrino production from this process is small. The high-energy neutrino spectrum will follow the shape of the accelerated proton spectrum, usually showing a power law index of 2 before interaction (Mannheim 1993). Purely hadronic models are not able to model the short time variability of TeV γ-ray sources. The reason is, that protons have to be accelerated to high energies, whereas this acceleration takes longer than the time interval of the variability. The solution for this problem is the use of lepto-hadronic models, e.g. Mücke et al. 2003, where soft electrons and protons are accelerated in the jet.
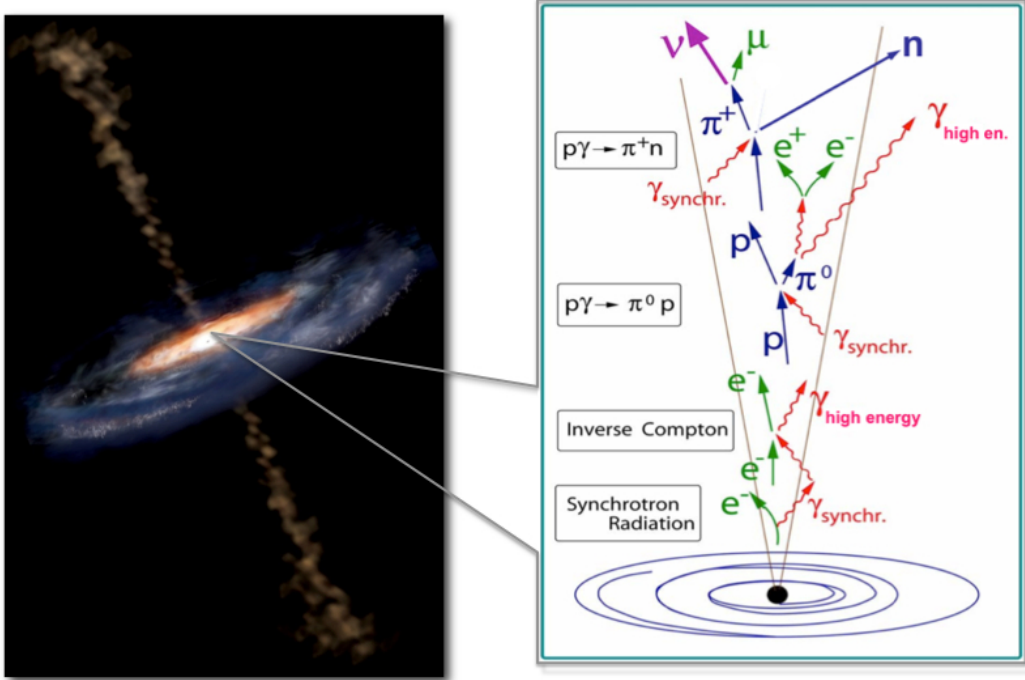
Figure 3.3: Left: Artist's view of an AGN, Right: Processes in a jet, generating high energetic photons and neutrinos. Credit: Simonnet, A., Sonoma State University and Katz & Spiering 2012

A jet, however, is a non stationary object. The plasma is injected as separate blobs, moving along the jet axis with relativistic velocities (see Figure 3.4). Electrons within these blobs emit synchrotron radiation, which serves as target for proton interaction as well as photon-photon pair production. To accelerate protons to energies above the photo-pion production threshold, fields of the order of 10 G would be necessary. With increasing magnetic field strength, the importance of synchrotron radiation increases. The increasing photon energy density leads to an increase of muon synchrotron radiation and pion cascades due the growing efficiency of meson production.

Variability, however can be influenced by an increase in the accretion rate, injecting a shock to propagate along the jet axis. As the shock propagates through the highly magnetized plasma of the jet, electrons tend to produce more synchrotron radiation due to an increase in electron density. The appearance of a fresh relativistic shock at a non-turbulent position of the jet plasma leads to an increase of the acceleration efficiency. Because of this gain in efficiency, the synchrotron and γ-ray production threshold is shifted towards higher energies.

The neutrino spectrum mainly depends on the proton spectrum and the density of target photons. If one assumes electrons and protons to be accelerated simultaneous, the energy spectrum of injected protons would follow an E^{-2} spectrum. Due to photohadronic interactions with synchrotron photons, this spectrum is flattened to a E^{-1} spectrum. Therefore, also the spectrum of the neutrinos is expected to follow a E^{-1} spectrum. For more details about this model please refer to Mannheim et al. 2001.

Neutrinos are the only particles, which could escape the strong conditions within an AGN jet. After escaping, they have to travel long trajectories through the universe, without interacting with other particles. Adiabatic losses of the trajectories for neutrino energies due to the

expansion of the Universe can be estimated according to:

$$E(z) = E_0 \cdot (1 + z) \tag{3.33}$$

where E_0 is the neutrino energy after leaving the jet and z is the redshift. This estimation is valid for adiabatic losses due to the expansion of the Universe, while it gives very poor results for photopion losses.

Finally, one can conclude that whenever high energetic photons are observed in a lepto-hadronic model, high energetic neutrinos will be produced as well.
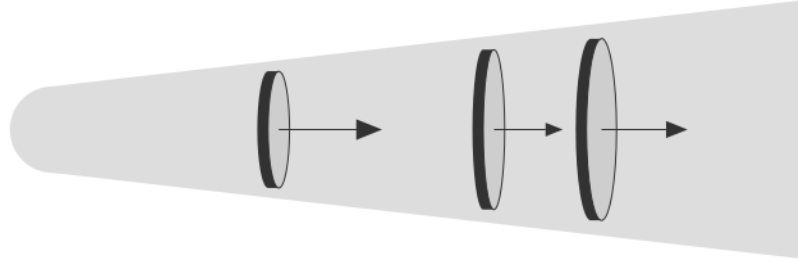
Figure 3.4: Schematic sketch of the acceleration within an AGN jet. The plasma is injected as separated blobs, moving along the jet axes with relativistic velocities. The length of the arrows however indicate their velocities.
Credit: Stanev 2010; based on Blandford & Königl 1979

4 A Multi-Messenger Approach

In the following, a brief overview of the *multi-messenger* approach used in this thesis will be given. More detailed information about the TANAMI program can be found in Ojha & Kadler 2010 or Kadler et al. 2015. For details about the ANTARES detector please refer to Ageron et al. 2011.

4.1 The TANAMI program

The TANAMI program (Tracking Active Galactic Nuclei with Austral Milliarcsecond Interferometry) is a multiwavelength program to monitor relativistic jets in active galactic nuclei of the southern sky.[1] It includes a radio Very Long Baseline Interferometry (VLBI) monitoring program, targeting the parsec-scale structures of radio-loud AGN. TANAMI is also performing radio spectral and light-curve monitoring programs with ATCA and the Ceduna telescope. Finally, TANAMI collects high-energy multiwavelength data with REM, *Swift, XMM-Newton, Suzaku, INTEGRAL, Fermi*/LAT and other telescopes. Currently, TANAMI is monitoring about 90 sources, most of them are blazars.

An overview of the TANAMI telescopes and a γ-ray skymap, including TANAMI associated
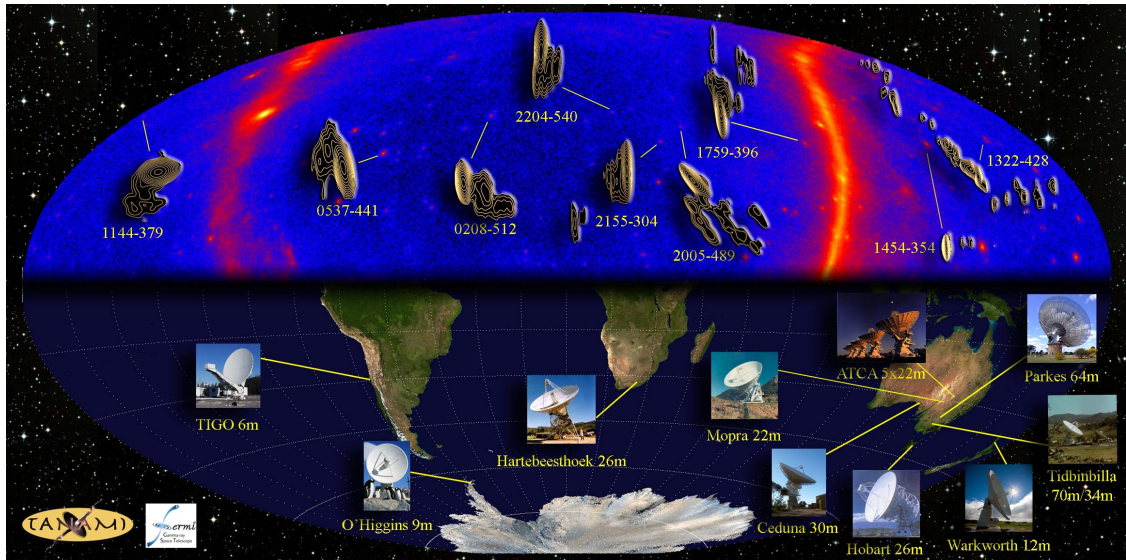
Figure 4.1: Collage to illustrate the basic concept of the TANAMI program. Top: Southern-Hemisphere γ-ray skymap observed by *Fermi*/LAT (in celestial coordinates). One can see the Milky Way and a couple of extragalactic point sources, which are associated with radio observations by TANAMI sources. Bottom: TANAMI telescopes located on Earth's Southern Hemisphere. Credit: M. Kadler

sources can be seen in Fig. 4.1. The heart of the TANAMI program are dual-frequency (8.4 GHz and 22.3 GHz) VLBI observations of AGN ($< -30°$ declination) of the southern sky. These observations are performed about every 4 months, providing resolution in the mas-scale. High resolutions in this range can only be achieved with VLBI. One of the core properties of a radio telescope is the angular resolution. According to the Rayleigh criterion this reads:

$$\sin(\alpha) \approx 1.22\frac{\lambda}{d}.$$ (4.1)

---

[1] http://www.pulsar.sternwarte.uni-erlangen.de/tanami

Here, α is the angular resolution, λ the wavelength at which the observation is performed and d the diameter of the radio telescope. In the case of VLBI, d corresponds to the baseline of the array, which is the longest distance between two telescopes. For the use of VLBI, it is important for all telescopes to observe simultaneously.

Roughly spoken, a VLBI image is generated by measuring the source brightness, in the first step using each telescope individually. Due to Earth's rotation and a discrepancy in the distance to the source for each individual antenna, an instrumental delay has to be corrected. Then, the VLBI image is obtained by applying a deconvolution of a complex visibility function in the so called (u,v)-plane. For further information please refer to Burke & Graham-Smith 2009.

The TANAMI array consists of the Australian Long Baseline Array (LBA), including telescopes at NASA's Deep Space Network (DSN), as well as the South-African Hartebeeshoeck antenna. In 2009, the German Antarctic Receiving Station (GARS), and the Transportable Integrated Geodetic Observatory (TIGO) joined the program. Since 2011, the Warkworth, Katherine and Yarragadee antennas are part of the TANAMI array.

4.1.1 The *Fermi* γ-ray space telescope

The *Fermi* satellite, formerly *Gamma-ray Large Area Telescope* (GLAST) was launched by NASA on June 11th, 2008. The instruments on board of *Fermi* are the Large Area Telescope (LAT) and the Gamma-ray Burst Monitor (GBM).

LAT is a high-energy γ-ray pair-conversion telescope, which provides a large field of view of about 2.4 *sr*. This large field of view allows LAT to scan the whole sky in less then 3 hours. The detection process is based on pair production. An incoming γ-ray photon converts into an e^+e^--pair, producing a track and energy deposit in the detector. The direction reconstruction is based on a segmentation of the electromagnetic calorimeter, which stops the electron - positron pairs and therefore provides a precise energy measurement. To distinguish between detections caused by γ-rays and cosmic rays, an anticoincidence shield is located at the entrance of the detector. This provides a reasonable background rejection.

Due to the wide field of view (about 20% of the whole sky) *Fermi*/LAT is able to operate in an all-sky mode, monitoring each point in the sky approximately every three hours. This monitoring strategy results in a nearly uniform coverage of the full sky and a continuous source monitoring. Continuous light-curves are generated by separating the obtained data into timebins and performing a maximum-likelihood method for each detected photon. For more information please refer to Atwood et al. 2009.

Fermi/LAT data is extracted by using a maximum-likelihood method. In a first step, a region of interest around the expected source position has to be defined. This region has to be large enough to distinguish between different sources in order to perform a reasonable background rejection but also small enough to facilitate a reasonable computing time. In the next step, a source model is folded with the detector response.

The maximum-likelihood method offers a probability for a source detection under the assumption of a background-only detection. The quantity for this kind of statistical test is the test statistic TS:

$$TS = 2Log\left[\frac{L_{max}}{L_{max,0}}\right] \tag{4.2}$$

The test statistic connects the likelihood L_{max}, which assumes the detection of a source at the appropriate positron with the likelihood $L_{max,0}$ which presumes the background-only

hypothesis. This method is based on the work of Cash 1979.

4.2 ANTARES a deep sea neutrino telescope

ANTARES (*Astronomy with a Neutrino Telescope and Abyss Environment RESearch*) is a large volume deep-sea water Cherenkov telescope in the Mediterranean Sea located 42 km from Toulon in France at $42°47.935'$ N, $6°09.942'$ E. ANTARES is optimized for the detection of muons from high-energetic neutrinos, which can be produced in the atmosphere or by extraterrestrial accelerators. In the field of neutrino astronomy, the primary purpose of ANTARES is the detection of extraterrestrial neutrinos.

4.2.1 Neutrino interactions before detection

As neutrinos are only weakly interacting fermions, they won't couple to electromagnetic fields and therefore won't get deflected like photons. The majority of neutrinos traverses the universe and the Earth without interacting. Therefore, the only chance of detecting a neutrino signal is in the case of an interaction, via its secondary particles. For that reason, the neutrino has to interact with matter of the detector and produce secondary particles, which do at least couple electromagnetically. Figure 4.2 displays possible neutrino interactions near the detector.
The chance for a neutrino interaction depends on the neutrino cross section.
According to Gandhi et al. 1996, the differential cross section for a deep inelastic scattering on a nucleus is

$$\frac{d^2\sigma}{dxdy} = \frac{2G_F^2 M E_\nu}{\pi} \left(\frac{M_W^2}{Q^2 + M_W^2} \right)^2 \left[xq(x, Q^2) + x\overline{q}(x, Q^2)(1 - y)^2 \right], \qquad (4.3)$$

where G_F is the Fermi constant, M the mass of the target nucleon, M_W the mass of the W-boson, E_ν the energy of the incident neutrino, $-Q^2$ the invariant momentum transfer between the incident neutrino and the outgoing muon, $x = \frac{Q^2}{2M\nu}$ and, $y = \frac{\nu}{E_\nu}$ are the Bjorken scaling variables, $\nu = E_\nu - E_\mu$ is the energy loss in the lab (target) frame, and E_μ the energy of the outgoing muon.
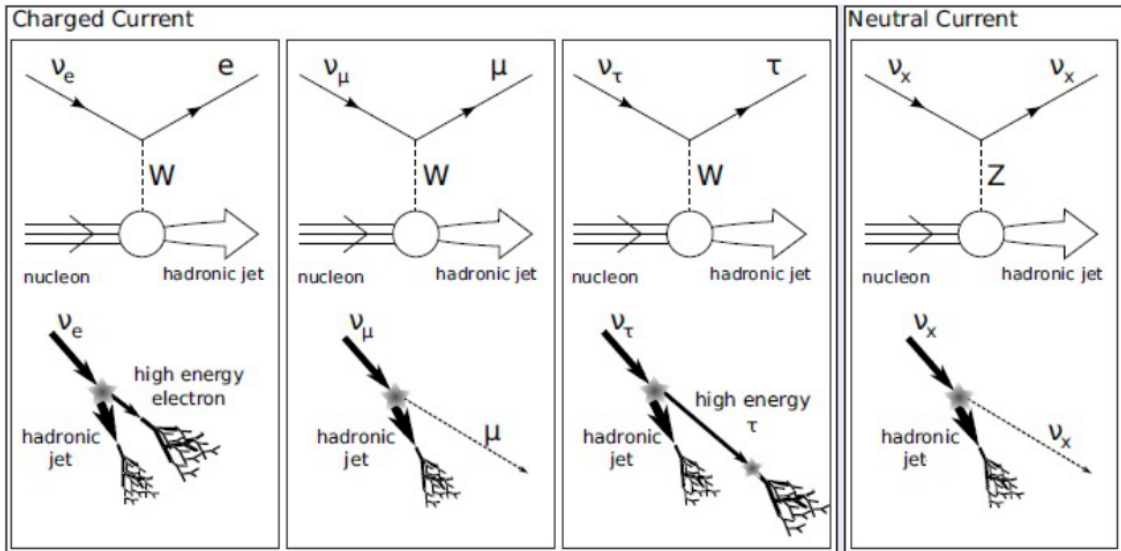
Figure 4.2: Possible neutrino interactions before a detection. Top: Feynman diagrams. Bottom: Schematic view. Credit: Abreu 2011

The quark distribution functions can be written as

$$q(x,Q^2) = \frac{1}{2}(u_v(x,Q^2) + d_v(x,Q^2)) + \frac{1}{2}(u_s(x,Q^2) + d_s(x,Q^2)) + s_s(x,Q^2) + b_s(x,Q^2)$$
(4.4)

and

$$\bar{q}(x,Q^2) = \frac{1}{2}(u_s(x,Q^2) + d_s(x,Q^2)) + c_s(x,Q^2) + t_s(x,Q^2),$$
(4.5)

where *u, d, c, s, t, b* denote on the different quark flavors in a proton and the indexes *v, s* label valence and sea contributions. Figure 4.3 shows the total cross section for the process discussed in this chapter, as well as the contributions from the neutral current and charged current interactions. For neutrino energies in the range of 10^6 GeV $< E_\nu < 10^{12}$ GeV, equation 4.3 can be approximated by a simple power law according to:

$$\sigma_{CC}(\nu N) = 2.69 \times 10^{-36} cm^2 \left(\frac{E_\nu}{1\ \text{GeV}}\right)^{0.402}$$
(4.6)

$$\sigma_{NC}(\nu N) = 1.06 \times 10^{-36} cm^2 \left(\frac{E_\nu}{1\ \text{GeV}}\right)^{0.408}$$
(4.7)

$$\sigma_{CC}(\bar{\nu} N) = 2.53 \times 10^{-36} cm^2 \left(\frac{E_\nu}{1\ \text{GeV}}\right)^{0.404}$$
(4.8)

$$\sigma_{NC}(\bar{\nu} N) = 0.98 \times 10^{-36} cm^2 \left(\frac{E_\nu}{1\ \text{GeV}}\right)^{0.410}.$$
(4.9)

For more detailed information, e.g. for the calculation of the cross section for low energetic atmospheric neutrinos, please refer to Formaggio & Zeller 2012.

4.2.2 Neutrino detection principle

As neutrinos only interact weakly, their detection is much difficult compared to photons. Their detection principle is based on secondary particles after the neutrino interaction. Figure 4.4 illustrates the basic concept of a neutrino detection.

An incoming high energetic neutrino interacts with the material surrounding the detector and produces (in the case of a ν_μ) a muon. As the muon (on average) gets most of the energy of the neutrino, its velocity will be faster than the speed of light in sea water (see Adrián-Martínez et al. 2012a). Therefore, the muon emits Cherenkov light while traveling through sea water, which is detected by an array of light sensors. In sea water the original spectrum of Cherenkov light is attenuated, ending up with light in the wavelength range from 350 nm to 500 nm. Due to the small fraction of energy deposits of the muon, the interaction vertex could be kilometers away from the detector.

While this description only focuses on track-like muon events, other flavors could also be observed. For example, electron neutrinos ν_e produce electromagnetic showers (the cascade results from Bremsstrahlung and pair production) which are detected with lower efficiency and less angular resolution because of the shorter path of the resulting leptons.

The Cherenkov light in the end is detected by a set of photomultipliers contained in a glass spheres, the so-called optical modules (OMs). The OMs are arranged on flexible lines anchored to the seabed, forming a matrix of optical light detectors. To reconstruct a muon track, the arrival time of Cherenkov photons on each OM is measured, while a precise positioning with an accuracy better than 10 cm via acoustic measurements of the OMs is required (Ageron et al., 2011; Adrián-Martínez et al., 2012b).
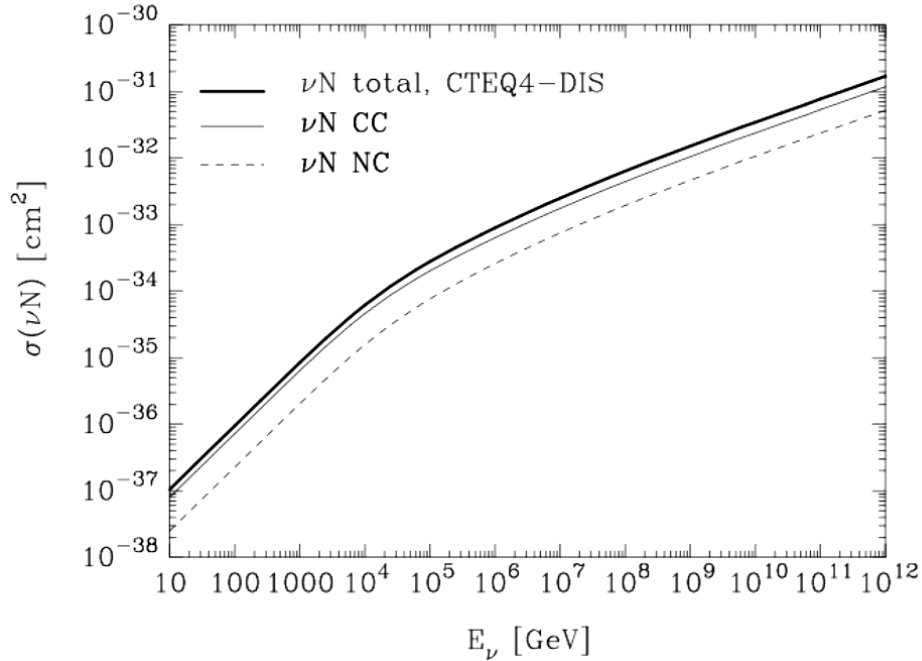
Figure 4.3: Neutrino cross section for the process of equation 4.3. Dotted line: neutral current contribution $\sigma(\nu N \to \nu + X)$. Thin line: charged current contribution $\sigma(\nu N \to \mu^- + X)$. Thick line: total (charged-current plus neutral-current) cross section. Gandhi et al. 1996

4.2.2.1 Event signature

Beside the expected extraterrestrial neutrino signal, other sources can leave an event signature within the detector. Air showers, produced by the interaction of cosmic rays with the Earth's atmosphere, generate so-called *atmospheric muons* and *atmospheric neutrinos*. These muons could penetrate the atmosphere and even several kilometers of sea water, finally entering the detector from above. As shown in Figure 4.5, down-going muons ($\cos(\theta) > 0$) are the dominant part of detected events and exceed neutrino induced up-going muons by several orders of magnitude.

On the other hand, up-going muons ($\cos(\theta) < 0$) can only be produced by neutrinos which travel in almost the same direction. Figure 4.6 displays the angular deviation between the direction of the neutrino and the muon. The major impact is caused by the neutrino-muon interaction (shown in white).

Most of the detected up-going muons originate from up-going atmospheric neutrinos, and this kind of interaction represents an irreducible background. In order to reduce background, neutrino telescopes are optimized for up-going muons, which means that they are "looking downwards" through the Earth. So if a neutrino telescope is located on the northern hemisphere, it is optimized to observe southern objects.

An extraterrestrial neutrino flux can only be detected at high energies, as for these energies the atmospheric neutrino flux is lower due to the steep energy spectrum of $\frac{dN}{dE} \propto E^{-3.6}$ (Carminati 2007).
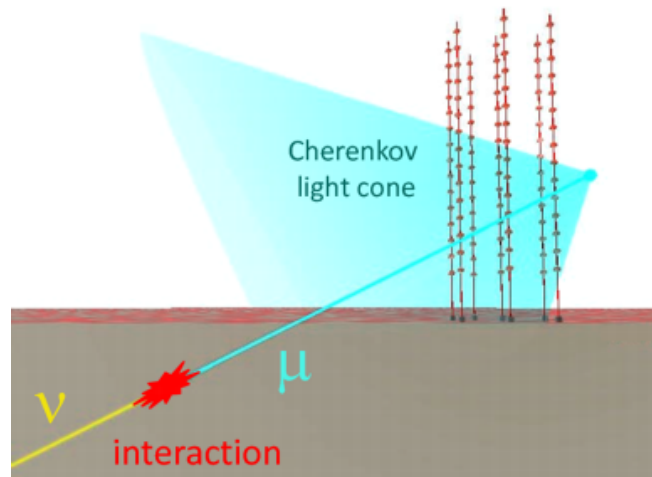
Figure 4.4: Detection principle of a high energetic neutrino. The incoming neutrino interacts with the material surrounding the detector and produces a muon. The muon emits Cherenkov light while traveling through sea water. The Cherenkov light (350 nm $< \lambda <$ 500 nm) is finally detected by an array of light sensors.
Credit: Ageron et al. 2011
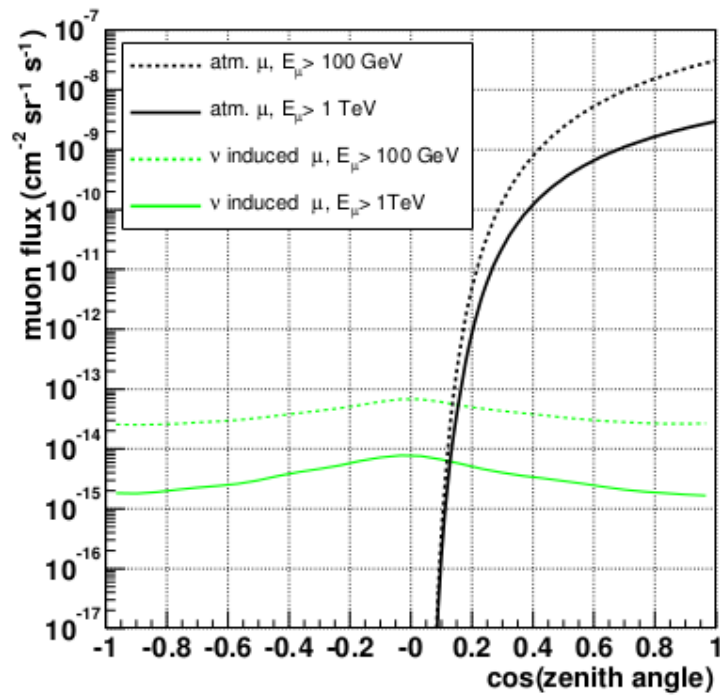
Figure 4.5: Muon background at 2.1 km depth indicated due to atmospheric muons and atmospheric neutrinos in two different energy ranges. While the neutrino indicated muon flux does not depend on the zenith angle, muons produced in the atmosphere can be rejected by choosing $\cos(\theta) < 0$.
Credit: Okada 1994
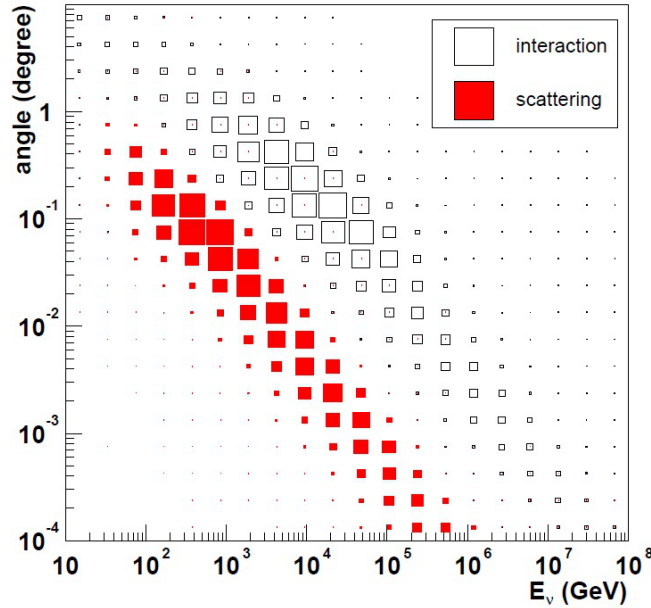
Figure 4.6: Angular deviation between the direction of the neutrino and the muon, depending on the neutrino energy. White: Deviation caused by the neutrino-muon interaction. Red: Deviation caused by multiple scattering off atomic nuclei. Credit: Heijboer 2004

4.2.2.2 Cherenkov radiation:

Cherenkov radiation is emitted whenever a highly energetic charged particle traverses a transparent medium with a velocity faster then the speed of light in the medium. In an atomic description, the charged particle causes a local disturbance at the surrounding atoms, which leads to an electric polarization of the medium. While the particle travels faster than the medium needs to elastically relax, this causes the medium to radiate a coherent shock wave. The Cherenkov radiation is emitted with a characteristic angle with respect to the track of the particle which reads:

$$\theta_C = \arccos\left(\frac{1}{\beta n}\right), \tag{4.10}$$

where θ_C is the so called Cherenkov angle, β is the velocity of the particle with respect to the speed of light in vacuum c and n is the refractive index of the medium. If one assumes a high relativistic muon ($\beta \approx 1$) traveling through sea water ($n \approx 1.35$), the Cherenkov angle becomes:

$$\theta_C \approx 42.5°. \tag{4.11}$$

The number of Cherenkov photons emitted at a specific wavelength λ is given by the Frank-Tamm formula:

$$\frac{d^2 N_\gamma}{dx d\lambda} = \frac{2\pi\alpha}{\lambda^2}\left(1 - \frac{1}{\beta^2 n^2}\right), \tag{4.12}$$

where α is the fine structure constant. This means that at characteristic wavelengths of 300 nm $< \lambda <$ 600 nm, about 3×10^4 Cherenkov photons are emitted during 1 m of track.

While propagating to the OMs, the photons could either be absorbed or scattered. The number of photons at a given distance r from the track is:

$$N(r) = N_0 \cdot \frac{1}{r} \cdot e^{\frac{-r}{\lambda_{abs}}}, \tag{4.13}$$

where $r = \frac{k}{\sin(\theta)}$ is the length of the photon path,

λ_{abs} is the effective absorption length

N_0 the number of photons produced at the track, and

k the wave vector of the photon.

The arrival time t at an optical module depends on the travel time of the muon, as well as the propagation time of the Cherenkov photon and is given as:

$$t = t_\mu + t_\gamma = \left[t_0 + \frac{1}{v} \left(l - \frac{k}{\tan(\theta)} \right) \right] + \left[\frac{1}{v_g} \left(\frac{k}{\sin(\theta)} \right) \right], \tag{4.14}$$

where t_0 is the time till the generation of the muon,

k the shortest distance between the muon track and the OM,

l the distance on the muon track to the position k,

v the velocity of the muon, and

v_g the group velocity of photons in water.

In order to enable a detection of Cherenkov photons in the OMs, the propagation path of the photons has to be shorter than the absorption length.
For more detailed information please refer to Kremers et al. 2009, Jackson 1998 and Leo 1994.

4.2.3 The ANTARES detector

The ANTARES detector is located in the Mediterranean Sea about 42 km from Toulon in France at about 2.5 km below sea level. It consists of an three-dimensional array of 885 optical sensors, arranged on 12 vertical strings. Each string of about 480 m hosts 75 optical modules (OMs), which are grouped to 25 storeys equipped with three OMs. The spacing between storeys is 14.5 m, while the strings are separated by about 70 m. Therefore, the total sensitive volume is about 0.03 km^3. An additional string, the instrumentation line (IL07), carries devices for environmental monitoring. The detector as displayed in Figure 4.7 was completed in May 2008. The strings are fixed to the sea floor with an anchor and kept tight using buoys at the top of each string. Electro-optical cables connect the strings at the seabed with a junction box, which provides the main cable to shore.
The main detection components are the optical modules, which are made of a 17-inch glass sphere, housing a 10-inch photomultiplier. Beside the photomultiplier, the glass sphere contains the electronics for the high-voltage power supply of the photomultiplier as well as an optical gel for the position stabilization of its components. The photomultiplier is surrounded by a mu-metal cage, which provides a shielding against the Earth's magnetic field of approximately 46 μT. The photomultipliers provide an intrinsic timing resolution (transit time spread) of about $\sigma_{\mathrm{TTS}} = 1.3$ ns, thus a precise measurement of the Cherenkov photon arrival time is possible. In order to reject the background of down-going atmospheric muons or neutrinos, the OMs are oriented looking downwards at an angle of 45°. Figure 4.8 shows an artist's view of an ANTARES storey, and one of the OMs is highlighted as a photograph.

In order to provide track reconstruction precisions of about 0.4° for energies above 1 TeV, a reasonable detector calibration has to be done.

To calibrate for time delays caused by different optical path lengths between the OMs of each string, the relative time needed to reach different LCMs is measured. To take the high-voltage dependent transit time of the photomultiplier into account, flashing a Light Emitting Diode (LED) located inside the optical module is used for calibration.

For the time calibration of the whole detector, two more devices are employed. Each string contains four storeys, which are equipped with an additional optical beacon. These beacons can be used to emit a set of pulsed LED flashes, which illuminate a given number of OMs on the strings. For a more global flashing, a powerful pulsed laser is located at the seabed, which is able to illuminate a large part of the detector. A timing precision of 0.5 ns is achieved, which is compatible with the requirements.

The correlation between a measured hit in the photomultipliers and the corresponding time information is done via a time to voltage converter (TVC). By using time ranges of 25 ns, the TVC measures the arrival time of the photomultiplier signal within this time range with a precision of about 2 ns.

The amplitude of the signal is measured using the amplitude to voltage converter (AVC). Due to the low number of photons reaching the OMs during normal data tacking, the amplitude is expressed in units of photoelectrons (pe). After a threshold of 0.3 pe is reached, the AVC starts to integrate the signal for a time range of 25 ns. After this time range it takes 250 ns for the AVC to recover. In order to minimize deadtime, two AVCs are installed.

One of the major problems for a precise positioning is the flexibility of the single lines. Their position and orientation is influenced by the sea current and therefore has to be monitored continuously. For that purpose, a compass and tiltmeter measuring the orientation of each storey is used. The relative orientation of the lines with respect to each other is measured via an acoustic detection system.
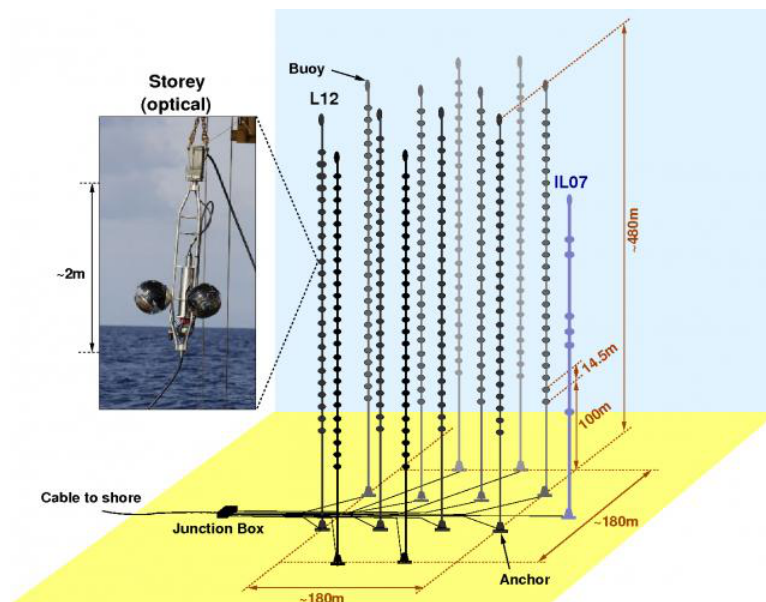
Figure 4.7: Schematic view of the ANTARES detector. Shown are the 12 strings which carry 25 detection storeys with 885 optical sensors in total, as well as the instrumentation line. An inset of a storey, carrying three optical modules is given as a photograph. Credit: Katz & Spiering 2012
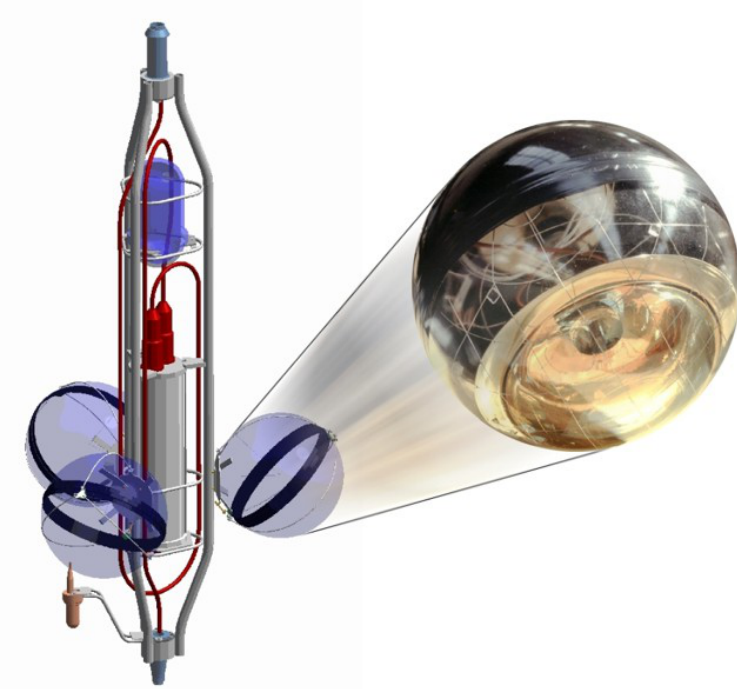
Figure 4.8: An artist's view of an ANTARES storey, hosting three optical modules shown as a photograph. Credit: Folger 2014

Hydrophones employed on five storeys per string measure the running times of acoustic pulses generated at transmitters on the sea floor. In addition, AMADEUS is used to study the feasibility of an acoustic neutrino detection. More detailed information can be found at Ageron et al. 2011 or Katz & Spiering 2012.

4.2.4 Trigger algorithms

Due to the huge amount of detected hits sent to shore, trigger algorithms are necessary to identify potential physics events. In order to distinguish between hits caused by optical background (see Sect. 4.2.5), specific assumptions on physical hits have to be made. As optical background mostly causes hits from just one photon, a charge threshold of typically three pe has to be reached. The second assumption on physical hits is that they have to fulfill a time correlation, as they all have to occur in a time range of 20 ns on the same storey. Hits which fulfill at least one of the criteria are referred to as *level 1 (L1)* hits. Within these L1 hits, different trigger algorithms search for correlations.

4.2.4.1 3N Trigger:

This kind of trigger is the standard muon trigger and can be used either in 3D or 1D. L1 hits are chosen that satisfy the causality criterion

$$|t_i - t_j| \leq \frac{|d_{ij}|}{c_{water}}, \tag{4.15}$$

where t_i and t_j are the arrival times of the hits i and j, d_{ij} is the distance between the two hits and c_{water} is the speed of light in sea water. Only hits that are consistent with this criteria can be connected to a muon from a certain direction.

4.2.4.2 2T3 Trigger:

This trigger searches for L1 hit coincidences in two adjacent storeys with a time window of 100 ns (*T2 trigger)*), or in two next-to-adjacent storeys with a time window of 100 ns or 200 ns (*T3 trigger)*).

4.2.4.3 GC Trigger:

This direction dependent trigger searches for L1 hit coincidences from the direction of the galactic center, with an amplitude threshold of 0.3 pe.

Different triggers can be combined and used in parallel. A sub-sample of L1 hits that fulfill a specified trigger cluster is referred to as *L2* hits. Data loss is prevented by adding a time window of 2.2 μs before the first and after the last trigger cluster hit that fulfilled the selected trigger. This time range corresponds to the time needed for a photon to traverse the complete detector. All hits within this time window are defined as one `event`.
Depending on the data taking conditions (i.e. current optical rates, run setup), the choice of the trigger setup varies. All triggered events during a given time period are saved in *runs*. The current data tacking policy prescribes to perform data tacking as long as possible, only limited by a maximum run length of 12 h or a maximum run size of 8 GB. Then, a new run starts. A more detailed discussion is available in Ageron et al. 2011.

4.2.5 Background sources

As astrophysical neutrino events are rare, a detailed understanding of possible background sources is required. In the deep sea ANTARES experiment, there are two major types of background.

4.2.5.1 Optical background

The decay of the radioactive isotope Potassium (^{40}K) produces electrons with an energy of 1.3 MeV. As the neutrino detection threshold of the OMs is about $10 - 100$ GeV, this decay causes a statistical noise of photo electrons with a rate of about 30 kHz (deVries Uiterweerd 2007). In addition, bioluminescent organisms, such as bacteria, plankton, or shrimps produce photons mostly for the purpose of communication or attracting prey. While the decay of ^{40}K produces a steady background, bioluminescence can be highly variable. Figure 4.9 shows the baseline of optical rates for the whole detector in a time window of 4 years with a two week binning. A periodic increase in bioluminescence activity can be seen, mostly influenced by the annual fluctuations of biological population in the deep sea. Furthermore, the amount of generated photons by bioluminescent lifeforms is highly correlated with the sea current. This could indicate that bacteria tend to glow more in movement, or that an increase in nourishment transport leads to an increase in bacteria population. To account for different data taking conditions, data quality parameters have been defined (see Sect. 5.4).

4.2.5.2 Atmospheric background

Secondary particles produced in interactions of cosmic rays in the Earth's atmosphere can reach the detector and leave a characteristic event signature. In an analysis focusing on ν_μ events, muons produced in the atmosphere (so called *atmospheric muons*) are the majority of triggered background events. While the instrumental volume is penetrated by neutrinos from all directions, atmospheric muons can only reach the detector from above (see Figure 4.5).

Therefore, a cut on the reconstructed zenith angle is used to reject most of the atmospheric muons. A small fraction of muons coming from above is mis-reconstructed as tracks coming from below and hence classified as physics events. A cut on the reconstructed energy of the muon (see Sect. 5.3) serves as parameter to get rid of this kind of background events.

Neutrinos produced in the atmosphere (so called *atmospheric neutrinos*) are able to cross the Earth and enter the detector volume from below, leaving a correctly reconstructed upgoing track. This kind of background again can only be reduced by applying a cut on the reconstructed energy.

For a more detailed discussion please see deVries Uiterweerd 2007.
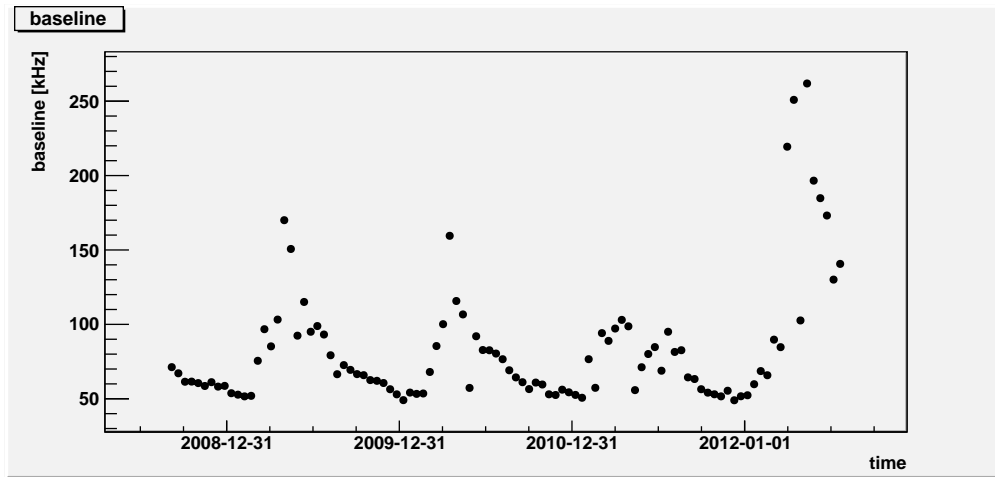
Figure 4.9: Baseline of optical rates in the deep sea. A periodic increase in bioluminescence activity can be seen, which is correlated to the biological population in the deep sea. The optical rate of one point is averaged over a time period of two weeks.

5 Simulation and Reconstruction

Due to highly variable background conditions in the deep sea (see Sect. 4.2.5) a detailed understanding of the underlying processes and the detector (see Sect. 4.2.3) has to be achieved. In this chapter, an overview of simulation and reconstruction methods used in this analysis will be given, together with a Data Monte Carlo comparison.

5.1 Run by Run Monte Carlo

The major purpose of the Run by Run Monte Carlo (rbrMC) is to model the expected data as accurately as possible. Due to highly variable background conditions in the deep sea, this kind of simulation is optimized on a per-run level in order to represent changing environmental conditions. The simulation is based on a chain of simulation steps like event generation, light propagation, detector response and event reconstruction. In the following, a summary of each individual step is given, while more detailed information can be found in Rivière 2012.

5.1.1 Event generation using GENHEN

GENHEN (GENerator of High Energy Neutrinos) is the ANTARES software package to simulate neutrino interactions. It is the first stage in the chain of rbrMC generation. While GENHEN is generating interactions in a specific generation volume, its size strongly depends on the neutrino energy, as well as the flavour or interaction type. ν_e and ν_μ events are generated using the LEPTO package (Ingelman et al. 1997), which provides a good accuracy of about 5% even for high energies. LEPTO, however is based on the deep inelastic scattering described in Sect. 4.2.1.

A neutrino event generated with GENHEN contains the trajectory of the neutrino itself, as well as all long-living secondary particles of the first generation. While neutrinos are generated following a power law energy spectrum, the used spectral index varies between $\gamma = 1$ and $\gamma = 2$ depending on the type of event. An event weighting procedure, however allows to re-weight the generated events to any kind of desired energy spectrum. Parameters included in the resulting weighting factor are the interaction cross sections and the transmission probability of neutrinos through the Earth. The generated flux of neutrinos Φ_ν per energy dE_ν, steradian dS and time dt can be calculated according to:

$$\frac{d\Phi_\nu}{dE_\nu dS dt} = g_1 \cdot g_2 \cdot g_3, \tag{5.1}$$

where the factors on the right hand site of the equation are:

- g_1: distribution of interacting neutrinos, which is directly dependent on the desired energy spectrum.

- g_2: depends on the interaction cross section and target nucleon density.

- g_3: depends on the inverse transmission probability through Earth.

Finally, the simulated flux has to be normalized with the desired flux defined in equation 5.1, resulting in the multiplication with to so called *generated weight* ω_2

$$\omega_2 = \left(\frac{d\Phi_\nu}{dE_\nu dS dt} \right)^{-1} \tag{5.2}$$

For the present analysis the desired flux is expected to follow an E^{-1} energy spectrum, within a range of 10^2 to 10^8 GeV.

5.1.2 Cherenkov light generation

The output of the GENHEN package (see Sect. 5.1.1) serves as input for the *KM3* program, which simulates the generation of Cherenkov photons from muon tracks using previously built photon tables. Afterwards, the propagation and hit generation at the OMs is simulated. All long-living particles are tracked, while the water properties (like density, pressure) are fixed for the experimental site.

Photon tables have to be used as simplification, as a detailed simulation of the Cherenkov photon generation and propagation for every single photon simply is impossible. The KM3 script consists of three subprograms:

- GEN:
  The package GEN generates photon fields at various distances from the muon track.

- HIT:
  The package HIT transforms the photon fields generated by GEN into hit probability distributions and builds the photon tables.

- KM3MC: The package KM3MC is the end of this simulation chain. It uses the hit probability distributions generated by HIT, together with a geometrical description of the detector to simulate the detector response to the passage of high-energy muons.

At the end of this simulation chain, the detector response to Cherenkov photons, emitted on a high energetic muon track has been simulated. For more details about the KM3 package please refer to S. Navas 2011.

5.1.3 Trigger Efficiency

The final step of the simulation procedure is the generation of events from Cherenkov photons arriving at the OMs. This is done by the *Trigger Efficiency* program. This is the point where different run setups and environmental conditions are taken into account, as until now the same simulation was used for each run.

Variable environmental conditions are considered by simulating a random noise for each OM, which is correlated to the measured optical rates. By this method, not just fluctuations in the baseline are considered but also local bioluminescent bursts. Time and charge uncertainties of the photomultipliers have been implemented by a Gaussian smearing.

Finally, the same triggers are applied that already have been used during data taking. For more details about the Trigger Efficiency program please see Jong 2009.

5.1.4 Monte Carlo file selection

After the production of the Run by Run Monte Carlo simulation the interesting parts for this analysis have to be selected. Table 2 lists the used parts of the rbrMC with their specific energy range. An extra low energy bin (named _x_ for "extra") was added in rbrMC v2.2. Please notice that ν_e and $\bar{\nu}_e$ files are not considered for high energies. These files could be included in an extended analysis.

In addition the MUPAGE Monte Carlo file is excluded, which contains events from muons generated in the atmosphere (see Carminati 2007). The rejection of this fraction of events is reasonable, as the background rate was drawn from data (see Sect. 7.4). This would in the worst case lead to a lack of ν_e events which are reconstructed as tracks, while these events only have a small contribution to the total signal.

interaction	file nomenclature	energy range
$\bar{\nu}_e$ charged current	$anue\_x\_CC$	$4\,GeV$ to $300\,GeV$
$\bar{\nu}_e$ neutral current	$anue\_x\_NC$	$4\,GeV$ to $300\,GeV$
$\bar{\nu}_\mu$ charged current	$anumu\_a\_CC$	$5\,GeV$ to $20\cdot 10^3\,GeV$
$\bar{\nu}_\mu$ charged current	$anumu\_b\_CC$	$20\cdot 10^3\,GeV$ to $1\cdot 10^8\,GeV$
$\bar{\nu}_\mu$ neutral current	$anumu\_x\_NC$	$4\,GeV$ to $300\,GeV$
ν_e charged current	nue_x_CC	$4\,GeV$ to $300\,GeV$
ν_e neutral current	nue_x_NC	$4\,GeV$ to $300\,GeV$
ν_μ charged current	$numu\_a\_CC$	$5\,GeV$ to $20\cdot 10^3\,GeV$
ν_μ charged current	$numu\_b\_CC$	$20\cdot 10^3\,GeV$ to $1\cdot 10^8\,GeV$
ν_μ neutral current	$numu\_x\_NC$	$4\,GeV$ to $300\,GeV$

Table 2: used parts of the Run by Run Monte Carlo

5.2 Track reconstruction

In order to reconstruct the track of a muon, precise knowledge of the muon's position on its way through the detector is required. To measure the position of the muon on its trajectory, the arrival time t of Cherenkov photons at the OMs (see equation 4.14) is one of the major ingredients of an accurate track reconstruction. The aim of this kind of algorithm is to reconstruct as many events as possible, while the fraction of misreconstructed down-going atmospheric muons as up-going tracks should be suppressed. Many different track reconstruction strategies have been developed within ANTARES. The most common algorithms are:
Bbfit, developed by Jürgen Brunner, provides a fast reconstruction and good performance together with *Gridfit*, developed by Erwin Visser for the low energy regime. While this analysis focuses on high energetic track-like events, the algorithm *Aafit*, developed by Aart Heijboer (Heijboer 2004) is used and will be described in more detail.
Aafit is made of six steps:

1. **Pre-selection of OM hits**
   In order to ensure a significant background rejection, a rough pre-selection of OM hits is performed. While the hit with the largest amplitude is always assumed to be caused by a signal event, only hits are selected that fulfill

$$|\Delta t| \leq \frac{d}{v_g} + 100\ ns \tag{5.3}$$

   to make sure all hits are produced by the same event. Here Δt is the time difference between a hit and the hit with the largest amplitude, v_g represents the group velocity of Cherenkov photons in water and d the distance between two hits.

2. **Linear prefit**
   In this step a linear fit through the positions of the hits is assumed, where each hit occurs as point that is located on the muon track. This is expected to be a reasonable approximation under the assumption, that the length of the muon track in the detector is much larger than the attenuation length of the Cherenkov photons. This leads to the relation:

$$\vec{y} = \hat{H}\vec{\Theta} \tag{5.4}$$

   where $\vec{y}$ is a vector containing the hit positions and $\vec{\Theta}$ a vector of track parameters. Both vectors are related by the matrix $\hat{H}$, containing the only independent variables, the hit times.

3. **M-estimator fit**
   A M-estimator is an algorithm that maximizes a likelihood function. Based on the output of the linear prefit, this algorithm is stable against fluctuations in the exact starting point of the fit. By a set of hit quality assumptions, a reasonable track reconstruction can be achieved, using:

$$G = \sum_i \kappa \left(-2\sqrt{1 + A_i \frac{r_i^2}{2}} \right) - (1 - \kappa) f_{ang}(a_i) \tag{5.5}$$

   where $\kappa = 0.05$ is an optimized parameter using Monte Carlo, A_i the amplitude of the hit and $f_{ang}(a_i)$ an angular response function of the OM.

4. **Maximum likelihood fit**
   For each possible set of track parameters, the probability to obtain the observed hits can be calculated. This probability is called the likelihood of the event. In case of uncorrelated hits, this likelihood can be written as:

$$P\,(\text{event}|\text{track}) = \prod_i P(t_i | t_i^{th}, a_i, b_i, A_i) \tag{5.6}$$

   where t_i is the time of hit i and t_i^{th} the expected arrival time of the hit i. The parameters a_i and b_i stand for $a_i = \cos(\alpha_i)$ where α_i represents the incidence angle on the OM and b_i the expected photon path length.
   The fit, which is assumed to be the true one is defined by a set of track parameters for which the likelihood function is maximal.

5. **Repetition of steps 3 and 4 with different starting points**
   To improve the performance of the track fitting, steps 3 and 4 are repeated with different starting points. The best result is obtained by taking the fit with the best likelihood per degree of freedom.

6. **Maximum likelihood fit with improved PDF**
   As background hits can degrade the performance of the track reconstruction a last maximum likelihood fit is performed. This time a more complex likelihood function (compared to equation 5.6) is used, also taking background hits into account.

Even with an optimized track reconstruction algorithm there is still a significant fraction of misreconstructed atmospheric muons. In order to get rid of these events, fit quality parameters have to be introduced (see Ageron et al. 2012):

- **track fit quality parameter λ**
  The quality parameter λ can be used to reject badly reconstructed events like atmospheric muons and is defined as:

$$\lambda = \frac{\log(L)}{N_{hits} - 5} \times 0.1 \times (N_{comp} - 1) \tag{5.7}$$

  with the maximum value of the likelihood L and the number of degrees of freedom of the fit (e.g. the number of hits N_{hits}) minus the number of fit parameters. N_{comp} stands for the number of iterations of prefits from the second step.

- **angular uncertainty parameter** β
  The angular uncertainty parameter β is used to estimate the directional uncertainty from the error matrix of the fit. β is defined as:

$$\beta = \sqrt{\sin(\vartheta)^2 \cdot \sigma_\varphi^2 + \sigma_\vartheta^2} \tag{5.8}$$

  and incorporates the fitted zenith angle ϑ, as well as the zenith and azimuth errors σ_ϑ and σ_φ.
  For more details about track reconstruction please refer to (Heijboer, 2004; Ageron et al., 2012).

5.3 Energy reconstruction

As the muon loses energy on its path through the detector (see Sect. 3.2), energy reconstruction is more challenging compared to track reconstruction. With increasing energy of the muon, the amount of radiated emission (due to pair production or bremsstrahlung) increases. This energy dependent deposition within the detector can be used to estimate the original energy of the muon. Due to the small size of the ANTARES detector (see Sect. 4.2.3) compared to the muon track length no clear correlation between deposited energy within the detector and muon-energy can be seen, a priori.

The energy estimator developed by Jutta Schnabel (Schnabel 2010) uses an Artificial Neuronal Network (ANN) to estimate the muon energy based on the chosen observables. The simplest ANN consists of a set of input and output nodes, as well as several hidden layers of nodes (see Figure 5.1). All nodes of adjacent layers are connected with each other. The output is calculated according to:

$$z_j = g\left(\sum_i \omega_{ij} x_i\right), \tag{5.9}$$

where x_i is the input of the ith node, ω_{ij} the connection weight between node i and j and g an activation function, which describes the reaction of node j. The parameter z_j represents the current state of the node j in the hidden layer.

Just like every neural network, the ANN introduced here must be trained. For this purpose training sets, as well as validation sets are created. The information content in the training sets should be disjoint, but still contain the maximum amount of information. During the training process each training set is inserted into the ANN, while the output is compared with the expected values. While in the beginning the connection weights ω_{ij} are chosen randomly, they will be set recursively during the training process starting from the output layer. The aim of the training process is to minimize the mean square error (MSE):

$$\text{MSE} = \frac{1}{N_{sample}} \sum_{k=1}^{N_{sample}} \left(y_k^{ANN} - y_k^{sample}\right)^2 \tag{5.10}$$

As in this analysis the energy reconstruction is applied after the track reconstruction, parameters related to the muon track are taken into account for the energy reconstruction as well. Such parameters are:

- triggered hits / triggered OMs

- track length, track zenith, mean charge of a hit

Using this Artificial Neuronal Network, the energy estimator *ANNergy* is created. As this estimator has a good resolution for high energies, it is obvious to use it within this analysis. In the following, the energy reconstructed using ANNergy will be labeled as *annergy*. Appendix B proofs the reasonable output achieved by the use of ANNergy.
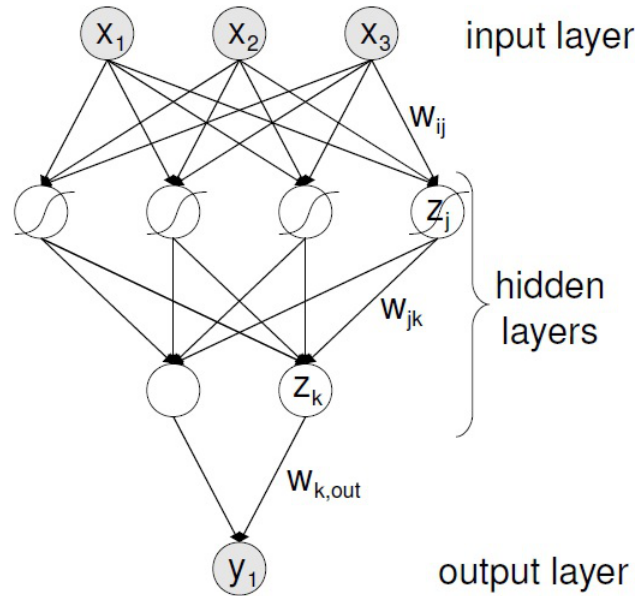
Figure 5.1: Schematic view of an Artificial Neuronal Network (ANN). Nodes in the input layer x_i are connected via connection weights ω_{ij} with nodes in the output layer y_j. Several layers of hidden nodes are located between the input and output layer. The state of the hidden nodes is set by equation 5.9.
Credit: Schnabel 2010

5.4 Data quality and run selection

A significant part of the detected data does not have an extragalactic or even atmospheric origin, but is caused by bioluminescent organisms in the deep sea (see Sect. 4.2.5). As the concept of Run by Run Monte Carlo simulations tries to model the highly variable background in an acceptable way, the question arises of how stable this reconstruction can be performed with different environmental conditions.

To answer this question, several checks have been introduced in order to select only runs with a reasonable amount of expected physical data. Selection criteria are for example:

- A reasonable data quality (see Sect. 5.4.1)

- A favorable coverage in the data Monte Carlo comparison (see Sect. 5.5)

- No technical problems or detector outages during data taking periods

5.4.1 The data quality parameter

The data quality parameter *QualityBasic (QB)* is introduced to have a compact flag of a joint number of data taking condition parameters. The QB is defined as a ranking parameter between 0 (worst conditions) and 4 (best conditions). Table 3 summarizes some environmental conditions, which are characteristic for a given QB value. While the *Baseline* represents the mean optical rate without bursts, the *Burst fraction* accounts for the amount of time during a run the rates were dominated by bursts.

However, while the QB values $QB > 0$ really represent the environmental data taking conditions, $QB = 0$ mainly is used to label runs that have been taken during technical problems with the detector. Therefore it is suggested to exclude these runs for any physical analysis.

QB value	Data taking condition
0	Run during < 1000 *s*, technical problems during data taking periods. It is suggested to exclude these runs for any physical analysis.
1	Baseline > 120 kHz, Burst fraction > 40%, less than 80% of all OMs are operating
2	Baseline > 120 kHz, Burst fraction > 40%, more than 80% of all OMs are operating
3	Baseline ≤ 120 kHz, 20% < Burst fraction ≤ 40%, more than 80% of all OMs are operating
4	Baseline ≤ 120 kHz, Burst fraction ≤ 20%, more than 80% of all OMs are operating

Table 3: Run classification based on the QualityBasic parameter. See: The ANTARES QB working group.

5.4.2 Run selection

In order to select only runs, which are expected to contain a significant amount of physical data, a run selection is performed. The following types of runs have been rejected from the final run selection.

5.4.2.1 Sparking runs:

Runs which are known to contain a significant number of sparking events are excluded from the final run selection. Sparking events are events for which the vertex position has been fitted close to the position of an OM. The high voltage of the photomultipliers sometimes causes a bright flash inside the OM. Instead of detecting desired Cherenkov photons, the OM itself acts as a point source. While these events are quite rare, they have not been modeled in the Run by Run Monte Carlo. Table 4 lists all known sparking runs within this analysis.

Run numbers of sparking runs:
30658 31309 33608 33610 34663 34665 35467 36600 36666 36670 36689 38347 38348 38349
38351 38352 38353 38355 38357 38482 39192 41668 41671 42507 42509 42511 42513 42746
42915 42919 43196 43202 43206 43210 43215 43684 43996 44030 44035 44070 45242 46980
51036 53508 53851 54512 64452 64457 66037 66039 66042 66046 66049 66053 65532 52675
55259 56457 63718

Table 4: List of sparking runs

5.4.2.2 Run setup and QB value:

As already mentioned in Sect. 5.4, QB = 0 runs show technical problems during data taking periods. Therefore, these runs are excluded from the final list. In addition, runs which have been taken with a preliminary or test detector configuration are excluded for data quality reasons. Such configurations are:

- *PRELIM* runs:
  These runs are labeled as preliminary and have been taken after some (not confirmed) tests on the run setup.

- *SCAN* runs:
  These runs are taken during the optimization processes of a new setup.

Finally, the definite run selection is expected to contain only reasonable runs. Appendix G shows the total list of selected runs.

5.5 Data Monte Carlo comparison

As the sensitivity plots calculated in Sect. 7.7 sometimes show a discrepancy between the self generated Monte Carlo and the Run by Run Monte Carlo simulation, the accuracy of the Run by Run MC will be studied in more detail.
This however, is done for the final run selection described in Sect. 5.4. In order to do so, a fixed parameter for the comparison has to be defined. Figure 5.2 displays the reconstructed zenith angle using Aafit (see Sect. 5.2). Events shown in the graph are:

- Gray:
  Data events, which have been reconstructed.

- **Black**:
  Triggered data. See Sect. 4.2.4 for more details about the ANTARES triggers.

- Yellow:
  Atmospheric events. These are atmospheric muon events, generated with the MUPAGE Monte Carlo event generator, which are assumed to follow a $\frac{dN}{dE} \propto E^{-3.6}$ energy spectrum (Carminati 2007). Therefore mostly low energetic atmospheric muons are detected.

- Blue:
  High energetic muon events, generated from neutrinos that have undergone a charged-current interaction. These events are produced by the GENHEN Monte Carlo event generator.

- Green:
  High energetic shower events, generated by the interaction of a high energetic neutrino and an electron. These events are produced by the GENHEN Monte Carlo event generator.

- Red:
  Sum of Monte Carlo events, consisting of atmospheric events, as well as high energetic muons and showers generated by GENHEN.

The bottom part of Figure 5.2 shows the ratio of **triggered data** over total Monte Carlo. While the ratio is fluctuating around unity, the Monte Carlo models the data in a precise way. The huge discrepancy right after 160° can be explained by a loss of statistics in the triggered data.
A detailed data Monte Carlo comparison for most of the selected sources can be found in Appendix F. A data Monte Carlo comparison is performed whenever high optical rates during flaring periods are known. The changing amount of statistics between different sources is caused by a different number of selected time intervals from the different light-curves (see Sect. 6). In addition, a data Monte Carlo comparison has been performed for PKS 2204-540

which shows favorable data taking conditions during flaring periods (see Figure 5.2). Sources for which no detailed data Monte Carlo comparison is performed show reasonable data quality (see Sect. 5.4) and are expected to be in good agreement with simulations. For more details about the Run by Run Monte Carlo generation please refer to Sect. 5.1.
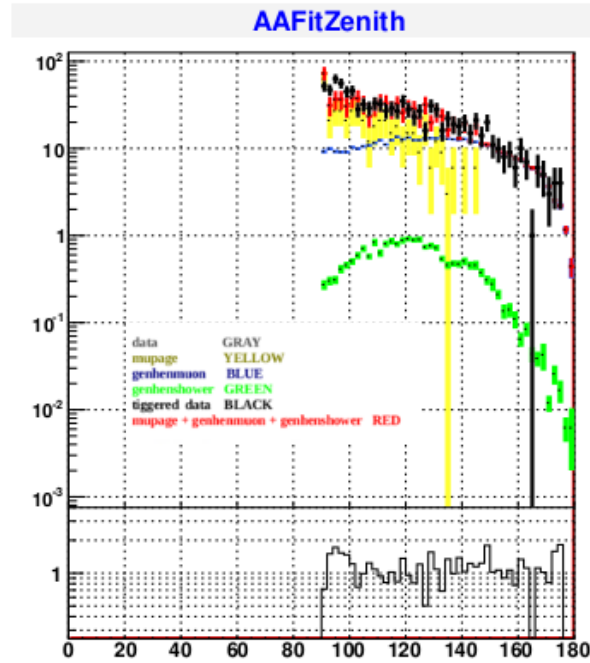
Figure 5.2: Data Monte Carlo comparison for the reconstructed zenith angle using Aafit of runs chosen for PKS 2204-540.
Top: Black shows the triggered data, while red labels the sum of all contributions considered by MC simulations. Different MC events are included in the graph: yellow represents atmospheric mupage events, muons (generated by the event generator GENHEN) are shown in blue and shower events are labeled in green.
Bottom: Comparison of triggered data (black) and sum of total MC (red). As the ratio is fluctuating around unity, the MC models the data in a precise way. Please note that the huge discrepancy right after 160° is caused through a loss of statistics in the triggered data.

6 Source sample

TANAMI has been monitoring more then 90 AGN since 2007 of which most are blazars. Many of these sources show highly variable γ-ray emission that is observed by *Fermi*. If proton acceleration takes place in AGN jets, then γ-ray photons and neutrinos are generated at the same time Mannheim 1993. Fig. 6.1 displays the reasonable correlation between observations with TANAMI and ANTARES. Sources of the TANAMI sample are shown as black circles. Red stars represent sources chosen for this analysis, and blue stars are sources selected by Fehn 2015. The color code labels the visibility for ANTARES, while unity represents the best visibility. All TANAMI sources lie in the field where ANTARES is most sensitive.

The source selection is based on the selection of sources which show bright short flares, e.g.
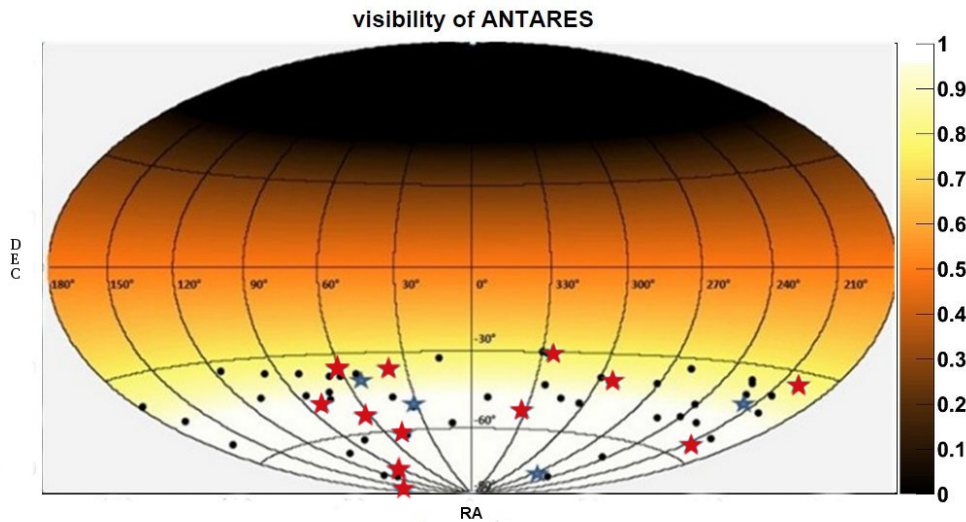
Figure 6.1: Visibility of ANTARES in equatorial coordinates. Black dots show TANAMI sources, red stars selected sources. Blue stars represent sources additional chosen by Fehn 2015.

on the order of 14 days (resulting from the two week binning of the light-curves). This is done to improve the sensitivity, as a compromise between low statistics and an effective background rejection had to be found. In more detail, the selection is done according to the following method which has been developed by Fehn 2015 and Müller 2014:

1. Take the maximum flux F_{max} that the source reaches during a flare.

2. Calculate the mean flux F_{mean} over the whole time period.

3. Choose only sources that satisfy $\frac{F_{\mathrm{max}}}{F_{\mathrm{mean}}} > 5$.

4. Count the number n of bins where the flux $F > F_{\mathrm{mean}} + 3\sigma$.

5. Calculate the weighting factor $w = \frac{F_{\mathrm{max}}}{F_{\mathrm{mean}}} \cdot \frac{1}{n}$.

The selection criteria are based on a relative increase of the source activity. In this context, the chosen threshold of $\frac{F_{\mathrm{max}}}{F_{\mathrm{mean}}} > 5$ is treated as a parameter that has been optimized. The optimization is done in order to suppress sources that show highly variable faint γ-ray emission. This selection minimizes the number of relevant flaring intervals and therefore reduces the amount of irreducible background.
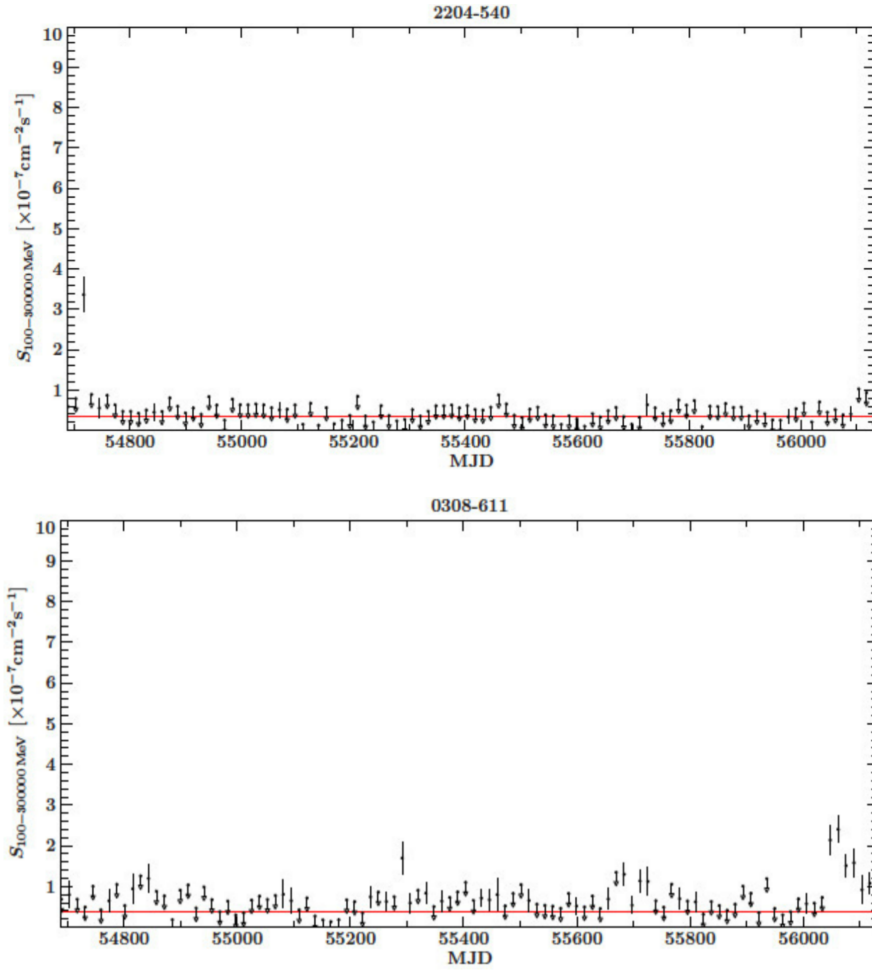
Figure 6.2: Light-curves of PKS 2204-540 and PKS 0308-611 in the energy range
$100\,\mathrm{MeV} - 300\,\mathrm{GeV}$.

Fig. 6.2 shows a comparison of PKS 2204-540, which is the best ranked source (according to crit. 5.) and PKS 0308-611.

While PKS 2204-540 has just one bright sharp flare at the beginning of the light-curve, PKS 0308-611 shows various faint flares over the entire time range. The normalized height of the light-curve is used as part of the likelihood. Therefore, a relative increase in the source activity leads to a gain in sensitivity. Figure 6.3 shows the resulting source ranking (according to point 5), and Appendix A lists a summary of all 12 sources used in this analysis sorted by their ranking factor.
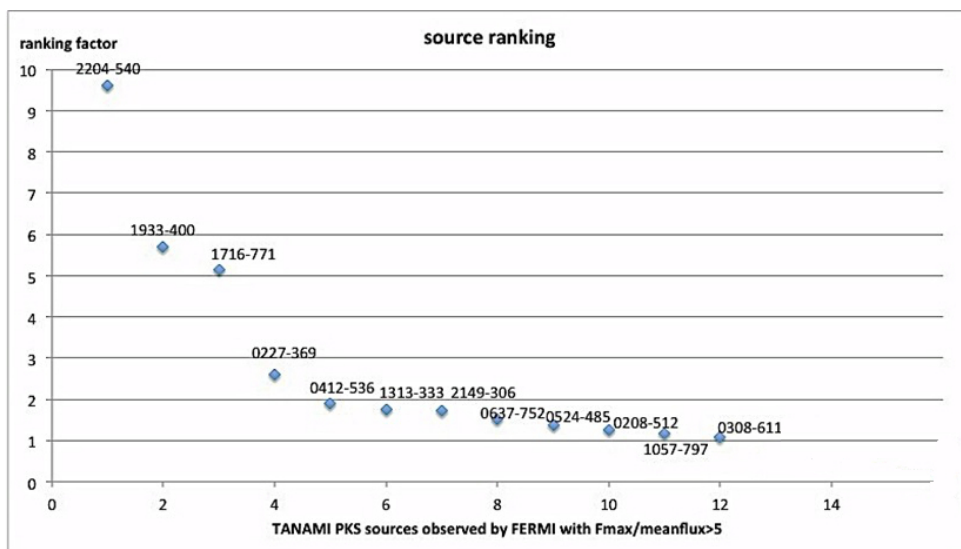
Figure 6.3: source ranking

7 Unbinned Maximum Likelihood Method

In Neutrino Astronomy it is not clear whether a detected neutrino event has been generated by an extraterrestrial source or in the atmosphere. To distinguish signal events from background events, assumptions on the special properties of signal events have to be made. For each event one can observe the reconstructed angle, reconstructed energy and the arrival time in the detector. The most obvious assumption on signal events in a point source analysis is that they point back to their origin. In regard to the reconstructed energy, one expects that the energy spectrum differs for signal events and background events produced in the atmosphere. A model independent approach is used, only assuming that neutrinos and γ-ray photons are produced simultaneously in an AGN-jet. *Fermi* γ-ray light-curves are used to correlate time information of detected neutrino events with associated γ-ray photons.

For a total number of N detected events, the contribution n_s of signal events is not known. Therefore, an unbinned maximum likelihood method is applied:

$$L(n_s) = \prod_{i=1}^{N} \left[\frac{n_s}{N} S_i + (1 - \frac{n_s}{N}) B_i \right] \tag{7.1}$$

where:
n_s is the unknown contribution of signal events,
N is the number of events,
S_i is the signal probability density, and
B_i is the background probability density.

Then, this likelihood function is maximized with respect to n_s, as a higher likelihood value corresponds to a more signal-like observation.
Here, $\frac{n_s}{N}$ is the fraction of signal events, and $(1 - \frac{n_s}{N})$ the fraction of background events.
The signal and background probability densities are calculated as follows:

$$S_i = N_i(\alpha) \times T_i(t) \times E_i^s \tag{7.2}$$

and

$$B_i = \frac{1}{5^2 \cdot \pi \cdot 0.1 \cdot 102} \times \frac{n}{\bar{n}} \times E_{i.}^b \tag{7.3}$$

$N_i(\alpha)$ is the probability function for the angle to the source, $T_i(t)$ the probability function for the time, and E_i for the energy (for either background or signal). The first factor in B_i is a normalization factor with 5^2 for a search-cone of $5°$ with a binwidth of $0.1°$ and 102 as the number of time bins. The term $\frac{n}{\bar{n}}$ represents the time dependency of the background with n number of events in a specific time period and $\bar{n}$, the mean number of events.
In the following, the individual parts of the likelihood will be described in more detail.

7.1 Angle term

As the signal is expected to originate from the source, a $5°$ search-cone around the source position is defined. In the signal case, the events are generated using Run by Run Monte Carlo version 2.2.1 (see Sect. 5.1). In the next step, theses events are reconstructed with Aafit (see Sect. 5.2) for various cuts of the quality parameter λ. The second quality parameter β has only a small effect. Therefore, the cut is fixed to $\beta_{cut} = 1$ (see Table 5 and Sect. 5.4). Afterwards, the position of each event has to be transferred from local coordinates to equatorial coordinates. Finally, the angle between a given event and the source position in the center of the cone is calculated according to (Fehn 2015):

$$\alpha = \arccos\left(\frac{\cos(d)\cdot\cos(a)\cdot\cos(d_s)\cdot\cos(a_s) + \cos(d)\cdot\sin(a)\cdot\cos(d_s)\cdot\sin(a_s) + \sin(d)\cdot\sin(d_s)}{\sqrt{(\cos(d)\cdot\cos(a))^2 + (\cos(d)\cdot\sin(a))^2 + (\sin(d))^2}\cdot\sqrt{\cos(d_s)\cdot\cos(a_s))^2 + (\cos(d_s)\cdot\sin(a_s))^2 + (\sin(d_s))^2}}\right) \quad (7.4)$$

with:

α as the angular distance to the source,

d as the declination of the reconstructed origin of the event,

d_s as the declination of the source,

a as the right ascension of the reconstructed origin of the event, and

a_s as the right ascension of the source.

All events passing the cuts are filled in an angle histogram between $0°$ and $5°$ with a binwidth of $0.1°$. This histogram is normalized according to its area and can be seen in Fig. 7.1. The normalized histogram serves as probability density part $N_i(\alpha)$ of the likelihood (see equation 7.1) in the case of a signal event. In case of a background event, the angle is chosen
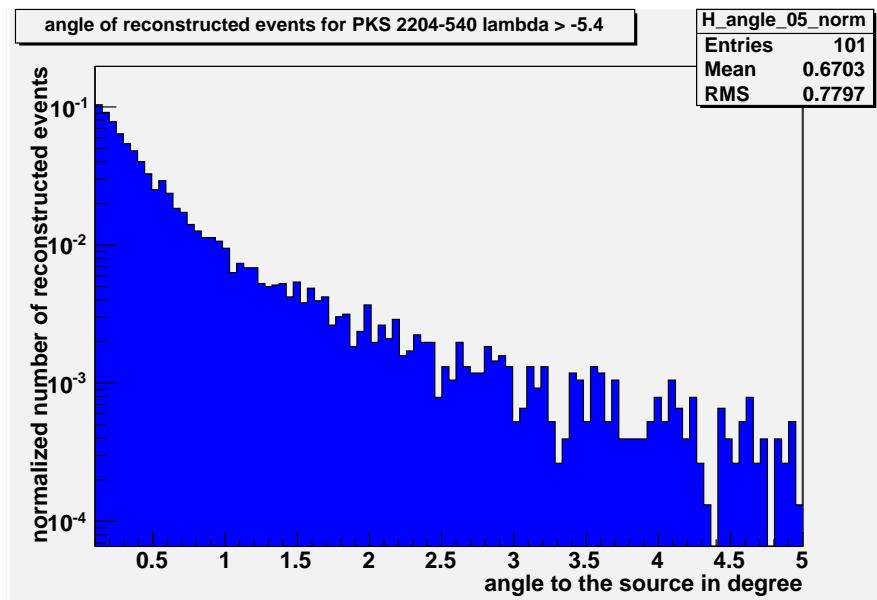
Figure 7.1: Normalized histogram of reconstructed angles for PKS 2204-540 for $\lambda > -5.4$.

from an uniform distribution according to $\sin(\alpha)$ because of the outwardly increasing area on the cone.

7.2 Energy term

Theoretical models (Mannheim et al., 2001; Mücke et al., 2003) predict a flat neutrino energy spectrum for AGN. According to these models, AGN are assumed to follow a $\frac{dN}{dE} \propto E^{-1}$ spectrum. An energy range of $10^2\,GeV$ to $10^8\,GeV$ is used for this analysis. In case of a signal event, the reconstructed energy of the track-like event is chosen for the same event as in the angle term. As this analysis restricts on track-like events, only muons are selected. For energy reconstruction ANNergy is used (see Sect. 5.3), as it provides a good resolution for high energies above $10^3\,GeV$ (see Figure B.3 in Appendix B).

β_{cut}	number of reconstructed events from rbrMC
0.5	7830
0.8	7885
1.0	**7866**
1.2	7871
1.5	7847

Table 5: Optimization of the angular uncertainty parameter β for PKS 2204-540 for $\lambda > -5.4$. As the variation of the β cut has only a negligible effect on the number of reconstructed events, the cut is fixed to $\beta_{cut} = 1$.

In order to correct for the assumed neutrino flux, every event has to be reweighted according to:

$$w_{\text{astro}} = \frac{1}{2} \cdot \frac{1}{4\pi} \cdot 10^{-7} \cdot 10^{4} \cdot w_2 \cdot E^{-1} \cdot \frac{1}{N_{\text{events}}} \cdot F_{\text{year}} \qquad (7.5)$$

Here, $\frac{1}{2}$ and $\frac{1}{4\pi}$ are the normalizations for the occurrence of neutrinos and antineutrinos and the solid angle implementation in the Monte Carlo. The term $w_2 \cdot E^{-1}$ is the global weight w_3 and 10^{-7} is the normalization constant for a flux of $10^{-7} \frac{\text{GeV}}{\text{cm}^2\text{s}}$. The factor 10^4 is important to convert meter in cm. Finally, N_{events} is the normalization for a given number of reconstructed events from the MC, and $F_{\text{year}} = \frac{T_{\text{run}}}{T_{\text{year}}}$ stands for the fraction of seconds a run takes during the year. After reweighting, these energies are filled in a histogram with $0.1 \log_{10}$ GeV bin width whose normalized height serves as E_i^s part of the likelihood.

To investigate the effect, the ANNergy energy estimator has on the muon energies, Fig. 7.2 shows a histogram of reconstructed energies using ANNergy versus the energy of the incoming muon. A correlation between the muon energy and the reconstructed annergy can be seen.

For background events the energy distribution is built up according to the energy distribution of data following a $\frac{dN}{dE} \propto E^{-3.6}$ energy spectrum of atmospheric muons (Carminati 2007). This is done in order to have a reasonable background approximation. After reconstruction, these events are filled in a similar histogram as signal events. The normalized height of these histogram serves as E_i^b part of the likelihood. Appendix B shows a list of energy distributions. Figure B.1 and Figure B.2 provide a crosscheck of the correct simulation of muon events in the Monte Carlo.

7.3 Time term

The time dependent approach is the main intention of this analysis. While this analysis is independent from any neutrino production model, the only assumption that is taken into account is a simultaneous production of photons and neutrinos. Therefore, *Fermi* γ-ray light-curves with a fortnight binning are used to select flaring periods. A fortnight binning of the light-curves is used, in order to maximize the number of bins for which a flux and not just an upper limit can be derived. The main purpose of this kind of selection is to minimize the contributing time periods and thus reduce the amount of background significantly.

Figure 7.3 shows a typical light-curve of PKS 1933-400 where the used time period from 01-Sep-2008 to 30-Jul-2012 is split up into 102 fortnights. Light-curves for the whole source sample can be found in the Appendix C.
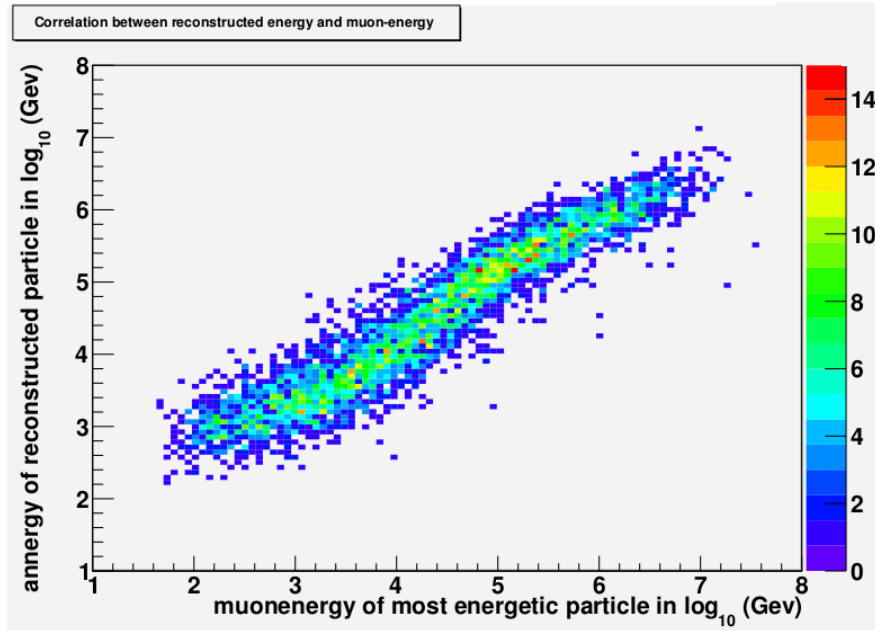
Figure 7.2: Histogram of reconstructed energies for PKS 2204-540 for $\lambda > -5.4$. A correction between the muon-energy (x-axes) and the annergy of the muon (y-axes) can be seen. For the muon-energy only the most energetic particle is used, as it carries almost the complete energy of the neutrino. The huge spreading is caused by ionization.

As photons and neutrinos are assumed to be generated simultaneously in the signal case, time intervals are chosen from the cumulative distribution function of the relevant light-curve, and used as $T_i(t)$ part of the likelihood. Figure 7.4 shows the selected light-curve fortnights for PKS 1933-400. A fortnight is chosen, whenever the light-curve provides a flux and not just an upper limit. Fortnights of high flux states are preferred. Therefore, an increase in the maximum flux F_{max} leads to a gain in sensitivity. In order to maximize the probability of a neutrino detection, fortnights with a detected flux in a low-pitched state of the source are also taken into account. These fortnights are chosen less likely for the $T_i(t)$ part of the likelihood, but still could contribute to a neutrino detection. It should be mentioned that these fortnights only have a rather negligible impact on the expected number of signal events.

In the background case, time is randomly chosen from one of the 102 bins of the light-curve, as these events are expected to be generated in the atmosphere.

7.4 Background rate

The background rate in a $5°$ cone is derived as follows:

a) Count the number of events in a $5°$ declination band over the whole time range with varying λ cuts.

b) Count the number of steradians in a $5°$ declination band.

c) Count the number of steradians in the cone.

An approximation of the background rate μ_{bg} is given by:

$$\mu_{\mathrm{bg}} \approx \frac{c}{b} \cdot a. \tag{7.6}$$
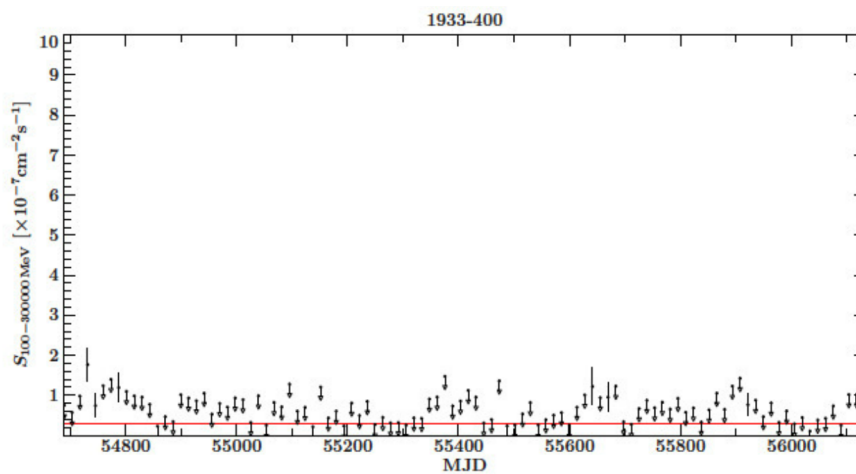
Figure 7.3: Light-curve for PKS 1933-400. Credit: Müller 2014
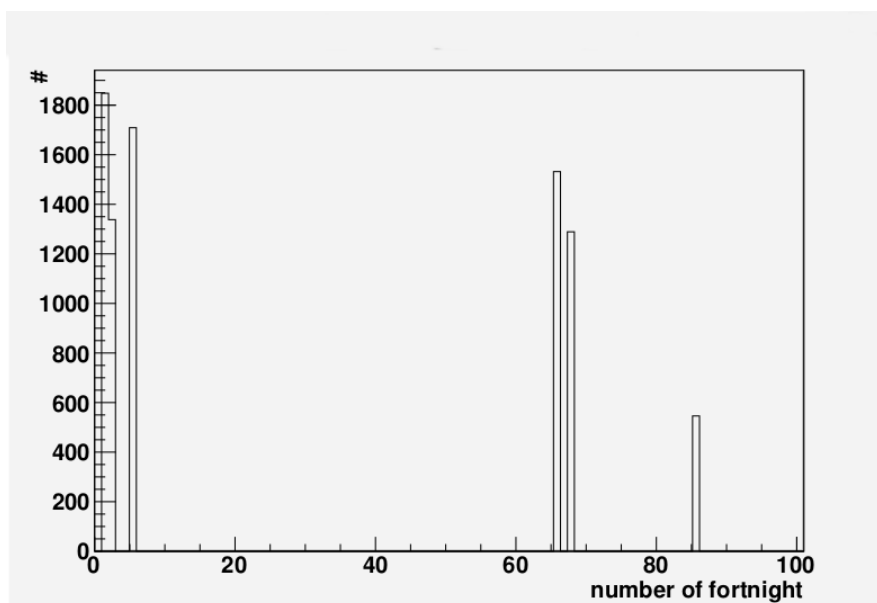
Figure 7.4: Selected fortnights for PKS 1933-400. Fortnights are chosen, whenever a flux and not just an upper limit was detected

The cone size is fixed to $5°$, as the signal contribution from outside this region is negligible (see Figure 7.1) and the amount of calculation time is optimized. Figure 7.5 shows the background rate in a $5°$ cone around the source position for two different λ-cuts (see Sect. 5.2). One can see that the background rate decreases with decreasing declination. For a harder λ cut, this effect is less pronounced because of the total loss of reconstructed events. As the background rate for sources in one specific declination band does not vary much, the same background rate is chosen for all sources in a given declination band. Furthermore, the central position in the declination band is taken to be the labeled position in Fig. 7.5 (e.g. in the declination band [-55,-50] $\delta = -52.5°$ is labeled). To account for time variation effects of the background rate, a correction factor (*corr*) is introduced. This factor is calculated according to the following scheme:

a) Calculate the number of events from all directions over all times including up- and down-going events.

b) Calculate the mean number of events.

c) Calculate the reconstructed number of events.

Thus, the correction factor is given by:

$$corr = \frac{c}{b}.$$
(7.7)

Figure 7.6 shows the resulting correction factor.
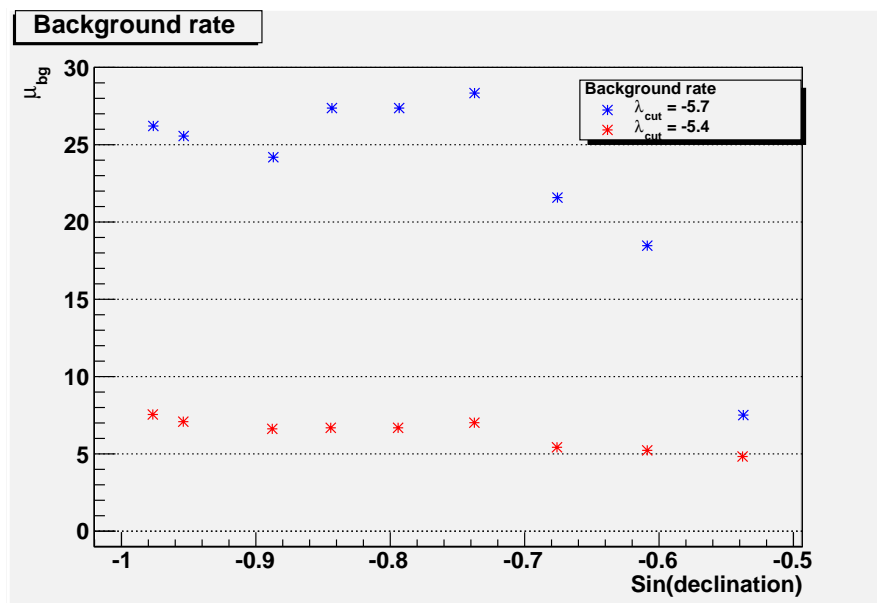
Figure 7.5: Background rate in a $5°$ cone around the source position.

7.5 Pseudo experiments

In order to derive the sensitivity for the selected sources, one has to generate pseudo experiments, where the generated events are known as true signal or signal plus background. For the background only case 10^7 events are generated, using the background rate as Poissonian mean.

In the signal plus background case 1000 events are generated, where the true number of signal events n_s serves as Poissonian mean. Figure 7.7 shows the performance of this method, where an excess at $n_s = 3$ signal events can be seen.
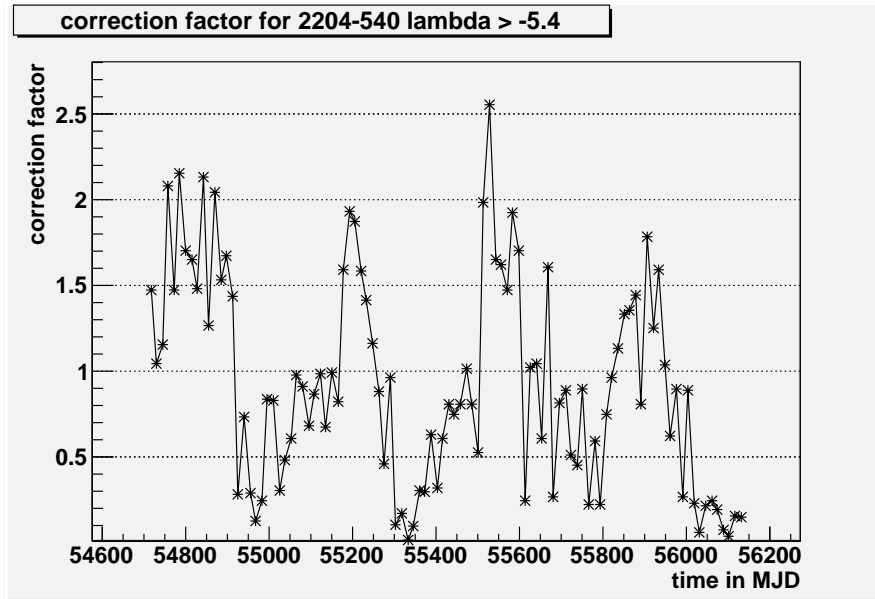
Figure 7.6: Correction factor to account for time variation of the background rate.
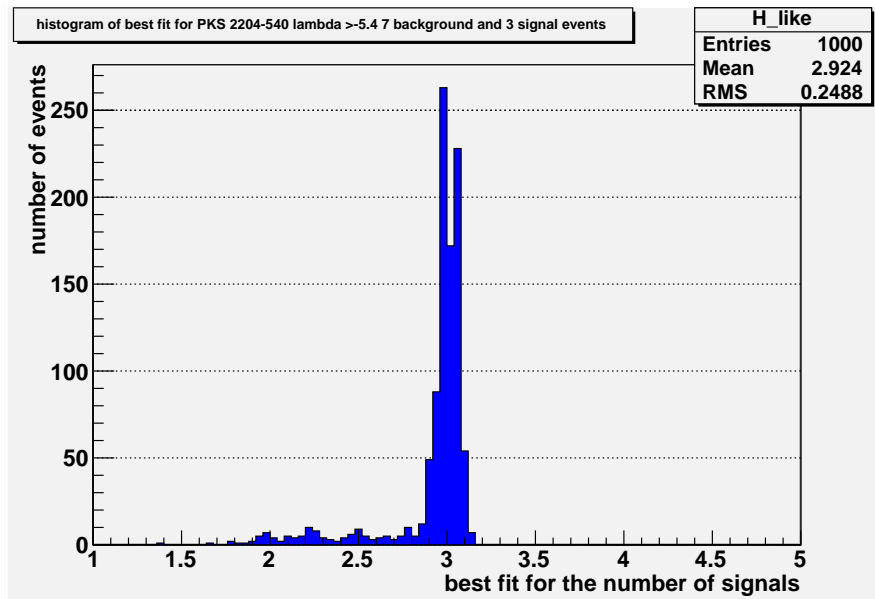
Figure 7.7: Histogram of the best fit value for the number of signal events $n_s = 3$.

7.6 Calculation of the Test Statistic

In order to derive the sensitivity for the selected sources, a quantity which correlates the likelihoods of background and signal events has to be defined. Therefore, the so called Test

Statistic (D) is calculated for every simulated pseudo experiment:

$$D = 2Log\left[\frac{L(\hat{n}_s)}{L(n_s = 0)}\right] \tag{7.8}$$

where $L(n_s = 0)$ is the likelihood in the background only case, and $L(\hat{n}_s)$ is the likelihood in the signal plus background case (n_s is the true number of expected signal events, while $\hat{n}_s$ is the estimated number of signal events). Figure 7.8 shows the distributions of the test statistic for PKS 2204-540 with $\lambda > -5.4$ (see Sect. 5.2). Shown in blue is the test statistic in the background only case. The distributions in the signal plus background case are plotted in yellow ($\hat{n}_s = 1$), red ($\hat{n}_s = 3$) and green ($\hat{n}_s = 5$). The threshold for a 5 σ discovery is given by the second greatest test statistic value in the background only case.

Now, the probability for a 5 σ discovery is calculated by counting the fraction of pseudo experiments in the signal plus background case, greater than the second greatest D value in the background only case. To test this method, the threshold of the background only pseudo experiments can also be derived from a fit according to:

$$f(D) = a \times 10^{-bD} \tag{7.9}$$

where a and b are just fit parameters and c is the largest D value. This leads to:

$$\int_x^c a \times 10^{-bD} dD = 0.1 \cdot \frac{1}{2} \cdot 5\sigma \cdot 10^7 \tag{7.10}$$

$$\left[\frac{a}{-b\ln(10)}10^{-bD}\right]_x^c = 0.2866515$$

$$\Rightarrow x = -\frac{1}{b}\log_{10}\left(0.2866515 \cdot \frac{b\ln(10)}{a} + 10^{-b\cdot c}\right).$$

The second greatest value of the test statistic in the background only case is 7.21, while the fit leads to 7.09.
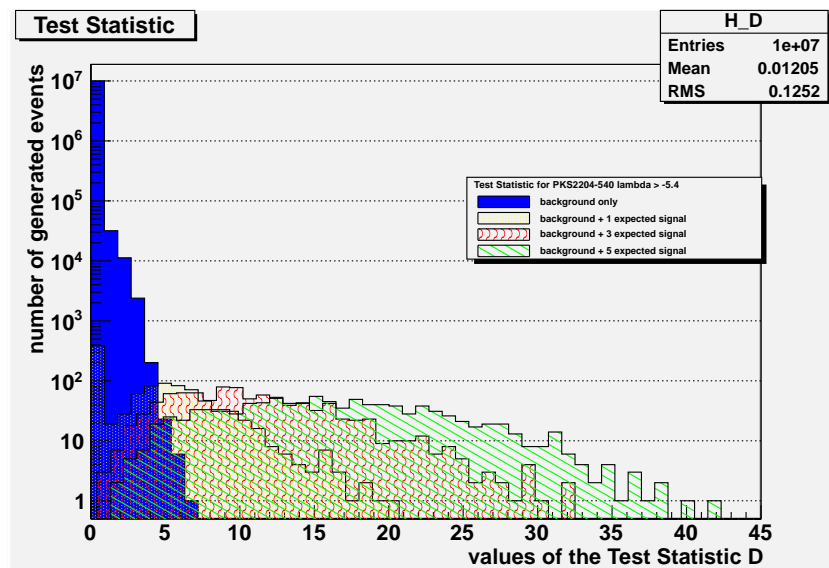
Figure 7.8: Test statistic D for PKS 2204-540 with $\lambda > -5.4$. Shown in deep blue is the test statistic for the background only case, while yellow, red and green represent the test statistic distributions in the signal plus background case.

7.7 Sensitivity

After the test statistic has been calculated (see Sect. 7.6), the sensitivity for each individual source can be derived. This is achieved by calculating the fraction of pseudo experiments in the signal plus background case greater than the second greatest D value in the background only case.

Beforehand, the track fit parameters have to be optimized source by source (see Sect. 5.2). As β has only a negligible effect on the number of reconstructed events, this parameter is fixed to $\beta < 1$. The track quality parameter λ is optimized according to the following scheme:

a) Calculate the number of reconstructed events per source for a given λ-cut.

b) Calculate the number of signal events n_s needed for a chance of 50 % to make a 5 σ discovery.

The optimized λ-cut is achieved when the ratio

$$c = \frac{a}{b}_{.}$$

(7.11)

is maximized. Table 6 summarizes the λ optimization process for PKS 2204-540, while the best λ cut is fixed to $\lambda > -5.4$.

Figure 7.9 displays the optimized sensitivity curves for PKS 2204-540, where the different colors represent different terms included in the likelihood calculation. While the green points only use the angle for the calculation of the likelihood, a significant gain in sensitivity is achieved by including the reconstructed energy (yellow points). The best result is obtained by including the light-curve term to the likelihood (blue points). Appendix D lists these graphs for the entire selected source sample.

As this analysis follows up the work of Fehn 2015, a comparison of the best results in the angle, annergy, and light-curve case is given in Figure 7.10. While Kerstin Fehn uses self generated Monte Carlo for the entire time period (further labeled as no-rbrMC), this analysis is based on the use of rbrMC (see Sect. 5.1). Both analysis agree for PKS 2204-540. This means, that the no-rbrMC models the highly variable background conditions in the deep sea in an acceptable way for this specific source. A comparison between both methods for the rest of the selected sources can be seen in Appendix E. For a significant number of sources both methods are not compatible. As the data-MC comparison for the rbrMC (see Sect. 5.5) is on a reasonable level, the results of the rbrMC analysis seems to be trustable.

λ_{cut}	number of reconstructed events from rbrMC	n_s needed for a chance of 50 % to make a 5 σ discovery	ratio c
-5.5	8248	2.0	4124
$\mathbf{-5.4}$	7866	1.8	**4370**
-5.3	7146	1.75	4083

Table 6: Optimization of the track quality parameter λ for PKS 2204-540.
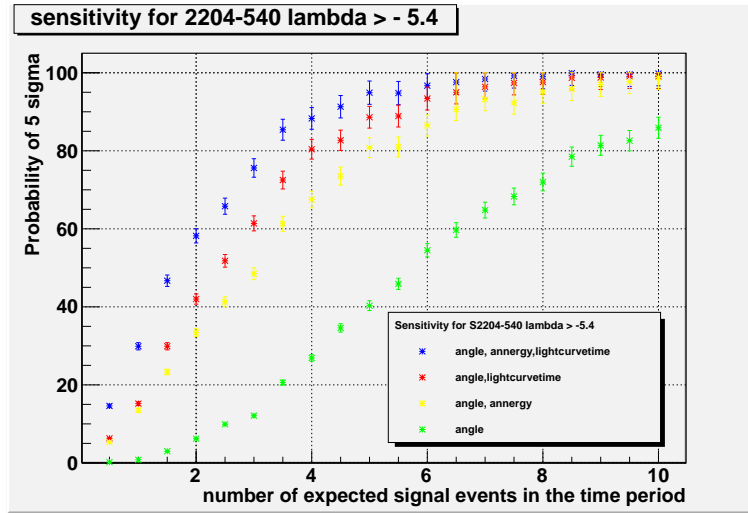
Figure 7.9: Optimized sensitivity for PKS 2204-540 with $\lambda > -5.4$. The green points represent the case, when just the angle part is used for the likelihood. The best result is achieved by combining angle, annergy, and light-curve time.
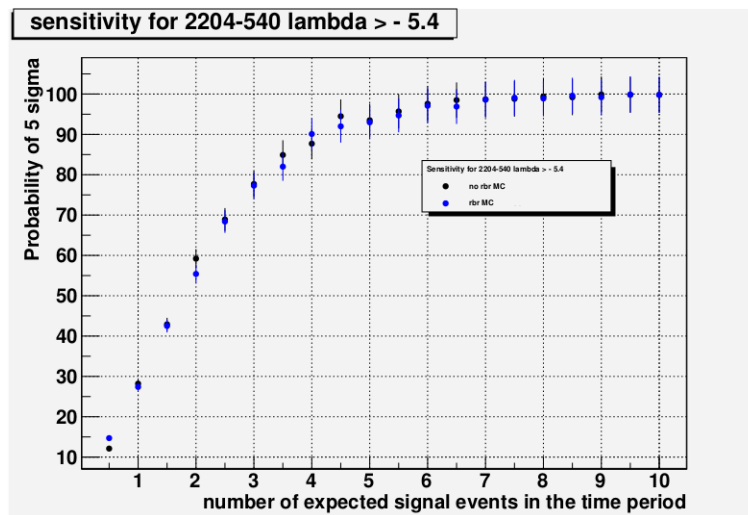
Figure 7.10: Comparison of the sensitivity for PKS 2204-540 with $\lambda > -5.4$ in the angle, annergy, and light-curve time case. Black points represent the result of the no-rbrMC analysis, while blue points show the sensitivity for the rbrMC. Both analysis are compatible.

8 Results and Discussion

Detected events are associated with selected sources by the calculation of their angular distance to the position of the source. In addition, the reconstructed energy, as well as the arriving time of each event is stored. Via the timing information every event can be placed within one of the 102 two-week periods of the light-curve starting from 01-Sep-2008.

An unbinned maximum likelihood method is applied to derive the sensitivity of a point source discovery. In order to do so, histograms of angle and energy are calculated in the case of signal or background events. The arrival time is correlated with flaring states of the selected sources. For a detailed description of the applied method please refer to Sect. 7.

Run by Run Monte Carlo simulations (see Sect. 5.1) have been used to model the highly variable environmental conditions in the deep sea. By the use of the time term from the light-curve, a significant increase in sensitivity has been achieved, see Figure 7.9 for PKS 2204-540 or Appendix D for the complete source sample.

In comparison to the work of Fehn 2015, several implementations in the calculation of the test statistic and sensitivity have been improved. Technical limitations, like an angular and energy uncertainty are added to the calculation. As this project is based on the correlation of neutrino and photon properties, a major gain in sensitivity is achieved by an improved implementation of the correlation. Figure 8.1 visualizes the advantage of the new script (red), with respect to the original implementation (black) for the results of the no-rbrMC analysis. Please note, that for the results given by Fehn 2015, no simple comparison to the outcome of this work is possible, because of the improved implementations used to generate the results of both analysis.

The quantity used to compare results of different sources is the number of signal events n_s, needed for a chance of 50 % to make a 5 σ discovery. Table 7 summarizes the results of all 12 sources, together with the values for the previous no-rbrMC analysis. A source is labeled as *both analysis compatible* in the case, where the sensitivity plots of both analysis are mostly compatible within their error bars. Please note, that statistical error bars are used. The flag *bad data taking conditions* is used to label sources, for which high optical rates during flaring periods or technical problems are known. While suspicious runs are removed from the final run selection (see Sect. 5.4.2), these sources have to be treated with caution, especially if promising events would occur during these periods.

From Table 7 it is clear that both analyses differ for a number of sources. While for the self generated Monte Carlo simulation of the no-rbrMC analysis events from a specific direction can be simulated with a reasonable amount of statistics, the rbrMC analysis takes the rapidly changing environmental conditions into account.

To verify the representation of data by the rbrMC, a data Monte Carlo comparison (see Sect. 5.5 and Appendix F) has been performed. The comparison clearly demonstrates, that data is modeled well by the rbrMC. This, however leads to the conclusion, that the Run by Run Monte Carlo represents the data on an accurate level, and thus seems to be trustworthy. As the no-rbrMC analysis assumes characteristic $QB = 4$ conditions (see Sect. 5.4.1) during the entire time period, highly variable outbursts of bioluminescent activity seem to have a rather huge impact on the outcome of a point source analysis.

Please note, that the results shown in Table 7 seem no longer to be connected to the source ranking (see Sect. 6), which is based on the selection of short and bright γ-ray flares. This ef-

fect is visible both in the no-rbrMC as well as in the rbrMC analysis. The reason for this effect can be found in the light-curve normalization of the sensitivity calculation. While the source selection is based on the measured γ-ray flux, the sensitivity calculation uses normalized light-curves for the calculation of the likelihood term (see equation 7.1). As this normalization only takes the integrated γ-ray flux of just one source into account, the absolute brightness of the sources isn't used for the calculation.

Thus, only the time evolution of γ-ray flares effects the sensitivity calculation. Sources, which show sharp and short flares result in a better sensitivity, because of their effective background rejection due to the short selected time window.

To conclude, a time dependent approach has a significant impact on the outcome of a point source analysis. This is independent of the kind of used Monte Carlo (please refer to Fehn 2015 for the no-rbrMC analysis). While flaring AGN are a promising candidate for the sources of high-energetic extraterrestrial neutrino point sources, a detection is still insignificant. Nevertheless, the implementation of the rbrMC has led to a precise modeling of neutrino data, as well as a more accurate sensitivity calculation with respect to the no-rbrMC analysis.
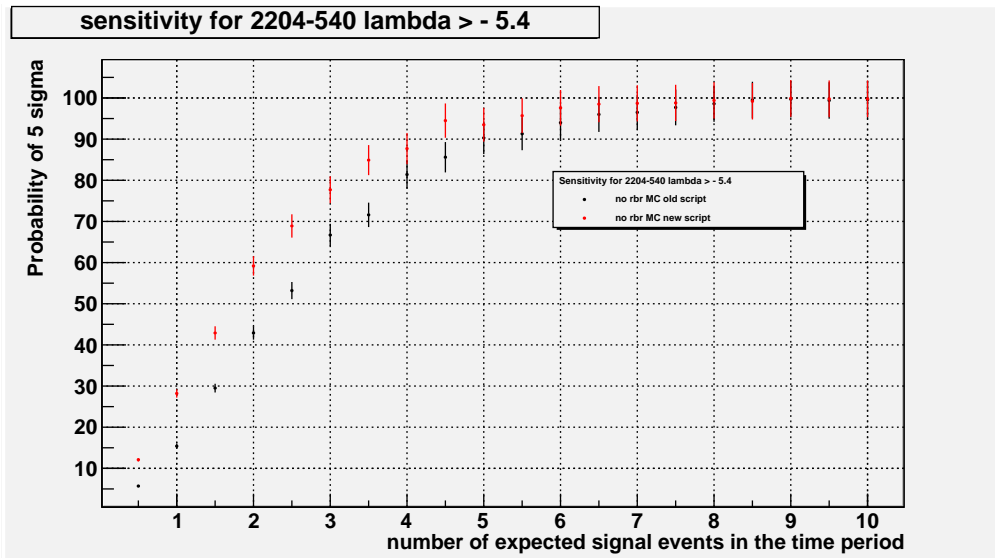
Figure 8.1: Comparison of the sensitivity for PKS 2204-540 with $\lambda > -5.4$ in the angle, annergy and light-curve time case. Black represents the result of the no-rbrMC analysis in the original implementation. Red represents the sensitivity after the improvement of several implementations, which results in a significant increase in sensitivity.

source	λ_{cut}	n_s needed for a chance of 50% to make a 5σ discovery with no-rbrMC (rbrMC)	both analysis compatible	bad data taking conditions
PKS 2204-540	-5.4	1.7 (1.84)	yes	
PKS 1933-400	-5.5	1.7 (1.8)	yes	
PKS 1716-771	-5.5	1.9 (2.25)	no	x
PKS 0227-369	-5.5	1.95 (1.32)	no	
PKS 0412-536	-5.4	1.9 (1.75)	yes	
PKS 1313-333	-5.6	2.25 (2.42)	yes	x
PKS 2149-306	-5.6	3.55 (2.75)	no	
PKS 0637-752	-5.5	3.2 (2.3)	no	x
PKS 0524-485	-5.5	1.9 (1.85)	yes	
PKS 0208-512	-5.4	2.35 (2.4)	yes	x
PKS 1057-797	-5.4	1.6 (2.6)	no	
PKS 0308-611	-5.4	1.8 (2.0)	yes	x

Table 7: Summary of the results for all 12 sources. Given are the source label, the optimized λ cut (see Sect. 7.7), and the value of n_s needed for a chance of 50% to make a 5σ discovery. If the sensitivity plots of both analysis are mostly compatible within their error bars, this source is labeled as *both analysis compatible*. Sources for which high optical rates during flaring periods or technical problems are known are labeled, although these runs have been excluded from the final list (see Sect. 5.4.2). The underlying sensitivity plots are listed in Appendix D and E.

9 Outlook

This work offers an overview of the taxonomy of active galactic nuclei, as well as their unification schema. Properties of AGN like the accretion of matter or radiation processes are discussed, together with possible neutrino generation models. An introduction to the multiwavelength program TANAMI, and the ANTARES neutrino detector is given, while the simulation and reconstruction of ANTARES data for highly variable environmental conditions is discussed.

As ANTARES is highly sensitive to the southern sky, a sample of 12 TANAMI sources is chosen. By the correlation of neutrino events measured with ANTARES and photons from *Fermi* γ-ray light-curves, a significant gain in sensitivity is achieved. The usage of Run by Run Monte Carlo simulations, which model highly variable background conditions in the deep sea, leads to a more precise calculation of the sensitivity per source.

An analysis has been developed which uses the full time-varying conditions of the ANTARES detector, combined with the time-variability of expected neutrino sources, to maximize the probability of a correlated neutrino detection. In order to compare results of different sources, the number of signal events n_s, needed for a chance of 50 % to make a 5 σ discovery has been introduced.

In the future a stacked search can be performed in order to increase the probability for a correlated neutrino detection. In the case of insufficient statistics for a significant detection, an upper limit on the expected neutrino flux can be calculated. This has to be done for real neutrino data instead of Monte Carlo simulations.

Beside the most obvious extensions of this work, some more general aspects could be taken into account:

- Reconstruction:
  While this analysis is using Aafit (see Sect. 5.2) for track reconstruction and ANNergy (see Sect. 5.3) as energy estimator, many other reconstruction algorithms exist within ANTARES. By testing and combining different reconstruction methods, a more effective track and energy reconstruction would be possible.

- Track & Showers:
  While this analysis is focusing on track-like events, the usage of shower events would result in an increase of statistics in signal events and thus enhance the probability of a correlated neutrino detection.

- Multiwavelength neutrino correlation:
  While the goal of this analysis is the correlation of neutrinos with γ-ray photons observed by *Fermi*, a correlation with e.g. VLBI data from TANAMI could lead to a more precise understanding of neutrino generation within a jet.

- Sources:
  The most obvious extension would be the use of a larger source sample. While ANTARES is most sensitive to the southern sky (see Sect. 6), an extension to a larger (TANAMI) source sample would be useful. In addition, sources in the northern sky could also be included to the sample. In this case, a weighting of sources according to their acceptance to the ANTARES detector would be reasonable.
  The current source selection criteria, which is based on the selection of bright short flares, could be revised in order to find an optimal balance between an effective background rejection and a maximization of detection time.

Finally, the application of the flux of the detected γ-ray flare within the analysis chain and not just in the source selection (see Sect. 7), would indeed result in an improved neutrino-γ-ray correlation.

- Instrumented volume:
  While the field of neutrino astronomy is mainly limited by statistics, the only solution for this problem is to use longer time intervals or a larger instrumented volume. The *KM3NeT/ARCA (Cubic Kilometer Neutrino Telescope)* project is a planed deep sea water Cherenkov telescope in the Mediterranean Sea. It will have an instrumented volume of about 1 km^3.
  With this increase of instrumented volume there is justified hope that a data analysis using the here developed methodology may finally reveal extraterrestrial neutrino point sources.

Appendices

A Source List

source	λ_{cut}	type	RA (J2000)	Dec (J2000)	redshift
2204-540	-5.4	Q	331.93208	-53.77611	1.206
1933-400	-5.5	Q	294.3175	-39.96722	0.965
1716-771	-5.5	U	260.96042	-77.23056	unknown
0227-369	-5.5	Q	37.3685375	-36.7324503	unknown
0412-536	-5.4	U	63.32167	-53.53389	unknown
1313-333	-5.6	Q	199.03333	-33.64972	1.21
2149-306	-5.7	Q	327.98125	-30.465	2.345
0637-752	-5.5	Q	98.94375	-75.27139	0.653
0524-485	-5.5	U	81.5694633	-48.5102197	unknown
0208-512	-5.4	B	63.6925	-51.01722	0.999
1057-797	-5.4	B	164.6804571	-80.0650442	unknown
0308-611	-5.4	Q	47.4837467	-60.0775153	1.48

Table 8: Summary of the properties for all 12 sources investigated in this thesis. (Q=quasar, B=blazar, U=unidentified)

B Energy Plots
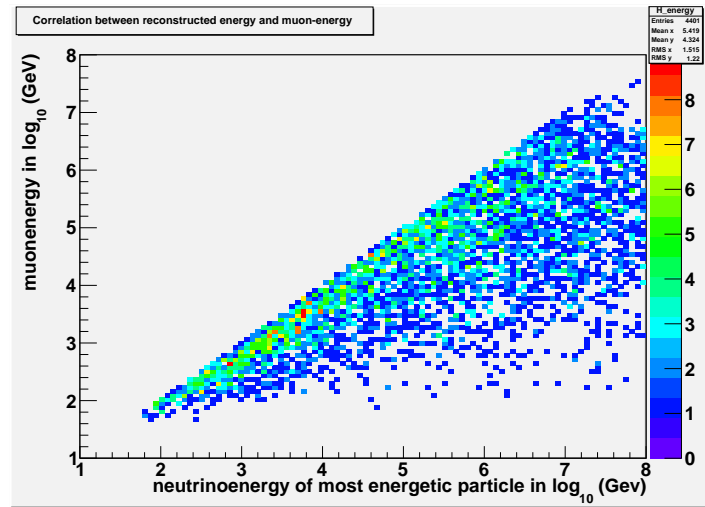
Figure B.1: Correlation between neutrino and muon energy for PKS 2204-540 for $\lambda > -5.4$. A correlation can be seen. The maximal gained energy of the muon is the total energy of the neutrino.
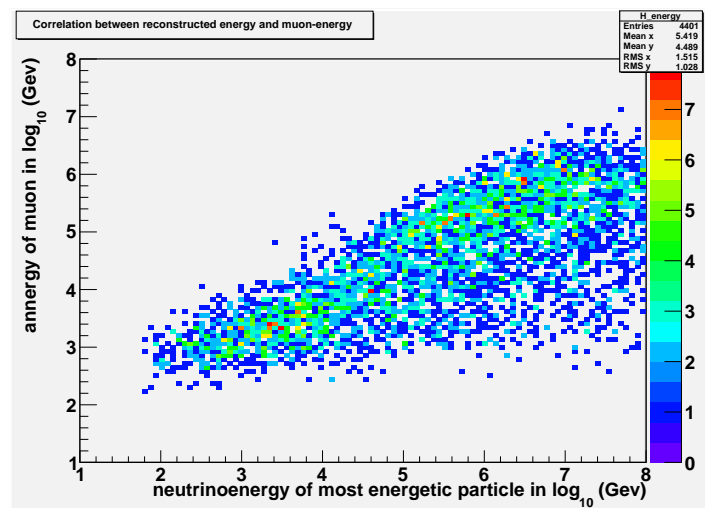
Figure B.2: Correlation between neutrino and muon energy for PKS 2204-540 for $\lambda > -5.4$. On the y-axes the muon annergy is shown. Due to the use of the ANNergy energy estimator the muon energy is smeared out and can take values greater than the total neutrino energy.
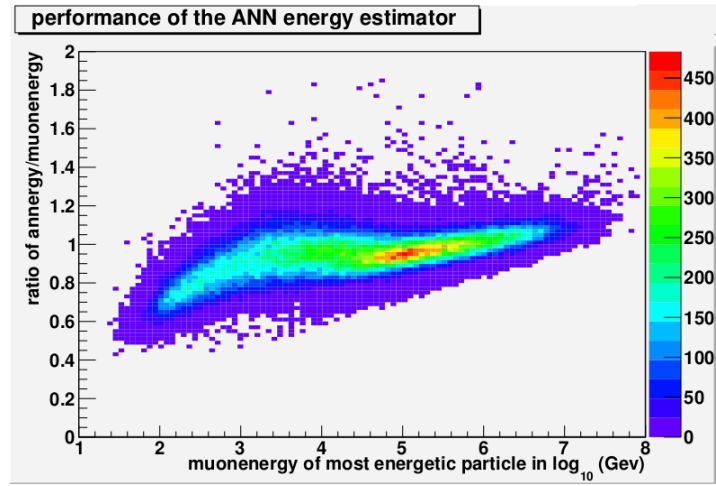
Figure B.3: Performance of the ANN energy estimator for PKS 2204-540 for $\lambda > -5.4$. On the y-axes the ratio of the muon annergy over the muon energy from the x-axes is shown. The huge spreading is caused by ionization.

C Light-curves of all 12 sources
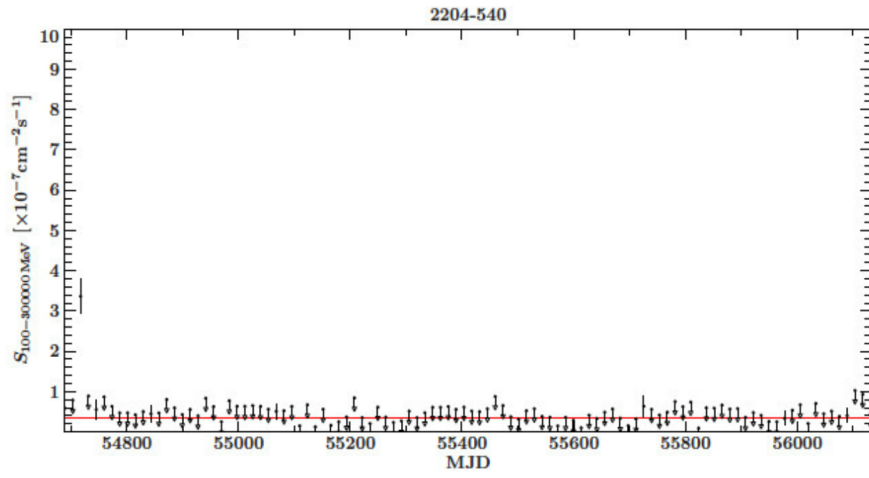
Figure C.1: Light-curve for PKS 2204-540
Credit: Müller 2014
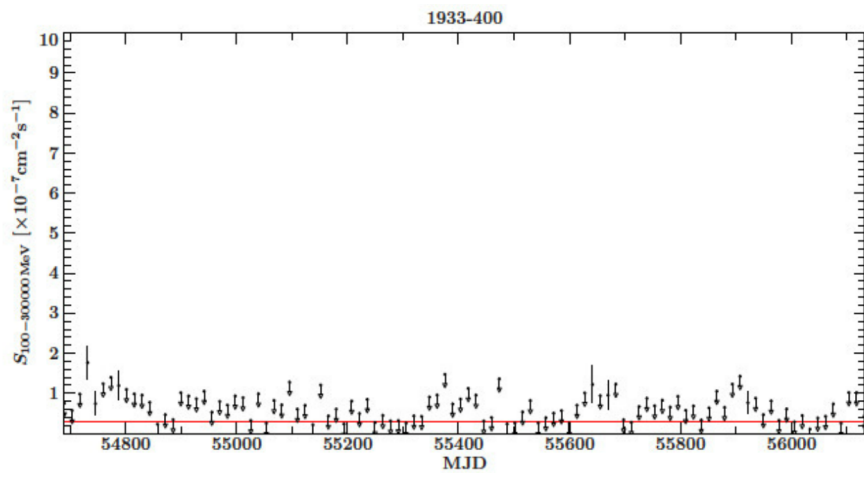
Figure C.2: Light-curve for PKS 1933-400
Credit: Müller 2014
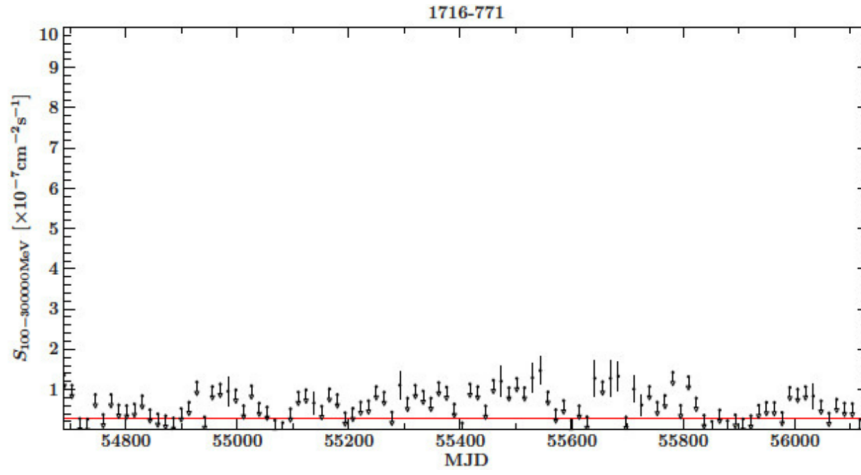
Figure C.3: Light-curve for PKS 1716-771
Credit: Müller 2014
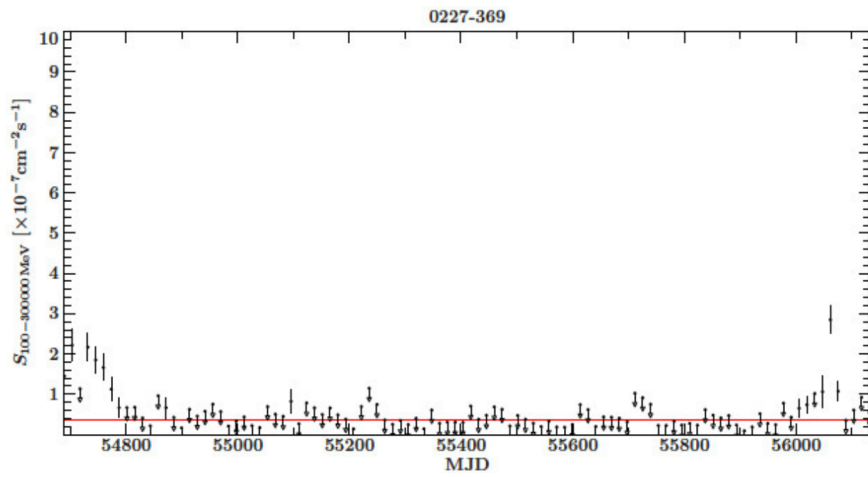
Figure C.4: Light-curve for PKS 0227-369
Credit: Müller 2014
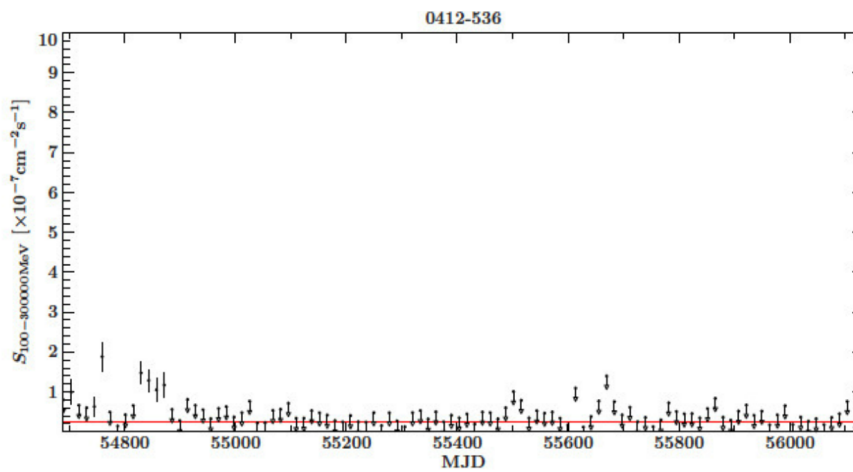
Figure C.5: Light-curve for PKS 0412-536
Credit: Müller 2014
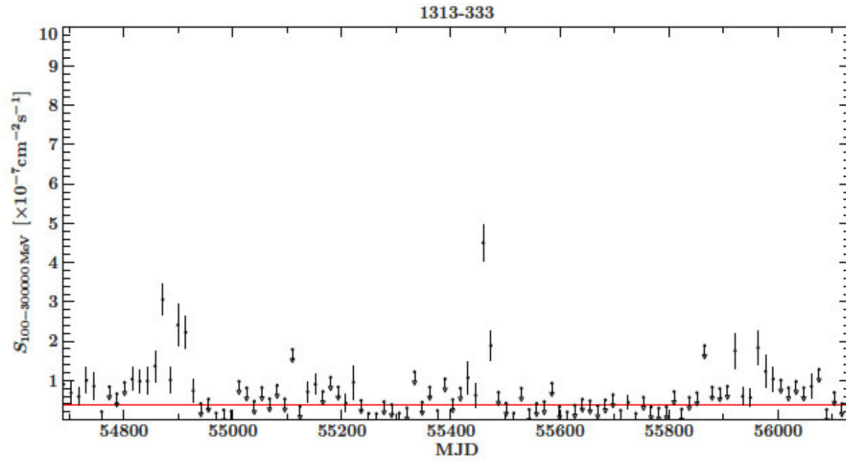
Figure C.6: Light-curve for PKS 1313-333
Credit: Müller 2014
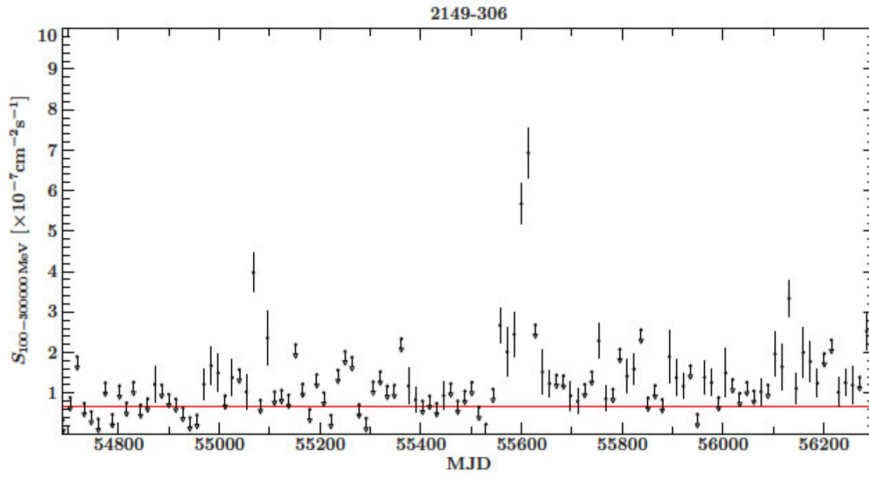
Figure C.7: Light-curve for PKS 2149-306
Credit: Müller 2014
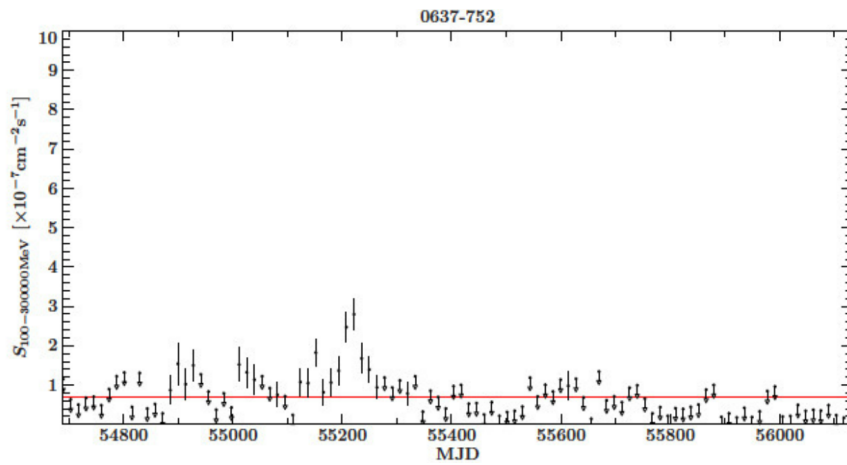
Figure C.8: Light-curve for PKS 0637-752
Credit: Müller 2014
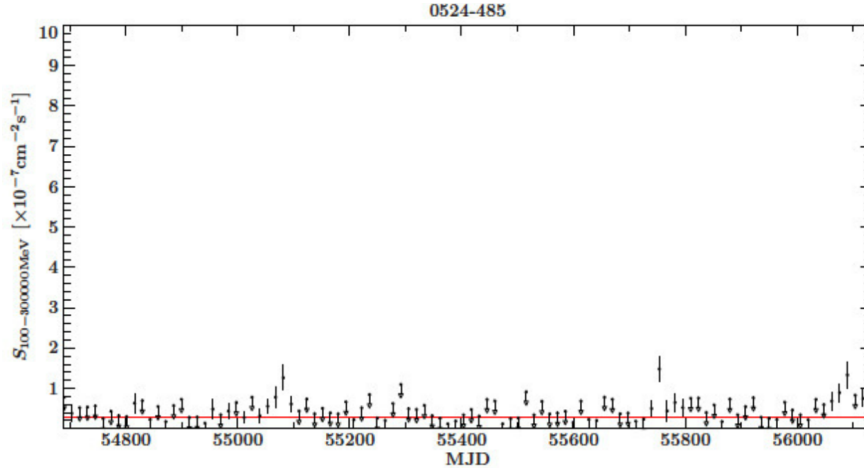
Figure C.9: Light-curve for PKS 0524-485
Credit: Müller 2014
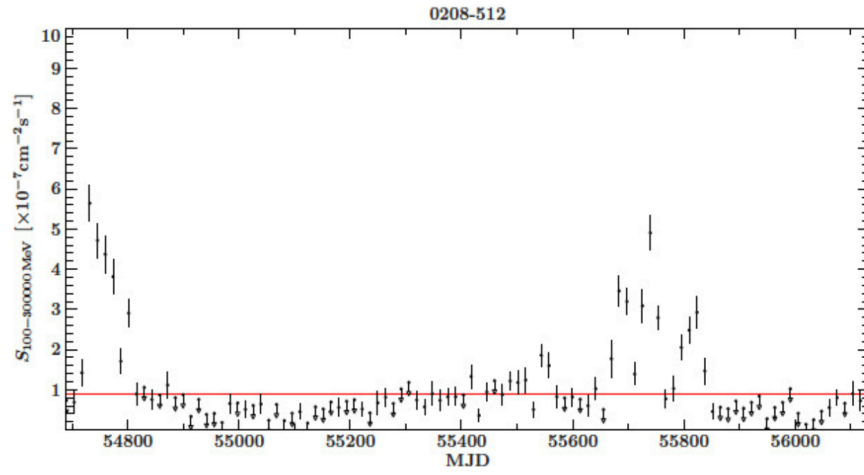
Figure C.10: Light-curve for PKS 0208-512
Credit: Müller 2014
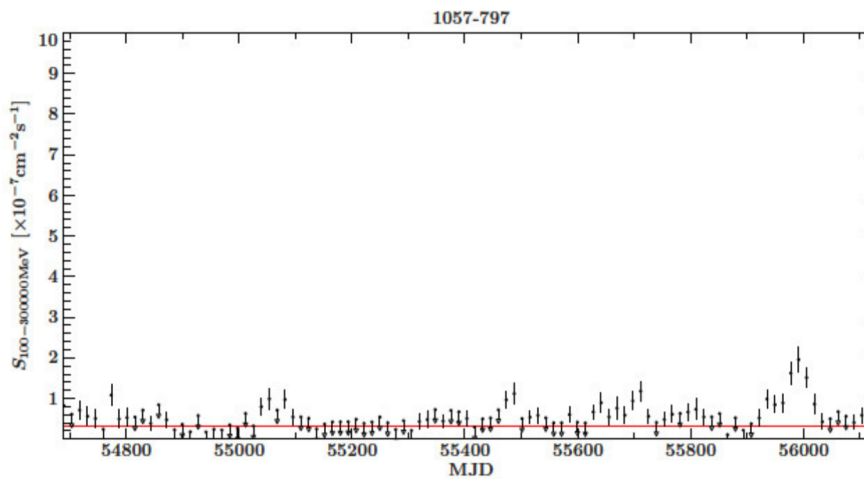
Figure C.11: Light-curve for PKS 1057-797
Credit: Müller 2014
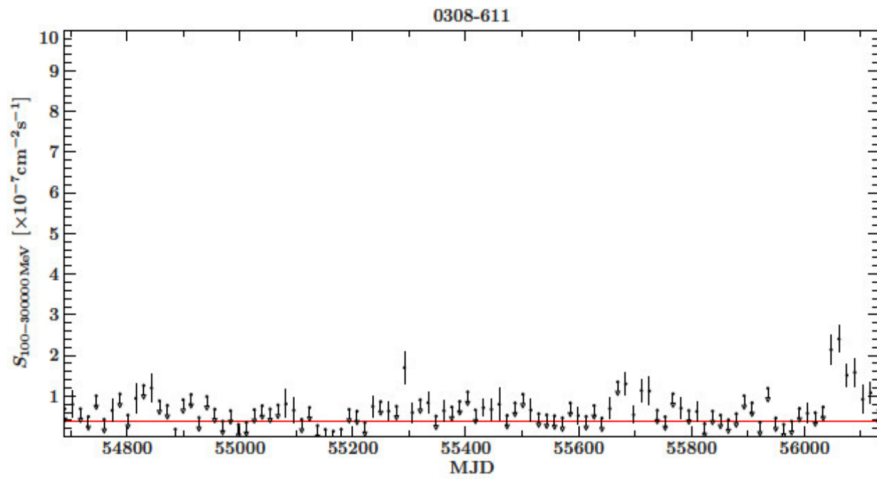
Figure C.12: Light-curve for PKS 0308-611
Credit: Müller 2014

D Sensitivity plots of all 12 sources
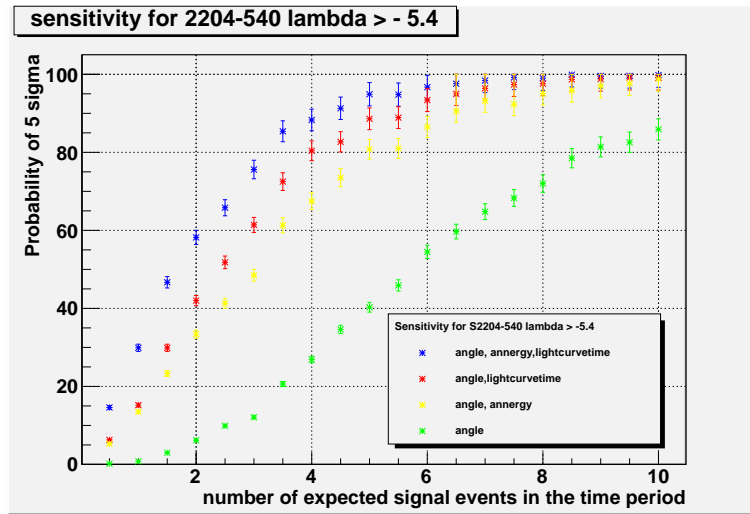
Figure D.1: Optimized sensitivity for PKS 2204-540 with $\lambda > -5.4$. The green points represent the case, when just the angle part is used for the likelihood. The best result is achieved by combining angle, annergy and light-curve time.
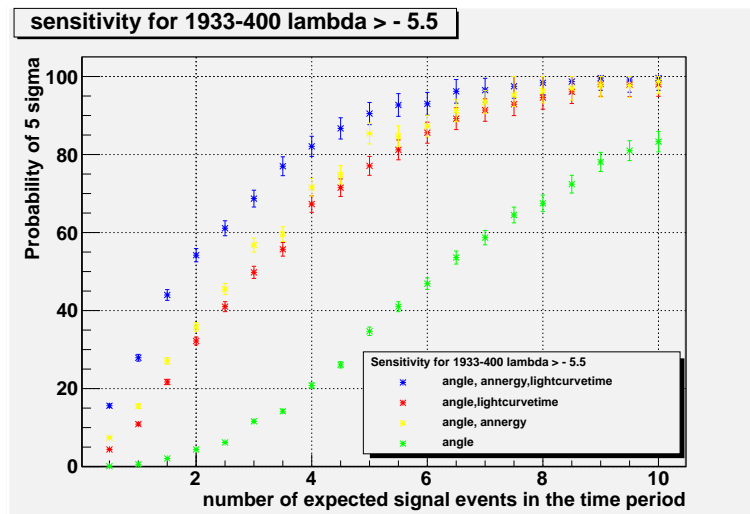
Figure D.2: Optimized sensitivity for PKS 1933-400 with $\lambda > -5.5$. The green points represent the case, when just the angle part is used for the likelihood. The best result is achieved by combining angle, annergy and light-curve time.
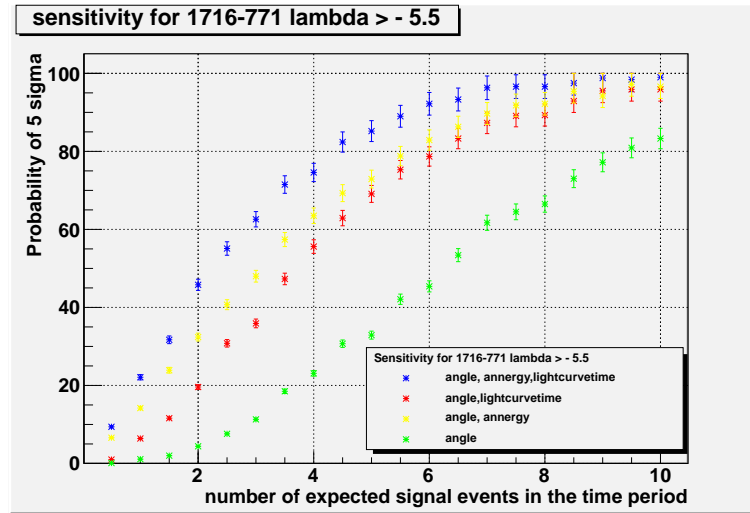
Figure D.3: Optimized sensitivity for PKS 1716-771 with $\lambda > -5.5$. The green points represent the case, when just the angle part is used for the likelihood. The best result is achieved by combining angle, annergy and light-curve time.
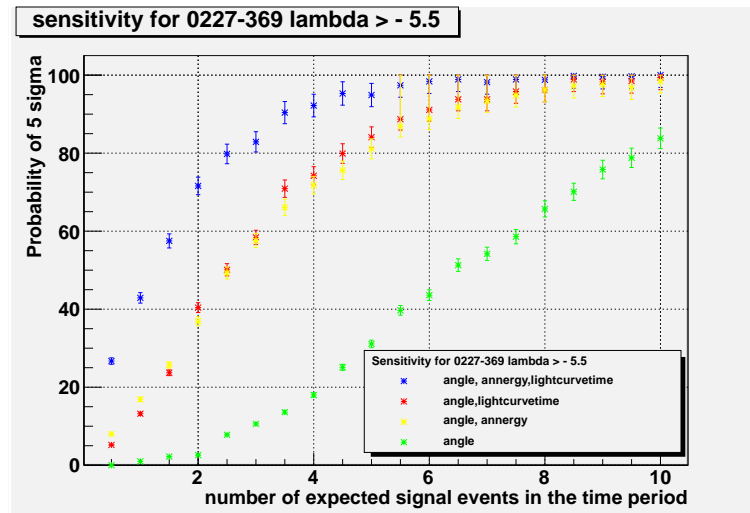
Figure D.4: Optimized sensitivity for PKS 0227-369 with $\lambda > -5.5$. The green points represent the case, when just the angle part is used for the likelihood. The best result is achieved by combining angle, annergy and light-curve time.
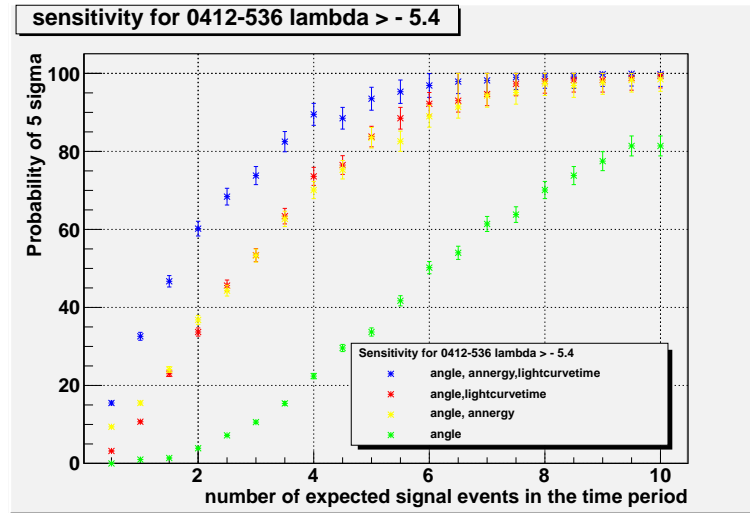
Figure D.5: Optimized sensitivity for PKS 0412-536 with $\lambda > -5.4$. The green points represent the case, when just the angle part is used for the likelihood. The best result is achieved by combining angle, annergy and light-curve time.
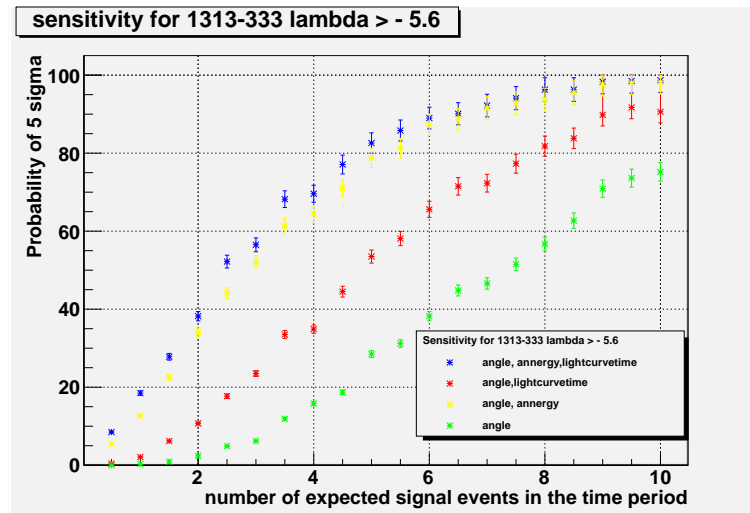
Figure D.6: Optimized sensitivity for PKS 1313-333 with $\lambda > -5.6$. The green points represent the case, when just the angle part is used for the likelihood. The best result is achieved by combining angle, annergy and light-curve time.
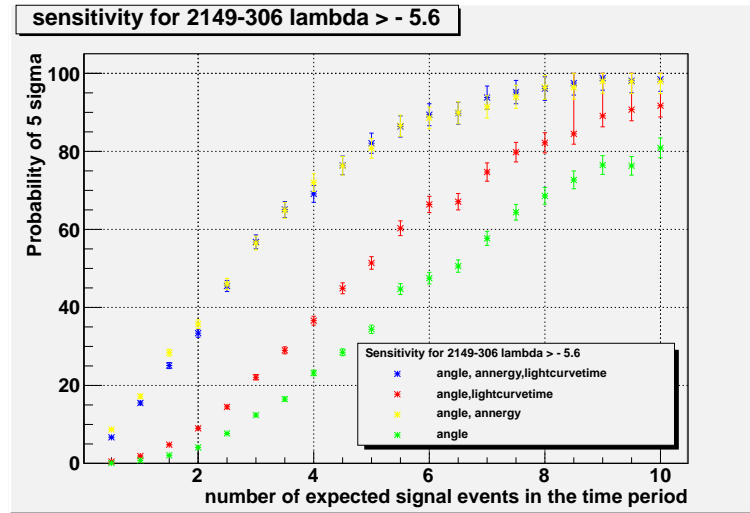
Figure D.7: Optimized sensitivity for PKS 2149-306 with $\lambda > -5.6$. The green points represent the case, when just the angle part is used for the likelihood. The best result is achieved by combining angle, annergy and light-curve time.
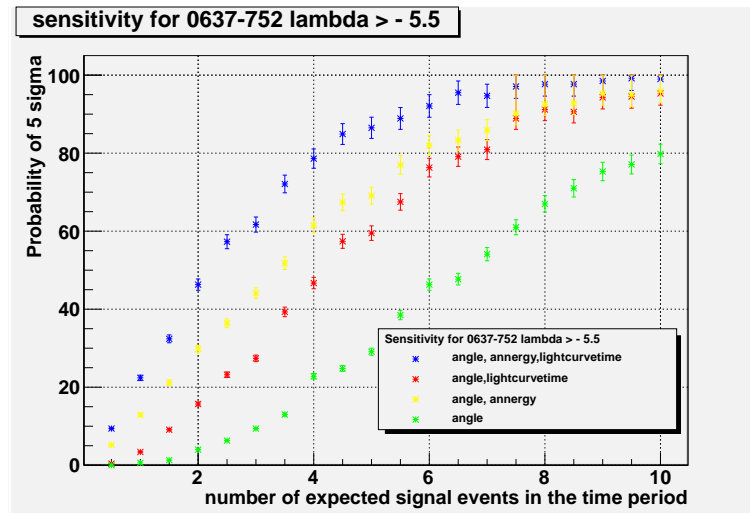
Figure D.8: Optimized sensitivity for PKS 0637-752 with $\lambda > -5.5$. The green points represent the case, when just the angle part is used for the likelihood. The best result is achieved by combining angle, annergy and light-curve time.
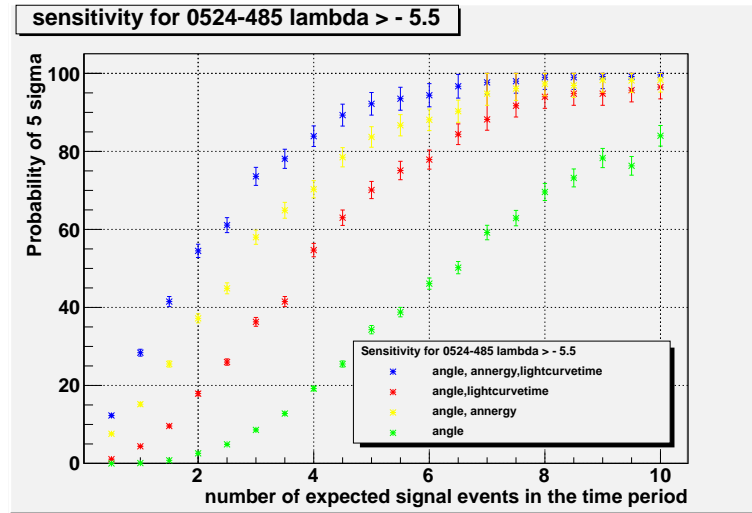
Figure D.9: Optimized sensitivity for PKS 0524-485 with $\lambda > -5.5$. The green points represent the case, when just the angle part is used for the likelihood. The best result is achieved by combining angle, annergy and light-curve time.
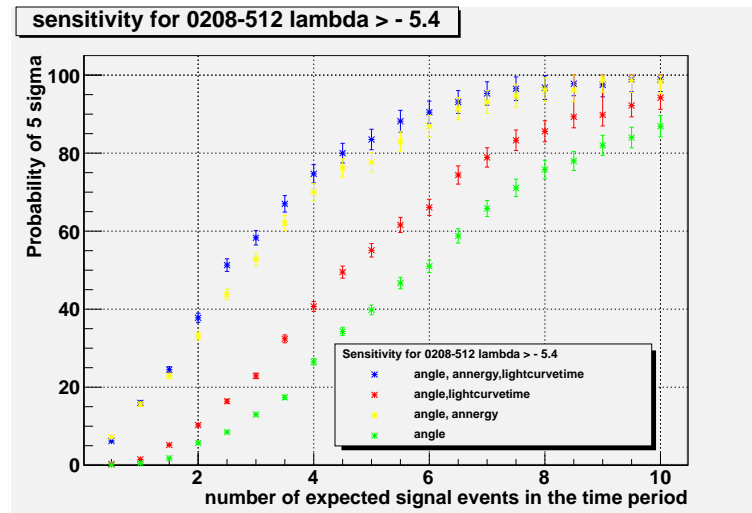
Figure D.10: Optimized sensitivity for PKS 0208-512 with $\lambda > -5.4$. The green points represent the case, when just the angle part is used for the likelihood. The best result is achieved by combining angle, annergy and light-curve time.
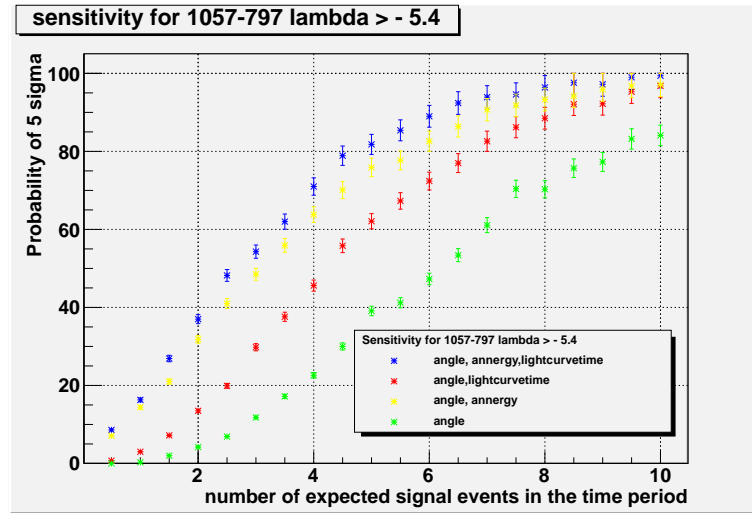
Figure D.11: Optimized sensitivity for PKS 1057-797 with $\lambda > -5.4$. The green points represent the case, when just the angle part is used for the likelihood. The best result is achieved by combining angle, annergy and light-curve time.
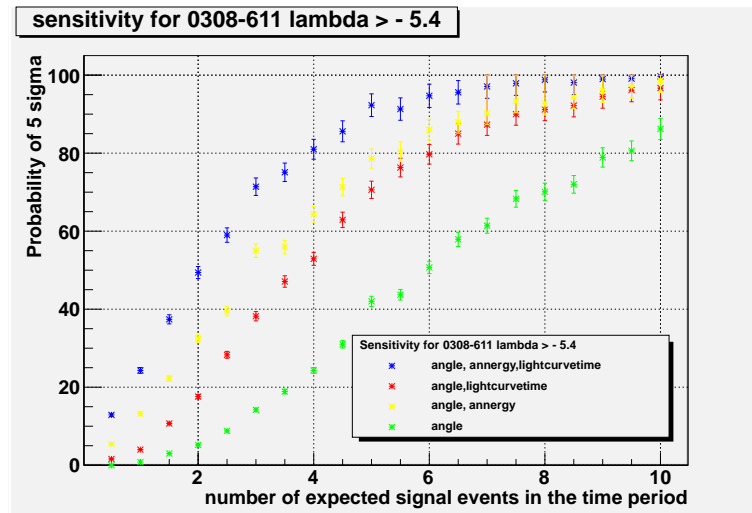
Figure D.12: Optimized sensitivity for PKS 0308-611 with $\lambda > -5.4$. The green points represent the case, when just the angle part is used for the likelihood. The best result is achieved by combining angle, annergy and light-curve time.

E Comparison of sensitivity of all 12 sources
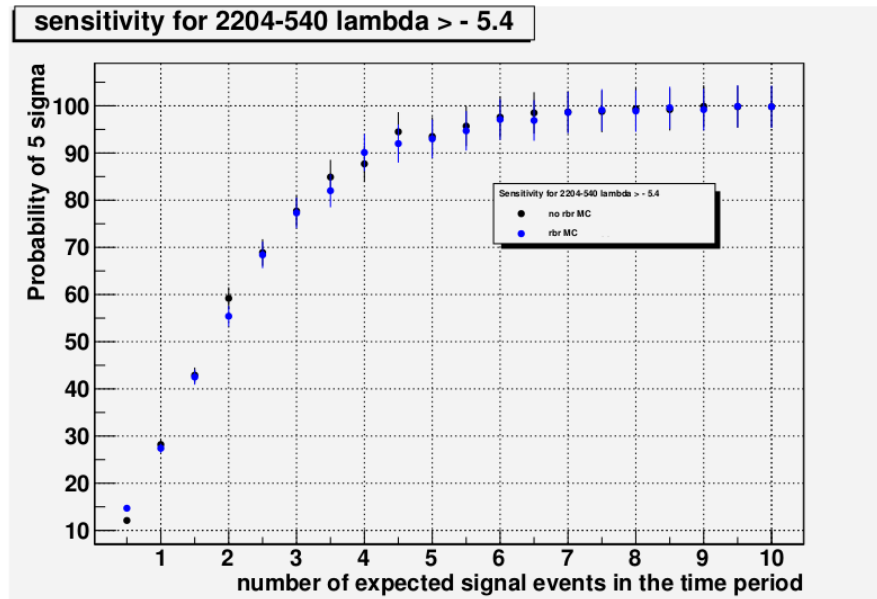
Figure E.1: Comparison of the sensitivity for PKS 2204-540 with $\lambda > -5.4$ in the angle, annergy and light-curve time case. Black points represent the result of the norbrMC analysis, while blue points show the sensitivity in the rbrMC case.
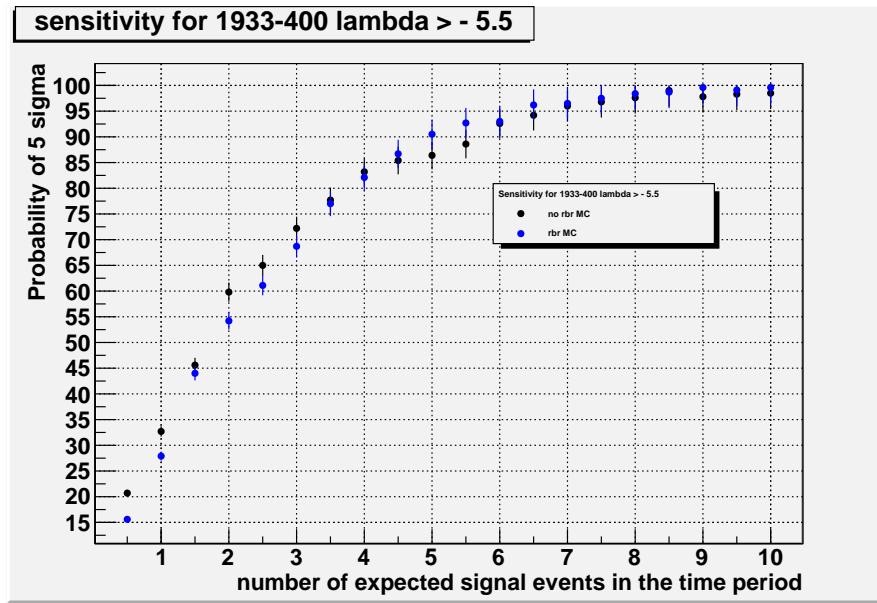
Figure E.2: Comparison of the sensitivity for PKS 1933-400 with $\lambda > -5.5$ in the angle, annergy and light-curve time case. Black points represent the result of the no-rbrMC analysis, while blue points show the sensitivity in the rbrMC case.
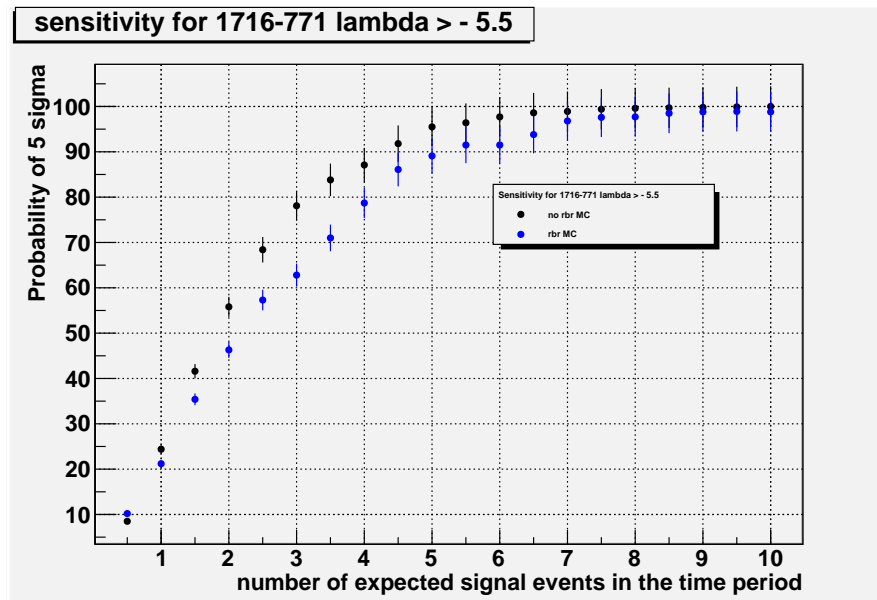
Figure E.3: Comparison of the sensitivity for PKS 1716-771 with $\lambda > -5.5$ in the angle, annergy and light-curve time case. Black points represent the result of the no-rbrMC analysis, while blue points show the sensitivity in the rbrMC case.
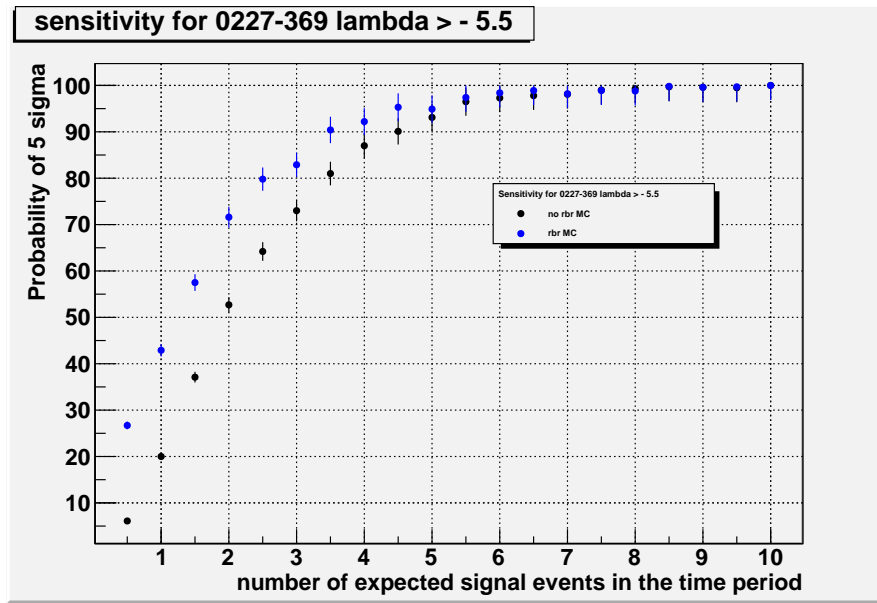
Figure E.4: Comparison of the sensitivity for PKS 0227-369 with $\lambda > -5.5$ in the angle, annergy and light-curve time case. Black points represent the result of the no-rbrMC analysis, while blue points show the sensitivity in the rbrMC case.
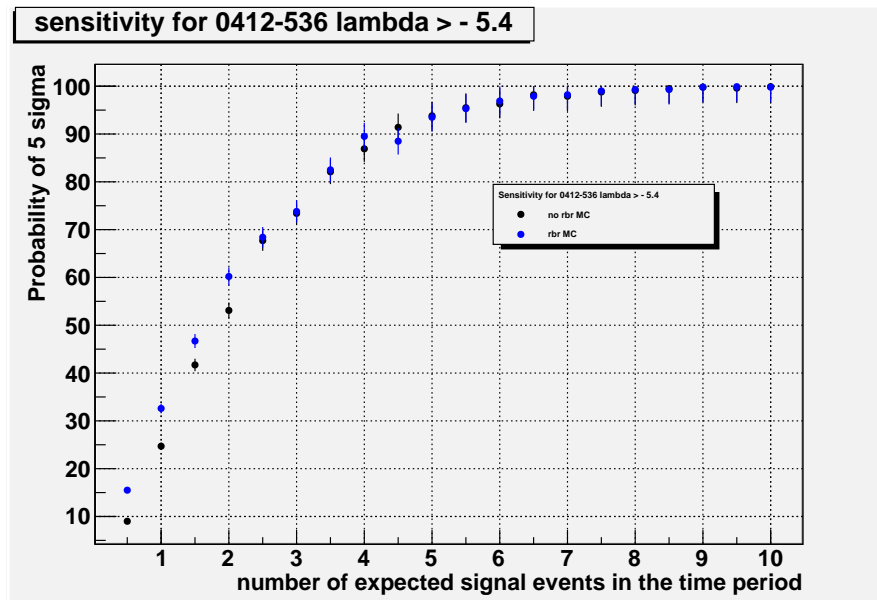
Figure E.5: Comparison of the sensitivity for PKS 0412-536 with $\lambda > -5.4$ in the angle, annergy and light-curve time case. Black points represent the result of the no-rbrMC analysis, while blue points show the sensitivity in the rbrMC case.
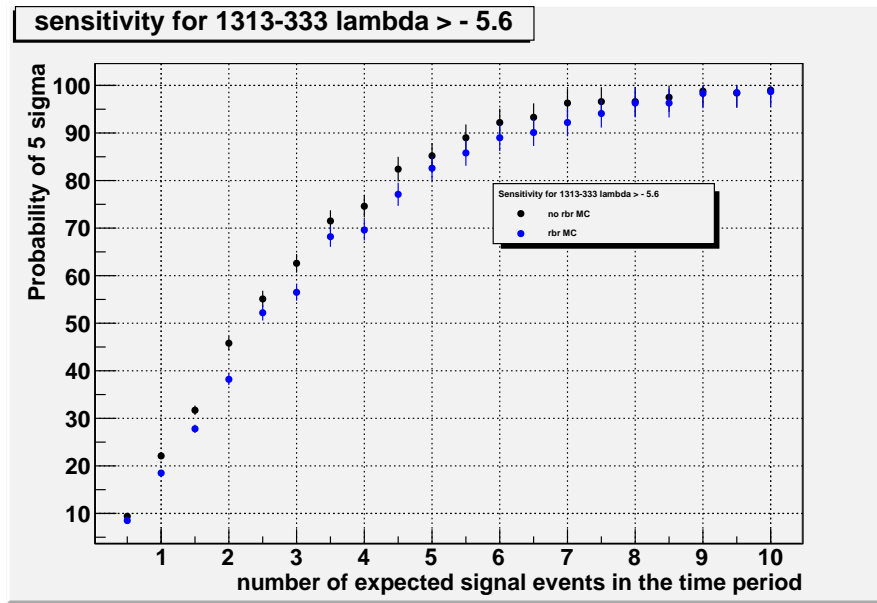
Figure E.6: Comparison of the sensitivity for PKS 1313-333 with $\lambda > -5.6$ in the angle, annergy and light-curve time case. Black points represent the result of the no-rbrMC analysis, while blue points show the sensitivity in the rbrMC case.
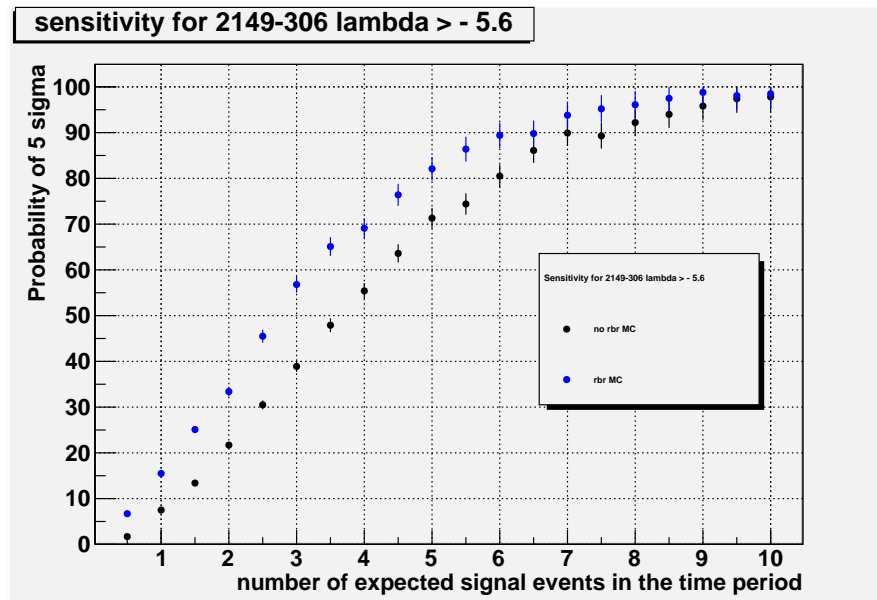
Figure E.7: Comparison of the sensitivity for PKS 2149-306 with $\lambda > -5.6$ in the angle, annergy and light-curve time case. Black points represent the result of the no-rbrMC analysis, while blue points show the sensitivity in the rbrMC case.
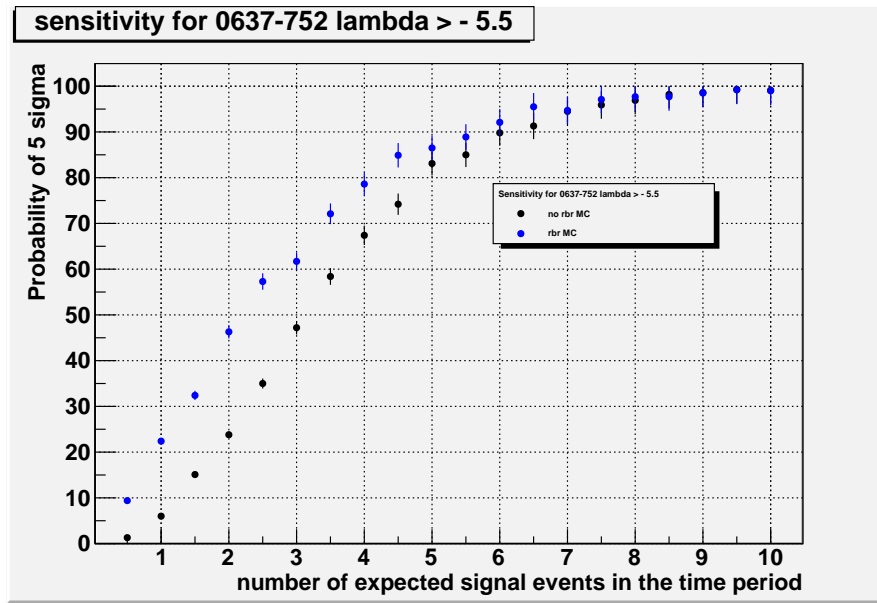
Figure E.8: Comparison of the sensitivity for PKS 0637-752 with $\lambda > -5.5$ in the angle, annergy and light-curve time case. Black points represent the result of the no-rbrMC analysis, while blue points show the sensitivity in the rbrMC case.
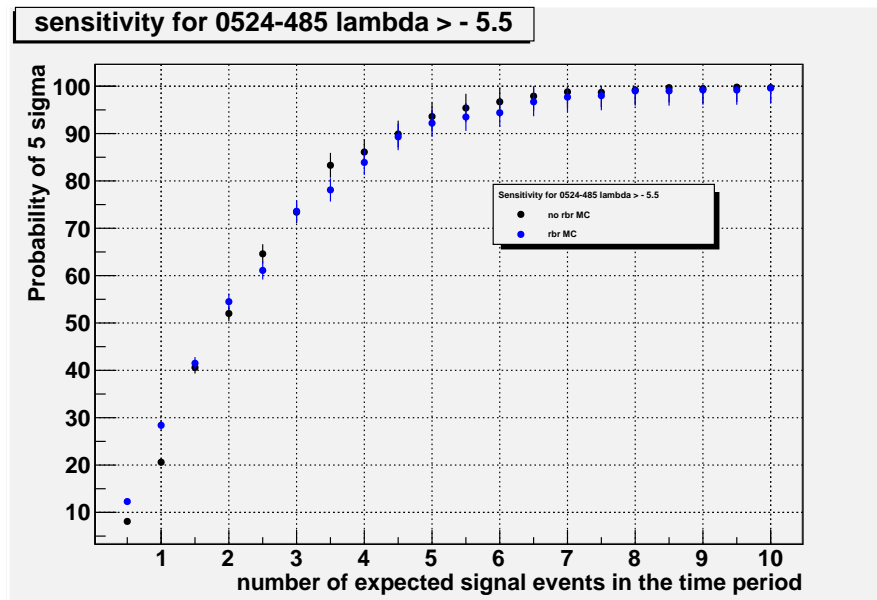
Figure E.9: Comparison of the sensitivity for PKS 0524-485 with $\lambda > -5.5$ in the angle, annergy and light-curve time case. Black points represent the result of the no-rbrMC analysis, while blue points show the sensitivity in the rbrMC case.
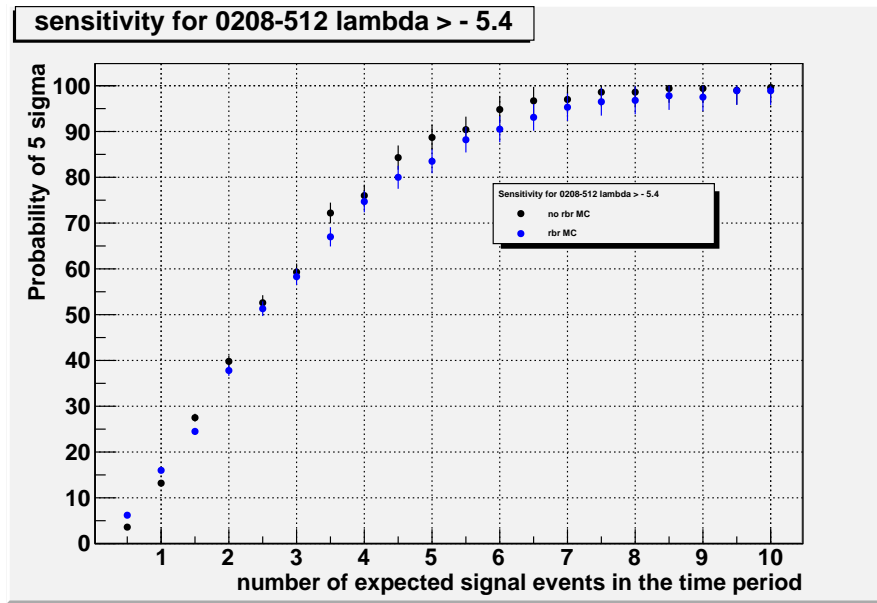
Figure E.10: Comparison of the sensitivity for PKS 0208-512 with $\lambda > -5.4$ in the angle, annergy and light-curve time case. Black points represent the result of the no-rbrMC analysis, while blue points show the sensitivity in the rbrMC case.
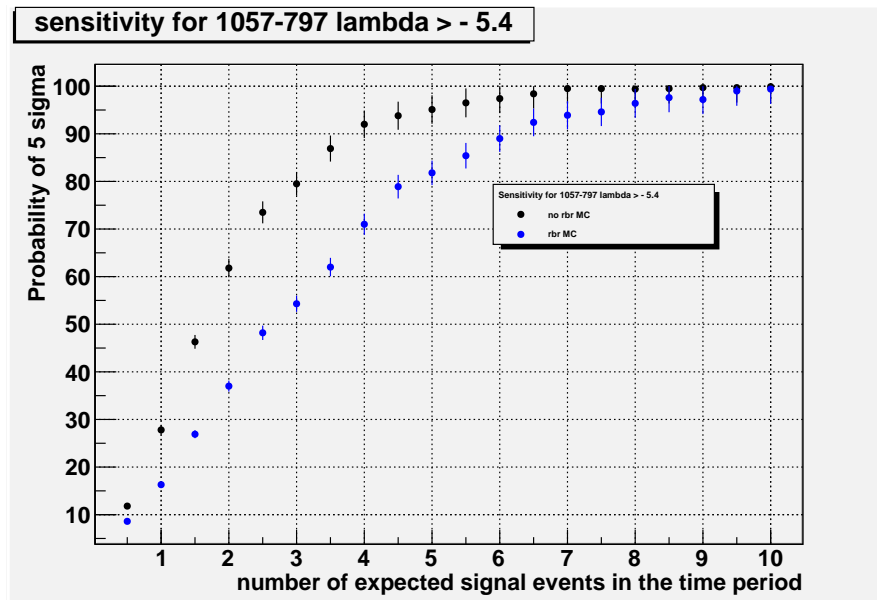
Figure E.11: Comparison of the sensitivity for PKS 1057-797 with $\lambda > -5.4$ in the angle, annergy and light-curve time case. Black points represent the result of the no-rbrMC analysis, while blue points show the sensitivity in the rbrMC case.
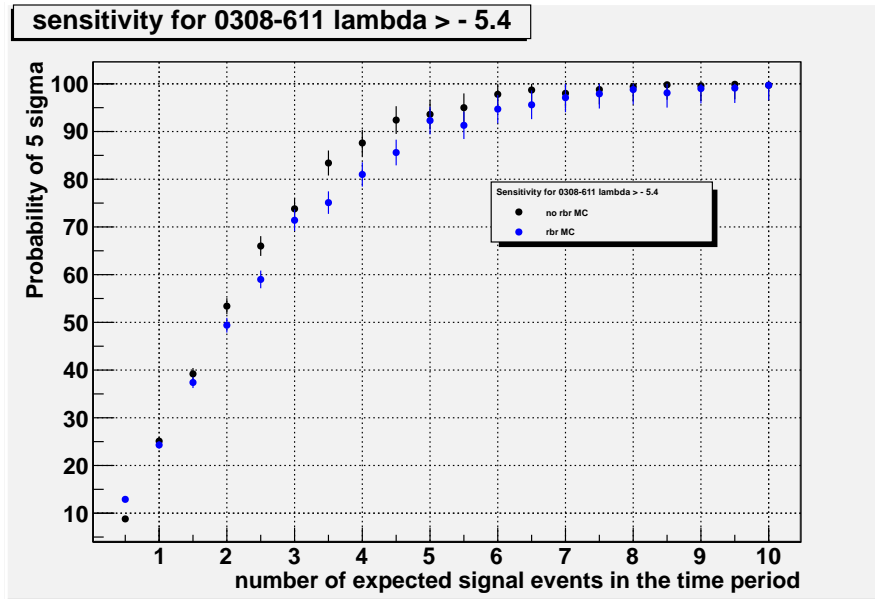
Figure E.12: Comparison of the sensitivity for PKS 0308-611 with $\lambda > -5.4$ in the angle, annergy and light-curve time case. Black points represent the result of the no-rbrMC analysis, while blue points show the sensitivity in the rbrMC case.

F Data Monte Carlo comparison
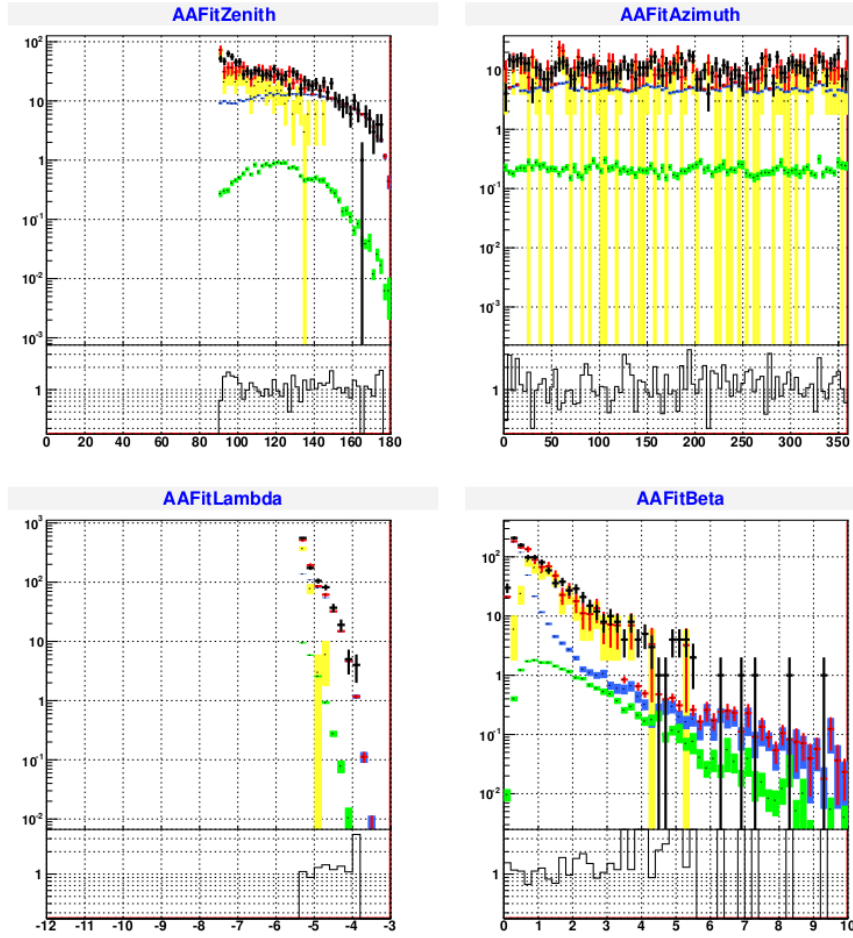
Figure F.1: Data Monte Carlo comparison of runs chosen for PKS 2204-540.
Top: Black shows the triggered data, while red labels the sum of all contributions considered by MC simulations. Different MC events are included in the graph: yellow represents atmospheric mupage events, muons (generated by the event generator GENHEN) are shown in blue and shower events are labeled in green.
Bottom: Comparison of triggered data (black) and sum of total MC (red). As the ratio is fluctuating around unity, the MC models the data in a precise way.
The two plots on the top show the data Monte Carlo comparison for the reconstructed zenith and azimuth angle, using Aafit, while the two plots on the bottom display the comparison for the track quality parameters λ and β (see Sect. 5.2).

Figure F.2: Data Monte Carlo comparison of runs chosen for PKS 1933-400.
Top: Black shows the triggered data, while red labels the sum of all contributions considered by MC simulations. Different MC events are included in the graph: yellow represents atmospheric mupage events, muons (generated by the event generator GENHEN) are shown in blue and shower events are labeled in green.
Bottom: Comparison of triggered data (black) and sum of total MC (red). As the ratio is fluctuating around unity, the MC models the data in a precise way.
The two plots on the top show the data Monte Carlo comparison for the reconstructed zenith and azimuth angle, using Aafit, while the two plots on the bottom display the comparison for the track quality parameters λ and β (see Sect. 5.2).

Figure F.3: Data Monte Carlo comparison of runs chosen for PKS 1716-771.
Top: Black shows the triggered data, while red labels the sum of all contributions considered by MC simulations. Different MC events are included in the graph: yellow represents atmospheric mupage events, muons (generated by the event generator GENHEN) are shown in blue and shower events are labeled in green.
Bottom: Comparison of triggered data (black) and sum of total MC (red). As the ratio is fluctuating around unity, the MC models the data in a precise way.
The two plots on the top show the data Monte Carlo comparison for the reconstructed zenith and azimuth angle, using Aafit, while the two plots on the bottom display the comparison for the track quality parameters λ and β (see Sect. 5.2).

Figure F.4: Data Monte Carlo comparison of runs chosen for PKS 0227-369.
Top: Black shows the triggered data, while red labels the sum of all contributions considered by MC simulations. Different MC events are included in the graph: yellow represents atmospheric mupage events, muons (generated by the event generator GENHEN) are shown in blue and shower events are labeled in green.
Bottom: Comparison of triggered data (black) and sum of total MC (red). As the ratio is fluctuating around unity, the MC models the data in a precise way.
The two plots on the top show the data Monte Carlo comparison for the reconstructed zenith and azimuth angle, using Aafit, while the two plots on the bottom display the comparison for the track quality parameters λ and β (see Sect. 5.2).

Figure F.5: Data Monte Carlo comparison of runs chosen for PKS 0412-536.
Top: Black shows the triggered data, while red labels the sum of all contributions considered by MC simulations. Different MC events are included in the graph: yellow represents atmospheric mupage events, muons (generated by the event generator GENHEN) are shown in blue and shower events are labeled in green.
Bottom: Comparison of triggered data (black) and sum of total MC (red). As the ratio is fluctuating around unity, the MC models the data in a precise way.
The two plots on the top show the data Monte Carlo comparison for the reconstructed zenith and azimuth angle, using Aafit, while the two plots on the bottom display the comparison for the track quality parameters λ and β (see Sect. 5.2).

Figure F.6: Data Monte Carlo comparison of runs chosen for PKS 1313-333.
Top: Black shows the triggered data, while red labels the sum of all contributions considered by MC simulations. Different MC events are included in the graph: yellow represents atmospheric mupage events, muons (generated by the event generator GENHEN) are shown in blue and shower events are labeled in green.
Bottom: Comparison of triggered data (black) and sum of total MC (red). As the ratio is fluctuating around unity, the MC models the data in a precise way.
The two plots on the top show the data Monte Carlo comparison for the reconstructed zenith and azimuth angle, using Aafit, while the two plots on the bottom display the comparison for the track quality parameters λ and β (see Sect. 5.2).

Figure F.7: Data Monte Carlo comparison of runs chosen for PKS 0637-752.
Top: Black shows the triggered data, while red labels the sum of all contributions considered by MC simulations. Different MC events are included in the graph: yellow represents atmospheric mupage events, muons (generated by the event generator GENHEN) are shown in blue and shower events are labeled in green.
Bottom: Comparison of triggered data (black) and sum of total MC (red). As the ratio is fluctuating around unity, the MC models the data in a precise way.
The two plots on the top show the data Monte Carlo comparison for the reconstructed zenith and azimuth angle, using Aafit, while the two plots on the bottom display the comparison for the track quality parameters λ and β (see Sect. 5.2).

Figure F.8: Data Monte Carlo comparison of runs chosen for PKS 0208-512.
Top: Black shows the triggered data, while red labels the sum of all contributions considered by MC simulations. Different MC events are included in the graph: yellow represents atmospheric mupage events, muons (generated by the event generator GENHEN) are shown in blue and shower events are labeled in green.
Bottom: Comparison of triggered data (black) and sum of total MC (red). As the ratio is fluctuating around unity, the MC models the data in a precise way.
The two plots on the top show the data Monte Carlo comparison for the reconstructed zenith and azimuth angle, using Aafit, while the two plots on the bottom display the comparison for the track quality parameters λ and β (see Sect. 5.2).

Figure F.9: Data Monte Carlo comparison of runs chosen for PKS 0308-611.
Top: Black shows the triggered data, while red labels the sum of all contributions considered by MC simulations. Different MC events are included in the graph: yellow represents atmospheric mupage events, muons (generated by the event generator GENHEN) are shown in blue and shower events are labeled in green.
Bottom: Comparison of triggered data (black) and sum of total MC (red). As the ratio is fluctuating around unity, the MC models the data in a precise way.
The two plots on the top show the data Monte Carlo comparison for the reconstructed zenith and azimuth angle, using Aafit, while the two plots on the bottom display the comparison for the track quality parameters λ and β (see Sect. 5.2).

G Final run selection

Runs used in this analysis:

35151 35153 35155 35158 35159 35160 35161 35162 35163 35164 35166 35168 35170 35172 35173 35175 35176 35178 35179 35180 35190
35193 35195 35196 35198 35199 35200 35201 35202 35203 35236 35238 35240 35242 35243 35244 35246 35247 35248 35250 35253 35261
35264 35277 35285 35288 35289 35291 35292 35293 35294 35296 35300 35304 35306 35308 35309 35311 35312 35314 35316 35318 35319
35321 35322 35325 35327 35328 35330 35332 35333 35335 35336 35337 35339 35340 35342 35343 35346 35348 35349 35351 35353 35354
35355 35357 35359 35360 35362 35363 35368 35370 35372 35374 35375 35377 35470 35472 35473 35475 35476 35479 35480 35483 35484
35485 35488 35490 35491 35493 35495 35496 35498 35501 35503 35504 35506 35511 35512 35513 35515 35517 35519 35520 35521 35523
35529 35530 35532 35534 35535 35539 35541 35543 35545 35548 35550 35551 35553 35555 35557 35559 35561 35562 35569 35571 35573
35575 35577 35579 35580 35582 35583 35584 35627 35630 35632 35633 35635 35636 35639 35640 35651 35653 35656 35658 35659 35661
35662 35663 35665 35666 35668 35671 35672 35674 35678 35681 35683 35685 35686 35689 35691 35696 35698 35700 35702 35704 35706
35707 35709 35710 35712 35716 35717 35719 35721 35723 35724 35726 35728 35730 35732 35734 35735 35737 35740 35741 35743 35744
35746 35748 35750 35751 35753 35754 35756 35758 35777 35779 35781 35783 35785 35788 35790 35793 35795 35797 35798 35799 35800
35802 35838 35843 35846 35849 35851 35852 35853 35855 35856 35858 35863 35864 35872 35873 35875 35876 35878 35880 35881 35884
35885 35886 35887 35889 35890 35891 35892 35894 35896 35897 35899 35900 35901 35902 35904 35905 35906 35907 35908 35910 35911
35912 35914 35916 35917 35919 35921 35923 35924 35926 35927 35929 35930 35932 35933 35935 35936 35937 35939 35941 35948 35953
35954 35956 35958 35959 35962 35963 35964 35966 35968 35969 35971 35972 35975 35976 35977 35979 35981 35983 35984 35985 35987
35989 35991 35992 35993 35996 35997 35999 36000 36002 36029 36070 36071 36072 36075 36076 36079 36088 36091 36093 36095 36097
36099 36101 36103 36104 36107 36108 36110 36112 36113 36119 36123 36124 36128 36139 36149 36151 36153 36155 36156 36157 36159
36160 36161 36163 36165 36168 36176 36189 36198 36202 36205 36209 36210 36212 36213 36215 36218 36220 36221 36223 36225 36227
36229 36238 36244 36254 36255 36256 36258 36259 36260 36262 36263 36264 36267 36268 36269 36271 36272 36273 36275 36276 36277
36279 36280 36281 36283 36284 36285 36287 36288 36289 36291 36294 36297 36298 36300 36302 36303 36305 36306 36309 36315 36352
36359 36360 36362 36364 36366 36367 36369 36371 36372 36373 36375 36380 36385 36386 36389 36392 36394 36396 36399 36401 36403
36406 36409 36411 36413 36417 36418 36420 36422 36424 36426 36428 36430 36431 36434 36435 36436 36438 36439 36442 36443 36444
36446 36448 36450 36452 36456 36458 36459 36461 36466 36467 36469 36471 36473 36474 36475 36477 36478 36480 36481 36483 36484
36485 36488 36489 36491 36492 36494 36495 36497 36498 36500 36501 36502 36505 36506 36507 36509 36511 36512 36514 36516 36517
36519 36532 36534 36543 36548 36549 36551 36552 36555 36556 36557 36570 36572 36576 36577 36582 36587 36590 36592 36593 36594
36596 36598 36599 36603 36605 36607 36623 36624 36663 36724 36725 36734 36736 36738 36740 36742 36745 36747 36749 36750 36752
36755 36759 36761 36763 36772 36775 36776 36783 36785 36786 36787 36789 36791 36826 36835 36836 36837 36850 36853 36858 36860
36862 36863 36865 36867 36869 36870 36872 36874 36877 36879 36881 36883 36885 36887 36889 36891 36892 36893 36895 36897 36898
36900 36901 36903 36904 36906 36907 36908 36911 36914 36915 36918 36922 36923 36925 36926 36927 36929 36930 36932 36934 36935
36938 36939 36940 36942 36943 36945 36947 36948 36950 36951 36953 36956 36957 36958 36960 36961 36963 36964 36966 36968 36970
36973 36975 36978 37015 37016 37018 37019 37021 37024 37025 37026 37028 37029 37031 37033 37035 37037 37044 37045 37047 37049
37051 37053 37055 37057 37061 37064 37065 37068 37070 37072 37073 37075 37076 37078 37081 37082 37084 37085 37090 37091 37093
37095 37096 37098 37099 37103 37104 37105 37107

Table 9: Final list of runs used for this analysis

37108 37109 37111 37112 37114 37115 37118 37119 37121 37123 37125 37128 37130 37132 37134 37137 37139 37141 37142 37144 37146
37147 37149 37150 37151 37153 37155 37158 37159 37161 37163 37165 37167 37169 37171 37176 37209 37211 37213 37215 37217 37218
37220 37222 37224 37226 37228 37230 37231 37234 37236 37238 37239 37241 37242 37246 37248 37249 37251 37252 37253 37255 37257
37259 37261 37263 37266 37268 37271 37272 37276 37280 37281 37283 37284 37285 37287 37289 37291 37292 37293 37296 37297 37300
37301 37302 37304 37305 37307 37308 37309 37312 37313 37314 37316 37317 37319 37320 37321 37323 37324 37327 37328 37330 37331
37332 37334 37335 37337 37339 37342 37344 37346 37348 37349 37350 37352 37353 37389 37391 37393 37395 37397 37399 37402 37404
37407 37409 37412 37415 37417 37419 37420 37423 37424 37426 37428 37430 37432 37434 37436 37437 37439 37440 37442 37443 37445
37447 37448 37450 37452 37454 37455 37456 37458 37459 37461 37462 37463 37465 37466 37468 37470 37471 37473 37601 37603 37605
37607 37608 37616 37618 37619 37620 37622 37623 37625 37632 37634 37635 37637 37638 37644 37650 37651 37653 37655 37656 37658
37659 37662 37664 37668 37670 37672 37673 37675 37678 37679 37682 37683 37685 37687 37688 37689 37701 37712 37714 37716 37717
37719 37720 37722 37723 37731 37732 37733 37735 37736 37738 37739 37741 37744 37746 37751 37752 37753 37755 37757 37759 37761
37763 37764 37765 37767 37768 37770 37771 37772 37774 37780 37782 37783 37785 37788 37871 37873 37874 37990 37992 37993 37994
37996 37997 37999 38002 38004 38007 38009 38011 38045 38052 38054 38056 38058 38060 38063 38065 38067 38070 38072 38074 38075
38076 38078 38080 38082 38084 38086 38088 38090 38093 38095 38097 38099 38100 38102 38104 38106 38108 38110 38112 38113 38115
38117 38118 38119 38121 38122 38123 38125 38126 38128 38129 38153 38155 38156 38157 38158 38159 38168 38177 38179 38180 38182
38183 38185 38187 38188 38190 38193 38195 38196 38197 38199 38200 38202 38204 38205 38207 38208 38209 38211 38212 38213 38215
38216 38218 38223 38225 38227 38228 38230 38241 38242 38244 38391 38397 38398 38400 38402 38403 38404 38406 38407 38410 38421
38423 38424 38426 38427 38429 38431 38432 38435 38438 38440 38442 38443 38445 38447 38448 38450 38451 38461 38463 38465 38466
38467 38470 38472 38474 38475 38477 38478 38480 38481 38485 38486 38488 38489 38491 38492 38493 38495 38496 38500 38502 38503
38504 38506 38511 38512 38515 38517 38518 38519 38520 38521 38523 38524 38526 38527 38529 38533 38534 38536 38537 38539 38540
38542 38543 38546 38548 38549 38551 38552 38554 38555 38557 38558 38560 38562 38569 38571 38572 38574 38575 38577 38578 38581
38582 38583 38585 38586 38588 38589 38590 38599 38600 38601 38610 38611 38612 38614 38615 38620 38621 38623 38625 38626 38628
38629 38631 38632 38634 38635 38636 38639 38640 38641 38643 38645 38646 38647 38649 38650 38652 38654 38656 38658 38685 38687
38688 38690 38691 38692 38695 38696 38697 38699 38700 38702 38703 38711 38712 38716 38717 38719 38720 38722 38723 38724 38726
38727 38738 38739 38741 38742 38744 38745 38747 38748 38750 38752 38753 38755 38756 38773 38780 38793 38795 38796 38799 38800
38801 38803 38805 38806 38807 38809 38810 38813 38814 38823 38824 38826 38827 38829 38830 38833 38834 38835 38837 38838 38840
38841 38843 38844 38847 38849 38850 38852 38853 38855 38856 38869 38899 38900 38902 38903 38905 38906 38908 38909 38913 38917
38918 38925 38926 38928 38929 38931 38932 38934 38936 38938 38940 38941 38943 38944 38946 38947 38949 38951 38953 38954 38955
38957 38958 38960 38961 38962 38965 38966 38968 38969 38971 38972 38974 38975 38977 38978 38980 38982 38983 38985 38986 38988
38989 38990 38992 38994 38996 38997 38999 39000 39001 39003 39004 39006 39008 39015 39021 39022 39025 39028 39030 39031 39033
39034 39036 39037 39038 39040 39042 39044 39045 39047 39048 39049 39051 39052 39054 39056 39057 39059 39060 39062 39063 39065
39066 39067 39069 39071 39072 39074 39076 39078 39079 39080 39082 39083 39085 39086 39087 39090 39091 39095 39104 39105 39106
39108 39109 39111 39112 39114 39116 39117 39119 39120 39122 39124 39125 39127 39128 39131 39133 39144 39147 39150 39151 39157
39161 39168 39169 39180 39196 39197 39199 39204 39205 39207 39209 39211 39212 39214 39215 39217 39218 39220 39221 39223 39225
39227 39228 39229 39231 39232 39234 39235 39237 39238 39240 39242 39244 39246 39247 39249 39250 39254 39255 39257 39259 39260
39262 39263 39265 39266 39273 39307 39313 39319 39321 39324 39327 39331 39339 39341 39342 39345 39349 39351 39357 39360 39362
39364 39365 39369 39372 39373 39377 39379 39381 39382 39384 39387 39389 39391 39393 39395 39398 39400 39410 39420 39425 39427
39430 39432 39438 39442 39453 39456 39458 39460 39564 39565 39567 39569 39570 39573 39575 39580 39581 39583 39586 39589 39590
39603 39609 39617 39620 39623 39625 39627 39629 39631 39633 39636 39638 39640 39642 39644 39647 39649 39652 39662 39669 39671
39673 39675 39677 39680 39682 39683 39685 39689 39700 39702 39705 39707 39711 39712 39713 39717 39718 39723 39725 39726 39727
39728 39729 39757 39760 39762 39763 39765 39772 39774 40098 40119 40150 40152 40154 40155 40157 40160 40161 40167 40169 40171
40177 40179 40189 40191 40195 40197 40199 40213 40216 40453 40473 40475 40507 40509 40516 40530 40545 40553 40555 40591 40594
40603 40606 40608 40616 40618 40623 40647 40649 40653 40655 40657 40659 40663 40664 40666 40668 40669 40672 40675 40676 40677
40678 40681 40682 40684 40686 40688 40690 40691 40695 40697 40698 40705 40706 40707 40709 40712 40713 40714 40716 40717 40718
40719 40721 40722 40741 40751 40753 40756 40758 40762 40763 40765 40766 40768 40777 40780 40783 40784 40786 40788 40870 40872
40879 40880 40884 40959 40962 41208 41212 41214 41215 41261 41262 41268 41270 41279 41281 41283 41285 41287 41289 41292 41295
41301 41303 41305 41308 41310 41313 41314 41316 41318 41320 41350 41352 41353 41365 41367 41369 41370 41373 41374 41376 41377
41400 41402 41403 41404 41406 41408 41416 41417 41418 41421 41423 41424 41426 41428 41429 41430 41431 41433 41434 41435 41437
41439 41440 41441 41442 41450 41524 41528 41534 41536 41538 41540 41543

Table 10: Final list of runs used for this analysis

37608 38744 41546 41548 41550 41552 41555 41557 41560 41563 41567 41605 41608 41614 41630 41631 41632 41633 41634 41635 41661
41662 41665 41666 41673 41675 41677 41679 41699 41702 41703 41706 41711 41712 41714 41715 41740 41742 41744 41852 41854 41980
41982 41984 41986 41988 41991 41993 41995 42042 42056 42086 42090 42091 42096 42102 42109 42111 42114 42116 42117 42119 42121
42264 42417 42420 42425 42477 42482 42494 42497 42500 42502 42504 42515 42518 42521 42523 42526 42528 42530 42533 42536 42541
42543 42545 42547 42550 42554 42577 42580 42585 42588 42592 42594 42597 42602 42606 42609 42612 42616 42623 42625 42628 42631
42634 42638 42640 42643 42646 42649 42652 42655 42658 42661 42668 42686 42756 42758 42765 42771 42777 42781 42785 42792 42796
42799 42804 42810 42811 42815 42819 42821 42825 42829 42831 42835 42838 42842 42851 42856 42860 42863 42866 42889 42893 42897
42900 42906 42909 42912 42922 42926 42932 42936 42941 42944 42950 42954 42959 42962 42964 42967 42971 42973 42976 42983 42986
42990 42994 42997 43003 43007 43010 43015 43040 43046 43059 43062 43069 43073 43078 43081 43086 43098 43108 43161 43169 43173
43176 43180 43183 43185 43191 43199 43219 43222 43226 43229 43234 43237 43240 43242 43245 43250 43256 43258 43262 43265 43271
43274 43325 43366 43379 43385 43546 43551 43555 43563 43568 43574 43584 43587 43591 43596 43600 43606 43610 43612 43615 43620
43624 43627 43629 43632 43634 43639 43646 43649 43653 43657 43663 43666 43669 43673 43681 43689 43692 43695 43698 43701 43705
43710 43713 43716 43719 43722 43725 43728 43731 43734 43737 43741 43743 43745 43748 43751 43758 43760 43764 43769 43773 43776
43778 43782 43787 43796 43800 43806 43812 43817 43823 43826 43831 43834 43837 43842 43846 43849 43852 43890 43905 43911 43922
43925 43930 43932 43936 43940 43959 43964 43974 43978 43981 43984 43987 43991 43999 44003 44007 44010 44013 44016 44018 44020
44025 44029 44037 44040 44042 44045 44049 44053 44056 44060 44064 44072 44075 44078 44081 44083 44087 44089 44098 44228 44285
44289 44293 44296 44298 44304 44307 44311 44315 44322 44334 44338 44340 44344 44348 44353 44356 44364 44367 44372 44375 44378
44395 44400 44423 44426 44473 44485 44487 44491 44497 44499 44502 44513 44529 44532 44539 44544 44556 44560 44564 44566 44568
44574 44577 44580 44583 44585 44588 44596 44598 44602 44605 44608 44611 44614 44617 44620 44623 44633 44637 44640 44644 44648
44653 44656 44666 44824 44833 44835 44840 44860 45000 45030 45040 45050 45054 45058 45061 45065 45069 45071 45102 45105 45108
45110 45112 45116 45128 45134 45138 45140 45142 45145 45147 45168 45169 45172 45177 45179 45181 45183 45188 45191 45193 45196
45202 45210 45212 45222 45225 45227 45229 45232 45234 45238 45243 45248 45250 45254 45256 45259 45265 45267 45271 45274 45275
45277 45279 45285 45287 45290 45291 45295 45326 45332 45338 45342 45349 45354 45356 45363 45367 45379 45388 45391 45393 45408
45412 45418 45419 45431 45435 45438 45440 45442 45444 45446 45448 45468 45470 45472 45477 45479 45485 45487 45489 45495 45540
45544 45546 45551 45557 45561 45563 45565 45567 45577 45586 45589 45592 45595 45598 45601 45617 45663 45665 45681 45687 45689
45692 45697 45700 45701 45703 45705 45707 45710 45714 45717 45719 45721 45724 45726 45728 45730 45746 45749 45750 45753 45755
45757 45759 45761 45766 45768 45771 45773 45775 45776 45778 45780 45784 45788 45790 45795 45797 45800 45802 45804 45807 45812
45814 45816 45818 45820 45822 45825 45827 45829 45831 45833 45835 45838 45841 45843 45845 45848 45851 45853 45855 45858 45860
45862 45864 45867 45869 45871 45873 45875 45877 45879 45881 45884 45905 45909 45912 45936 45938 45940 45942 45944 45946 45952
45956 45958 45960 45962 45964 45966 45971 45976 45978 45981 45983 45985 45987 45991 45994 45996 45998 46001 46003 46006 46009
46011 46014 46016 46018 46020 46022 46026 46027 46030 46033 46036 46039 46040 46043 46045 46048 46050 46052 46054 46092 46094
46097 46099 46101 46102 46104 46106 46109 46112 46118 46120 46122 46133 46135 46137 46147 46353 46356 46360 46362 46367 46369
46383 46388 46389 46392 46394 46396 46399 46401 46404 46406 46407 46409 46411 46413 46415 46418 46420 46422 46423 46425 46428
46430 46432 46434 46438 46442 46449 46451 46453 46455 46457 46460 46462 46464 46468 46469 46472 46474 46475 46478 46480 46482
46485 46498 46500 46531 46533 46536 46538 46540 46542 46544 46546 46549 46551 46554 46574 46576 46584 46586 46591 46593 46595
46605 46670 46694 46696 46707 46855 46858 46861 46863 46865 46869 46916 46955 47210 47214 47218 47223 47228 47236 47238 47241
47575 47577 47599 47601 47674 47676 47682 47688 47692 47694 47706 47708 47801 47830 47833 47835 47836 47838 47840 47843 47846
47859 47861 47862 47865 47866 47868 47870 47878 47879 47882 47883 47943 47947 47949 47951 47969 48140 48146 48148 48179 48181
48182 48184 48276 48461 48463 48465 48466 48468 48471 48472 48474 48476 48478 48482 48484 48487 48488 48490 48492 48494 48495
48512 48514 48515 48517 48518 48904 48909 48929 48931 48932 48934 48937 48939 48943 48945 48947 48950 48953 48956 48966 49360
49362 49366 49369 49372 49375 49388 49393 49395 49396 49398 49401 49403 49413 49660 49661 49669 49672 49685 49689 49693 49696
49699 49701 49703 49706 49708 49709 49710 49712 49715 49722 49725 49728 49731 49733 49737 49740 49741 49743 49745 49755 49757
49759 49764 49770 49773 49777 49853 49858 49860 49863 49872 49897 49900 49902 49906 49908 49911 49914 49932 49942 49945 49948
49951 49954 49958 49980 49983 49986 49989 49991 49995 50002 50012 50016 50018 50021 50023 50026 50028 50030 50032 50035 50037
50038 50046 50049 50063 50064 50068 50069 50071 50072 50198 50211 50216 50218 50346 50348 50351 50355 50359 50361 50377 50379
50383 50386 50388 50390 50391 50411 50416 50771 50785 50789 50792 50796 50802 50821 50824 50826 50829 50832 50834 50837 50839
50843 50845 50848 50850 50861 50863 50867 50874 50877 50878 50880 50882 50884 50887 50889 50891 50897 50901 50914 50937 50941
50943 50947 50951 50955 50958 50960 50964 50990 50999 51002 51003 51005 51007 51009 51011 51013 51014 51017 51070 51072 51079
51083 51085 51088 51092 51094 51097 51101 51104 51107 51110 51113 51116 51118 51122

Table 11: Final list of runs used for this analysis

37608 38744 51124 51127 51130 51132 51133 51136 51138 51140 51144 51146 51149 51152 51154 51156 51158 51160 51162 51163 51165
51166 51168 51169 51172 51174 51175 51177 51179 51199 51207 51216 51222 51223 51225 51226 51228 51230 51232 51234 51235 51237
51238 51241 51242 51245 51246 51251 51252 51254 51256 51257 51260 51261 51263 51264 51266 51268 51271 51273 51274 51276 51278
51285 51290 51292 51295 51299 51301 51305 51312 51315 51320 51323 51326 51327 51330 51332 51334 51336 51337 51339 51341 51343
51345 51348 51354 51358 51359 51362 51367 51370 51373 51375 51379 51382 51384 51390 51393 51396 51399 51403 51406 51409 51411
51413 51423 51435 51488 51493 51497 51499 51503 51506 51511 51514 51529 51531 51536 51538 51541 51544 51547 51549 51550 51552
51553 51555 51558 51559 51561 51564 51566 51568 51572 51574 51576 51578 51580 51582 51584 51586 51588 51589 51591 51594 51596
51598 51600 51603 51605 51607 51609 51614 51616 51630 51632 51634 51636 51638 51641 51645 51648 51657 51669 51684 51686 51690
51692 51695 51697 51834 51835 51838 51840 51842 51844 51846 51848 51850 51853 51855 51857 51859 51861 51863 51865 51868 51870
51872 51876 51879 51881 51883 51885 51886 51897 51899 51901 51903 51905 51906 51908 51909 51912 51914 51916 51917 51919 51921
51923 51924 51926 51929 51931 51933 51934 51936 51938 51941 51943 51964 51965 51967 51969 51971 51975 51977 51979 51983 51984
51986 51988 51989 51991 51993 51994 51997 51999 52001 52002 52004 52006 52007 52009 52011 52013 52017 52019 52021 52023 52025
52026 52028 52031 52032 52041 52043 52044 52046 52055 52057 52073 52075 52083 52085 52087 52098 52101 52116 52119 52125 52128
52131 52133 52136 52138 52139 52142 52145 52147 52149 52151 52155 52157 52159 52162 52164 52166 52169 52171 52174 52178 52179
52182 52184 52186 52187 52189 52191 52193 52195 52197 52199 52201 52202 52204 52206 52208 52209 52212 52216 52220 52240 52242
52244 52246 52247 52250 52252 52254 52258 52260 52261 52263 52265 52268 52269 52271 52276 52278 52280 52292 52293 52307 52309
52335 52337 52347 52350 52361 52363 52365 52366 52368 52376 52377 52393 52395 52404 52406 52408 52409 52411 52413 52414 52417
52419 52421 52423 52425 52426 52428 52430 52433 52435 52437 52439 52441 52442 52444 52447 52449 52451 52453 52455 52456 52458
52460 52463 52465 52467 52469 52471 52473 52475 52478 52479 52481 52483 52485 52487 52489 52491 52493 52495 52497 52499 52502
52504 52506 52509 52511 52513 52515 52517 52518 52521 52523 52526 52528 52530 52532 52533 52535 52537 52539 52542 52545 52547
52557 52563 52671 52673 52676 52678 52679 52681 52685 52687 52689 52705 52707 52710 52712 52713 52715 52717 52719 52721 52732
52733 52735 52737 52739 52741 52742 52750 52752 52754 52756 52758 52759 52761 52764 52767 52769 52771 52772 52774 52776 52779
52781 52783 52784 52786 52788 52790 52799 52824 52826 52827 52829 52831 52835 52837 52838 52840 52843 52845 52848 52850 52853
52880 52882 52884 52885 52886 52977 52979 52981 52985 52987 52989 52992 52994 52996 52998 53000 53003 53005 53007 53008 53009
53014 53016 53019 53025 53027 53028 53031 53032 53034 53037 53039 53041 53042 53044 53045 53047 53049 53050 53052 53054 53055
53057 53059 53060 53062 53064 53066 53068 53070 53072 53075 53077 53079 53080 53082 53084 53085 53087 53089 53091 53093 53094
53097 53099 53100 53102 53103 53105 53107 53109 53110 53112 53113 53116 53118 53119 53122 53126 53127 53131 53135 53140 53144
53148 53151 53153 53154 53156 53158 53159 53161 53162 53164 53175 53177 53179 53214 53216 53218 53223 53224 53226 53229 53230
53232 53234 53235 53237 53238 53240 53241 53243 53245 53246 53248 53249 53251 53253 53254 53256 53257 53259 53261 53262 53264
53265 53267 53269 53270 53272 53274 53275 53277 53279 53280 53282 53284 53285 53287 53288 53290 53292 53293 53295 53297 53298
53300 53302 53303 53305 53306 53308 53350 53352 53353 53355 53356 53358 53359 53361 53363 53364 53365 53367 53368 53371 53373
53374 53376 53378 53379 53381 53383 53384 53408 53410 53412 53413 53415 53417 53418 53420 53422 53423 53425 53427 53428 53431
53433 53434 53436 53438 53439 53441 53443 53445 53446 53448 53450 53451 53453 53455 53456 53458 53460 53461 53463 53465 53466
53467 53469 53471 53472 53474 53476 53477 53479 53481 53482 53484 53486 53489 53490 53492 53493 53495 53497 53498 53500 53502
53503 53505 53507 53510 53512 53514 53516 53517 53519 53520 53522 53523 53525 53527 53528 53531 53533 53534 53536 53537 53539
53541 53543 53545 53547 53548 53550 53552 53553 53555 53557 53559 53561 53563 53565 53568 53570 53571 53573 53575 53576 53578
53580 53581 53583 53584 53586 53588 53589 53592 53594 53595 53597 53600 53601 53603 53605 53607 53608 53610 53612 53613 53615
53617 53618 53620 53622 53623 53625 53627 53628 53631 53633 53635 53637 53639 53641 53642 53644 53646 53647 53649 53651 53654
53656 53657 53660 53662 53664 53665 53667 53669 53670 53672 53674 53675 53677 53679 53680 53682 53683 53685 53687 53688 53690
53692 53693 53695 53696 53698 53700 53701 53703 53704 53706 53707 53708 53710 53712 53714 53715 53718 53719 53721 53724 53726
53728 53730 53732 53734 53736 53739 53741 53743 53745 53747 53749 53751 53753 53755 53756 53758 53760 53762 53764 53766 53768
53770 53772 53773 53777 53779 53781 53783 53785 53787 53804 53806 53808 53809 53811 53813 53814 53818 53819 53820 53822 53823
53825 53826 53828 53830 53832 53834 53836 53854 53856 53857 53859 53860 53862 53863 53865 53866 53868 53869 53900 53901 53903
53904 53905 53907 53909 53910 53912 53914 53916 53917 53919 53927 53928 53932 53933 53935 53937 53938 53940 53943 53945 53948
53950 53952 53953 53966 53968 53969 53983 53986 54029 54031 54033 54034 54036 54037 54039 54041 54042 54043 54045 54047 54049
54050 54052 54053 54054 54056 54057 54059 54060 54062 54063 54065 54066 54088 54089 54091 54093 54094 54096 54097 54099 54100
54102 54103 54105 54107 54108 54110 54111 54113 54115 54116 54118 54119 54121 54123 54124 54129 54131 54133 54158 54161 54167
54169 54171 54173 54175 54177 54179 54181 54182 54184 54186 54188 54189 54191 54193 54194 54196 54198 54199 54201 54202 54204
54205 54207 54209 54210 54212 54213 54215 54217 54218 54220 54222 54224 54226 54228

Table 12: Final list of runs used for this analysis

37608 38744 54229 54231 54233 54234 54236 54237 54239 54241 54242 54244 54246 54247 54249 54250 54253 54255 54257 54258 54260

54261 54263 54265 54266 54268 54269 54271 54272 54275 54277 54279 54281 54283 54284 54286 54287 54289 54290 54292 54294 54295

54297 54298 54300 54301 54303 54305 54306 54309 54311 54312 54314 54315 54317 54319 54320 54322 54323 54325 54326 54328 54330

54331 54333 54334 54336 54337 54339 54341 54342 54344 54345 54347 54348 54350 54351 54365 54366 54368 54370 54371 54373 54374

54376 54378 54379 54381 54382 54384 54385 54387 54388 54390 54391 54393 54394 54396 54397 54399 54401 54403 54405 54406 54408

54410 54412 54414 54415 54417 54418 54423 54425 54426 54428 54429 54431 54434 54436 54437 54439 54441 54443 54445 54447 54449

54451 54453 54454 54456 54457 54459 54461 54462 54464 54465 54473 54475 54476 54478 54479 54481 54483 54588 54606 54608 54610

54612 54614 54616 54618 54619 54621 54623 54624 54626 54627 54629 54630 54632 54634 54635 54637 54638 54640 54642 54644 54646

54648 54649 54651 54653 54654 54656 54658 54671 54673 54675 54676 54678 54680 54681 54683 54685 54686 54690 54692 54693 54695

54697 54698 54700 54702 54703 54705 54707 54708 54710 54712 54714 54715 54717 54719 54720 54722 54724 54725 54727 54730 54732

54733 54738 54740 54742 54744 54745 54747 54749 54751 54752 54754 54756 54758 54760 54761 54763 54765 54767 54769 54771 54772

54774 54776 54778 54779 54781 54783 54785 54786 54788 54789 54791 54793 54795 54796 54798 54799 54801 54802 54804 54805 54807

54811 54818 54820 54822 54824 54826 54827 54829 54831 54832 54834 54837 54838 54840 54842 54844 54846 54849 54850 54852 54856

54857 54859 54860 54862 54885 54887 54889 54890 54893 54895 54897 54898 54900 54902 54903 54905 54906 54908 54910 54914 54916

54917 54919 54921 54922 54924 54925 54931 54933 54935 54937 54938 54940 54942 54943 54945 54947 54948 54950 54952 54953 54967

54969 54971 54972 54974 54975 54977 54978 54980 54982 55001 55003 55004 55006 55008 55010 55012 55014 55016 55018 55020 55021

55024 55025 55028 55030 55032 55033 55035 55037 55038 55040 55042 55043 55045 55047 55048 55050 55052 55054 55055 55057 55059

55061 55062 55069 55071 55073 55074 55076 55078 55080 55081 55083 55085 55086 55088 55090 55092 55093 55095 55097 55099 55101

55103 55105 55106 55108 55110 55112 55114 55115 55117 55119 55121 55124 55126 55142 55144 55146 55147 55149 55151 55173 55176

55177 55178 55180 55182 55183 55185 55208 55210 55232 55233 55235 55593 55699 55701 55703 55707 55709 55712 55714 55716 55718

55720 55722 55726 55728 55729 55731 55733 55734 55736 55737 55739 55741 55743 55744 55746 55748 55749 55751 55753 55754 55757

55759 55760 55762 55763 55765 55810 55812 55813 55815 55817 55818 55820 55821 55823 55828 55830 55832 55836 55837 55839 55868

55873 55875 55877 55920 55945 56107 56109 56111 56113 56123 56125 56127 56129 56131 56132 56134 56135 56157 56165 56171 56179

56186 56192 56200 56207 56213 56220 56228 56235 56242 56250 56256 56264 56271 56277 56284 56291 56297 56304 56312 56318 56326

56429 56431 56433 56436 56437 56438 56440 56565 56567 56568 56570 56581 56582 56589 56592 56594 56596 56597 56599 56606 56670

56672 56674 56694 56700 56703 56706 56708 56710 56711 56713 56715 56716 56718 56719 56722 56725 56728 56732 56734 56736 56737

56739 56740 56742 56743 56745 56746 56755 56756 56758 56760 56761 56763 56794 56796 56797 56798 56800 56802 56804 56805 56807

56828 56829 56832 56834 56836 56839 56841 56842 56844 56845 57056 57057 57067 57258 57260 57266 57268 57269 57271 57272 57274

57275 57276 57278 57279 57280 57282 57284 57285 57287 57289 57291 57293 57295 57297 57299 57302 57304 57306 57308 57310 57311

57313 57314 57316 57317 57319 57324 57326 57327 57329 57331 57332 57334 57336 57338 57346 57348 57350 57358 57360 57362 57431

57524 57526 57528 57542 57544 57546 57547 57549 57555 57557 57558 57587 58024 58030 58032 58034 58035 58038 58039 58041 58043

58045 58047 58050 58052 58053 58054 58057 58058 58059 58061 58063 58065 58067 58069 58071 58072 58074 58077 58078 58080 58081

58083 58084 58086 58087 58088 58090 58091 58093 58094 58095 58097 58101 58102 58104 58106 58108 58110 58112 58114 58115 58117

58118 58121 58123 58124 58130 58132 58134 58136 58138 58140 58142 58143 58145 58147 58149 58150 58152 58154 58156 58163 58165

58166 58168 58170 58172 58174 58176 58178 58180 58182 58184 58185 58187 58189 58191 58193 58195 58197 58199 58200 58202 58204

58206 58214 58216 58218 58220 58225 58227 58229 58372 58374 58430 58432 58449 58451 58460 58462 58472 58474 58476 58485 58487

58545 58547 58549 58550 58552 58554 58555 58556 58558 58560 58562 58563 58565 58566 58568 58570 58572 58573 58575 58577 58583

58585 58586 58588 58590 58595 58599 58601 58602 58604 58606 58612 58616 58617 58619 58620 58622 58624 58625 58627 58629 58631

58633 58636 58638 58640 58642 58644 58646 58648 58650 58652 58654 58656 58658 58660 58662 58663 58664 58666 58667 58669 58670

58672 58674 58675 58677 58679 58681 58683 58684 58686 58688 58690 58692 58693 58695 58697 58699 58701 58702 58704 58706 58708

58710 58711 58713 58715 58717 58719 58721 58727 58729 58730 58732 58734 58736 58753 58762 58764 58806 58808 58810 58881 58882

58883 58884 58885 58886 58887 58888 58890 58892 58894 58896 58898 58900 58902 58904 58906 58908 58909 58911 58913 58915 58917

58919 58921 58923 58925 58927 58929 58931 58933 58935 58937 58939 58940 58942 58944 58946 58948 58950 58952 58958 58960 58962

58964 59168 59170 59172 59174 59176 59179 59180 59182 59184 59188 59386 59388 59417 59419 59421 59423 59425 59428 59430 59432

59434 59435 59437 59439 59441 59443 59445 59447 59448 59450 59451 59453 59456 59458 59460 59462 59464 59466 59467 59469 59471

59472 59474 59476 59477 59479 59481 59483 59485 59486 59487 59489 59491 59492 59494 59496 59500 59501 59503 59509 59511 59512

59515 59517 59519 59521 59523 59525 59527 59529 59532 59535 59536 59544 59578 59580 59582 59583 59605 59615 59617 59619 59627

59629 59631 59633 59640 59642 59644 59646 59647 59649 59651 59653 59654 59656 59658 59660 59661 59663 59664 59666 59668 59670

59672 59674 59677 59679 59681 59682 59684 59688 59690 59692 59694 59696 59698 59699

Table 13: Final list of runs used for this analysis

37608 38744 59701 59702 59704 59705 59707 59709 59710 59712 59714 59716 59736 59738 59739 59741 59743 59745 59749 59751 59753
59782 59785 59787 59789 59793 59795 59797 59799 59802 59803 59810 59813 59816 59829 59831 59832 59834 59836 59838 59840 59842
59843 59847 59851 59853 59855 59857 59860 59862 59864 59868 59870 59872 59876 59878 59880 59882 59884 59886 59888 59890 59892
59894 59896 59904 59906 59908 59910 59912 59914 59916 59919 59921 59923 59924 59926 59928 59930 59931 59933 59939 59941 59942
59944 59946 59947 59949 59951 59953 59954 59955 59957 59959 59960 59962 59964 59965 59967 59969 59971 59972 59974 59976 59978
59979 59981 59983 59985 59987 59988 59990 59992 59994 59995 59996 59998 59999 60001 60005 60007 60009 60011 60013 60014 60016
60018 60020 60022 60024 60026 60028 60030 60031 60033 60035 60037 60039 60041 60043 60045 60047 60049 60050 60052 60054 60056
60058 60060 60062 60070 60071 60073 60074 60076 60077 60079 60082 60084 60087 60089 60091 60093 60095 60097 60098 60100 60101
60103 60104 60106 60108 60110 60112 60114 60116 60118 60120 60122 60124 60125 60127 60129 60138 60139 60141 60142 60144 60146
60147 60149 60150 60152 60153 60155 60156 60158 60159 60161 60163 60164 60237 60238 60294 60300 60302 60303 60305 60306 60308
60310 60311 60313 60315 60316 60320 60322 60324 60327 60329 60337 60339 60341 60342 60344 60346 60347 60349 60351 60352 60354
60356 60357 60359 60361 60362 60364 60366 60367 60369 60371 60373 60374 60376 60378 60380 60382 60383 60385 60387 60388 60390
60392 60393 60396 60398 60399 60401 60403 60405 60407 60409 60410 60412 60414 60416 60418 60420 60421 60423 60425 60426 60428
60429 60431 60433 60435 60436 60438 60440 60441 60443 60444 60446 60448 60449 60451 60453 60455 60456 60458 60460 60461 60463
60465 60466 60469 60471 60473 60474 60478 60479 60481 60483 60484 60489 60490 60492 60494 60495 60497 60499 60500 60502 60503
60505 60508 60511 60512 60514 60516 60517 60519 60520 60522 60524 60525 60527 60533 60535 60536 60538 60539 60541 60543 60544
60546 60548 60549 60551 60553 60556 60557 60559 60561 60562 60564 60565 60570 60571 60573 60574 60576 60610 60617 60619 60627
60629 60631 60633 60635 60637 60639 60671 60673 60675 60677 60679 60685 60686 60688 60690 60691 60693 60695 60696 60698 60699
60701 60703 60704 60706 60708 60709 60711 60712 60714 60715 60717 60719 60720 60722 60723 60725 60727 60728 60730 60731 60733
60735 60736 60738 60740 60741 60743 60746 60747 60749 60751 60752 60754 60758 60759 60776 60779 60780 60782 60783 60785 60786
60792 60794 60796 60798 60800 60827 60859 60861 60862 60891 60894 60905 60907 60918 60919 60921 60922 60924 60925 60969 60970
60979 60982 60984 60986 60989 60990 60992 60994 60995 60997 60999 61003 61005 61006 61008 61010 61011 61013 61015 61020 61022
61023 61025 61027 61028 61030 61032 61033 61035 61037 61038 61040 61042 61043 61047 61048 61050 61052 61053 61055 61057 61058
61060 61062 61063 61065 61066 61069 61070 61072 61074 61075 61077 61079 61080 61082 61083 61085 61087 61088 61090 61092 61093
61095 61097 61098 61100 61103 61104 61113 61114 61116 61118 61119 61121 61127 61129 61131 61151 61154 61524 61525 61527 61529
61530 61532 61534 61536 61537 61539 61542 61544 61546 61548 61549 61551 61553 61555 61556 61558 61560 61562 61563 61565 61567
61569 61571 61572 61574 61576 61578 61579 61581 61583 61585 61586 61588 61590 61592 61594 61595 61598 61606 61608 61609 61611
61613 61615 61617 61618 61620 61622 61624 61625 61636 61638 61641 61642 61644 61646 61648 61649 61651 61653 61654 61656 61662
61664 61665 61667 61669 61672 61674 61675 61677 61679 61681 61682 61684 61686 61687 61689 61691 61693 61694 61696 61698 61699
61701 61703 61706 61798 61800 61801 61803 61805 61813 61814 61816 61817 61819 61821 61830 61832 61833 61835 61837 61838 61840
61842 61843 61845 61847 61848 61850 61852 61853 61855 61856 61858 61859 61861 61863 61864 61866 61868 61869 61877 61879 61880
61889 61891 61892 61894 61896 61898 61900 61902 61904 61908 61909 61911 61913 61915 61917 61919 61920 61922 61924 61926 61928
61930 61931 61933 61935 61941 61943 61945 61947 61949 61951 61952 61954 61956 61958 61960 61962 61964 61966 61969 61971 61973
61975 61976 61978 61980 61982 61984 61986 61988 61989 61990 61992 61993 61996 61997 61999 62001 62002 62004 62006 62008 62009
62011 62013 62015 62017 62019 62021 62022 62024 62026 62028 62030 62032 62033 62035 62037 62039 62041 62043 62044 62046 62048
62050 62052 62054 62056 62057 62059 62061 62072 62074 62076 62078 62080 62081 62083 62085 62087 62089 62091 62093 62095 62096
62098 62100 62102 62104 62106 62108 62110 62112 62113 62115 62117 62121 62123 62124 62127 62128 62130 62132 62134 62135 62139
62140 62143 62145 62150 62152 62153 62155 62157 62159 62161 62163 62165 62166 62168 62170 62172 62174 62176 62178 62180 62182
62184 62187 62189 62191 62192 62228 62230 62232 62234 62236 62240 62241 62243 62245 62247 62249 62250 62256 62258 62260 62261
62263 62267 62269 62270 62272 62276 62279 62281 62283 62285 62286 62288 62290 62291 62293 62295 62297 62298 62300 62302 62303
62305 62307 62309 62310 62312 62314 62315 62319 62321 62322 62324 62326 62328 62329 62331 62334 62336 62338 62340 62342 62344
62345 62347 62349 62351 62352 62354 62355 62357 62359 62369 62370 62372 62374 62376 62378 62380 62382 62384 62386 62388 62390
62394 62396 62398 62400 62404 62408 62410 62412 62414 62416 62418 62420 62426 62429 62432 62434 62436 62438 62440 62442 62444
62446 62448 62450 62452 62454 62456 62458 62460 62462 62464 62466 62468 62475 62477 62479 62484 62486 62488 62489 62491 62498
62500 62502 62506 62508 62509 62511 62513 62515 62517 62523 62525 62527 62529 62531 62533 62535 62537 62539 62541 62543 62545
62549 62551 62553 62554 62559 62560 62562 62565 62566 62568 62570 62572 62577 62579 62583 62585 62589 62596 62599 62601 62602
62610 62612 62614 62616 62623 62625 62629 62631 62632 62634 62636 62638 62642 62644 62645 62647 62649 62651 62653 62655 62657
62659 62661 62663 62668 62670 62672 62675 62677 62679 62681 62683 62687 62689 62693 62695 62697 62699 62701 62703 62705 62707
62714 62716 62718 62720 62722 62724 62726 62728 62730 62745 62747 62749 62751 62753

Table 14: Final list of runs used for this analysis

37608 38744 62755 62757 62759 62766 62773 62780 62782 62784 62786 62788 62789 62791 62794 62796 62798 62807 62811 62812 62815

62817 62819 62821 62822 62824 62826 62827 62829 62831 62832 62834 62836 62838 62839 62841 62843 62844 62846 62849 62855 62857

62859 62862 62863 62865 62867 62869 62872 62875 62877 62906 62908 62911 62913 62915 62917 62919 62921 62922 62924 62926 62930

62931 62933 62935 62937 62939 62941 62943 62945 62947 62949 62951 62953 62955 62957 62959 62962 62964 62966 62968 62969 62971

62973 62975 62977 62983 62985 62987 62989 62991 62993 62995 62997 62999 63001 63003 63007 63009 63011 63013 63015 63017 63019

63021 63024 63026 63028 63030 63032 63033 63035 63037 63039 63041 63043 63045 63047 63049 63051 63054 63056 63058 63060 63062

63064 63066 63068 63070 63072 63074 63076 63078 63080 63082 63083 63085 63087 63089 63091 63093 63095 63097 63099 63101 63107

63109 63111 63113 63115 63118 63120 63152 63168 63178 63204 63206 63208 63210 63213 63218 63220 63222 63224 63226 63228 63230

63241 63243 63245 63247 63249 63259 63261 63263 63265 63267 63275 63277 63279 63281 63283 63285 63287 63289 63291 63293 63338

63340 63344 63345 63346 63348 63350 63388 63390 63392 63393 63395 63396 63398 63400 63402 63404 63407 63409 63411 63413 63415

63417 63419 63421 63423 63425 63427 63436 63519 63521 63523 63525 63527 63529 63531 63532 63534 63536 63538 63539 63541 63542

63543 63544 63545 63547 63548 63550 63552 63554 63555 63579 63735 63736 63738 63740 63742 63744 63745 63747 63749 63766 63768

63770 63772 63773 63842 64074 64076 64077 64079 64081 64083 64085 64087 64088 64090 64092 64094 64096 64098 64100 64101 64110

64113 64114 64116 64117 64119 64121 64123 64124 64126 64128 64130 64132 64133 64135 64136 64138 64140 64142 64144 64146 64148

64150 64151 64153 64155 64157 64159 64161 64162 64166 64168 64178 64192 64196 64198 64305 64334 64367 64403 64404 64409 64413

64415 64417 64419 64423 64424 64426 64428 64430 64437 64439 64440 64442 64446 64448 64450 64454 64455 64489 64491 64493 64495

64497 64499 64500 64502 64503 64548 64558 64574 64576 64577 64592 64600 64602 64604 64606 64608 64609 64611 64613 64615 64616

64619 64623 64624 64626 64627 64629 64632 64634 64636 64637 64638 64640 64659 64662 64665 64666 64668 64688 64690 64692 64739

64741 64743 64744 64746 64748 64750 64751 64753 64755 64756 64758 64760 64772 64791 64793 64795 64797 64801 64803 64805 64807

64877 64879 64882 64884 64887 64889 64890 64892 64893 64894 64895 64898 64902 64903 64905 64908 64910 64911 64913 64914 64915

64917 64918 64920 64921 64923 64924 64926 64927 64929 64930 64933 64935 64937 64938 64940 64942 64944 64946 64947 64951 64952

64954 64956 64958 64960 64965 64967 64969 64971 64972 64974 64976 64978 64979 64981 64983 64984 64986 64987 64989 64990 64992

64993 64994 64996 64997 64999 65000 65002 65004 65005 65007 65008 65010 65011 65013 65015 65016 65018 65019 65021 65022 65024

65025 65027 65028 65030 65031 65033 65034 65041 65047 65048 65050 65052 65054 65055 65059 65061 65063 65064 65066 65068 65069

65071 65119 65120 65122 65123 65126 65133 65135 65136 65138 65139 65140 65145 65146 65148 65149 65150 65152 65153 65154 65160

65176 65177 65178 65180 65181 65183 65184 65185 65187 65188 65189 65191 65192 65193 65195 65196 65198 65199 65201 65203 65205

65211 65212 65214 65215 65217 65221 65226 65228 65229 65231 65239 65244 65246 65247 65254 65256 65266 65269 65271 65283 65284

65291 65296 65315 65317 65319 65321 65323 65325 65326 65328 65329 65331 65332 65333 65335 65336 65338 65339 65341 65342 65344

65345 65346 65347 65349 65350 65351 65352 65353 65355 65356 65357 65358 65360 65365 65366 65368 65369 65371 65372 65374 65376

65378 65379 65381 65383 65384 65386 65388 65390 65393 65396 65398 65400 65402 65404 65406 65407 65410 65412 65414 65415 65417

65419 65421 65423 65425 65427 65428 65434 65436 65438 65440 65441 65443 65445 65447 65449 65453 65457 65459 65461 65462 65464

65465 65467 65469 65471 65472 65474 65475 65477 65478 65480 65482 65484 65485 65487 65489 65491 65493 65494 65495 65497 65499

65500 65502 65503 65505 65506 65508 65509 65511 65512 65518 65520 65521 65523 65525 65527 65528 65530 65531 65533 65535 65537

65539 65540 65542 65544 65545 65547 65548 65550 65551 65552 65554 65555 65556 65558 65559 65561 65563 65565 65566 65568 65570

65572 65573 65575 65577 65579 65581 65583 65585 65587 65588 65590 65592 65593 65595 65597 65598 65600 65602 65603 65605 65607

65609 65610 65612 65613 65615 65617 65619 65620 65622 65624 65625 65627 65628 65630 65632 65633 65635 65637 65638 65640 65642

65643 65645 65647 65649 65651 65652 65654 65656 65658 65660 65661 65667 65669 65671 65673 65675 65676 65678 65680 65682 65684

65685 65688 65690 65691 65693 65694 65696 65698 65699 65701 65702 65704 65706 65707 65708 65710 65712 65713 65715 65716 65718

65719 65721 65722 65724 65726 65727 65729 65730 65732 65737 65740 65742 65743 65745 65747 65748 65751 65752 65754 65755 65757

65758 65760 65762 65765 65767 65768 65770 65771 65773 65774 65776 65779 65780 65782 65784 65786 65787 65789 65790 65792 65795

65796 65798 65799 65801 65803 65805 65806 65808 65809 65811 65813 65814 65816 65817 65819 65821 65854 65856 65858 65860 65862

Table 15: Final list of runs used for this analysis

References

Abreu P.e.a., 2011, Physical Review D, vol. 84, Issue 12 84, 122005

Adrián-Martínez S., Al Samarai I., Albert A., et al., 2012a, Astroparticle Physics 35, 552

Adrián-Martínez S., Al Samarai I., Albert A., et al., 2012b, Journal of Instrumentation 7, 8002

Adrián-Martínez S., Albert A., André M., et al., 2015, ArXiv e-prints

Adrián-Martínez S., Samarai I.A., Albert A., et al., 2012c, ApJ 760, 53

Ageron M., Aguilar J.A., Al Samarai I., et al., 2011, Nuclear Instruments and Methods in Physics Research A 656, 11

Ageron M., Aguilar J.A., Al Samarai I., et al., 2012, The Astrophysical Journal 760

Ajit K. Kembhavi J.V.N., 1999, Quasars and Active Galactic Nuclei: An Introduction, Cambridge University Press

Antonucci, R.R.J Miller J., 1985, ApJ 297, 621

Atwood W.B., Abdo A.A., Ackermann M., et al., 2009, ApJ 697, 1071

B. Povh, K. Rith C.S., 1999, Teilchen und Kerne, Springer

Balbus S.A., Hawley J.F., 1991, Astrophysical Journal 376, 214

Beckmann, V. Shrader C., 2012, Active Galactic Nuclei, Wiley-Vch

Bianchi S., Maiolino R., Risaliti G., 2012, Advances in Astronomy 2012, 17

Blandford R.D., Königl A., 1979, Astrophysical Journal 232, 34

Blumenthal G.R., Gould R.J., 1970, Reviews of Modern Physics 42, 237

Burke B.F., Graham-Smith F., 2009, An Introduction to Radio Astronomy

Carminati G., 2007, ANTARES internal note: ANTARES-Soft/2007-004

Cash W., 1979, ApJ 228, 939

Collin S., Kawaguchi T., Peterson B.M., Vestergaard M., 2006, A&A 456, 75

deVries Uiterweerd G., 2007, Ph.D. thesis, Utrecht University, the Netherlands

Fanaroff B.L. R.J., 1974, MNRAS 167, 31P

Fehn K., 2015, Ph.D. thesis, FAU Erlangen

Folger F., 2014, Ph.D. thesis, FAU Erlangen

Formaggio J.A., Zeller G.P., 2012, Reviews of Modern Physics 84, 1307

Fossati G., Celotti A., Ghisellini G., Maraschi L., 1997, In: Ostrowski M., Sikora M., Madejski G., Begelman M. (eds.) Relativistic Jets in AGNs., p.245

Fukuda S., Fukuda Y., Ishitsuka M., et al., 2001, Physical Review Letters 86, 5656

Gaisser T.K., 1990, Cosmic rays and particle physics, Cambridge University Press

Gandhi R., Quigg C., Hall Reno M., Sarcevic I., 1996, Astroparticle Physics 5, 81

G.B. Rybicki A.L., 1985, Radiative Processes in Astrophysics, John Wiley & Sons

Heijboer A., 2004, Ph.D. thesis, Amsterdam

IceCube Collaboration 2013, Science 342, 1

Ingelman G., Edin A., Rathsman J., 1997, Computer Physics Communications 101, 108

Jackson J., 1998, Classical Electrodynamics, John Wiley & Sons

Jong M.D., 2009, ANTARES internal note: ANTARES-SOFT-2009-001

Kadler M., Ojha R., TANAMI Collaboration 2015, Astronomische Nachrichten 336, 499

Katz U.F., Spiering C., 2012, Progress in Particle and Nuclear Physics 67, 651

Khachikyan É.Y. W.D., 1971, Astrophysics 7, 231

Krauß F., Kadler M., Mannheim e.a., 2014, Astronomy & Astrophysics 566, L7

Kremers C., Chigrin D.N., Kroha J., 2009, Physical Review A 79, 013829

Krolik J., 1999, Active galactic nuclei : from the central black hole to the galactic environment, Princeton University Press

Lawrence A., 1987, PASP 99, 309

Leo W., 1994, Techniques for Nuclear and Particle Physics Experiments, Springer-Verlag New York Inc

Mannheim K., 1993, Astronomy and Astrophysics 269, 67

Mannheim K., Protheroe R.J., Rachen J.P., 2001, Physical Review D vol. 63, Issue 2, id. 023003 63, 023003

Meyer E.T., Fossati G., Georganopoulos M., Lister M.L., 2011, ApJ 740, 98

Mücke A., Protheroe R.J., Engel R., et al., 2003, Astroparticle Physics 18, 593

Müller C., 2014, Ph.D. thesis, FAU Erlangen

Ojha R., Kadler M.e.a., 2010, A&A 519, A45

Okada A., 1994, Astroparticle Physics 2, 393

Peterson B., 1993, PASP 105, 247

Rivière C., 2012, ANTARES internal note ANTARES-PHYS-2012-001

S. Navas L.T., 2011, ANTARES internal note: ANTARES-Soft-1999-011

Schnabel J., 2010, Diploma thesis, FAU Erlangen

Schneider P., 2008, Einführung in die Extragalaktische Astronomie und Kosmologie, Springer Berlin Heidelberg New York

Seyfert C., 1943, ApJ 97, 28

Shakura N.I., Sunyaev R.A., 1973, A&A 24, 337

Shu F., 1991, The physics of astrophysics. Volume 1: Radiation, University Science Books

Stanev T., 2010, High energy cosmic rays, Springer

Stecker F.W., Done C., Salamon M.H., Sommers P., 1991, Physical Review Letters 66, 2697

Terzian Y., Khachikian E., Weedman D., (eds.) 1999, Active Galactic Nuclei and Related Phenomena, Vol. 194 of IAU Symposium, IAU Symposium

The ANTARES QB working group, ANTARES Wikipage: http://antares.in2p3.fr/internal/dokuwiki/doku.php?id=quality_flags

Urry C.M., Padovani P., 1995, PASP 107, 803

10 Acknowledgments

At this point I would like to thank all the people who supported me during this thesis. Without them, this work would no be possible at all.

Firstly, I thank Prof. Dr. Matthias Kadler for drawing my interest on active galactic nuclei and neutrino physics. He gave me the opportunity to start the first ANTARES master thesis in Würzburg and was always available for discussions. I also want to thank Matthias for allowing me to participate in several ANTARES Collaboration meetings and for letting me become a member of the Collaboration. At this point I want to thank the head of the astronomy chair of Würzburg Prof. Dr. Karl Mannheim for giving me the chance of performing this project here in Würzburg. Many thanks also to Prof. Dr. Gisela Anton for all her support in respect to this project.

I thank Dr. Kerstin Fehn for supervising and introducing me into all steps of the analysis. She was always available to support me in any kind of problem that came up.
I also want to express my thanks to Dr. Thomas Eberl and Dr. Clancy James for all the regular meetings we had and all the support in any stage of this project.
I thank Dr. Cornelia Müller for supporting me with the source selection part and always being available for discussions.

Many thanks goes to Stefan Geißelsöder, Dr. Oleg Kalekin, and Dr. Kay Graf for the great introduction to the ANTARES shift. In addition, I want to thank Jannik Hofestädt, Steffen Hallmann, Robert Schulz, Jonas Trüstedt, and Marcus Langejahn for supporting me in any technical problem that occurs. I thank Paul Ray Burd for explaining the concept of VLBI to me. Thanks also to my office colleague Rosamunde Pare and the entire group of Würzburg and Erlangen for the sympathetic atmosphere.

Many thanks goes to all the prove readers of this thesis: Prof. Dr. Matthias Kadler, Dr. Dorit Glawion, Dr. Thomas Eberl, Dr. Clancy James, Dr. Cornelia Müller, Jannik Hofestädt and Rosamunde Pare.

I also want to express my gratitude to Viktor Lackmann, who organized and payed attention of my car. Without his afford, such a strong cooperation with Erlangen wouldn't be possible. Finally, I deeply want to thank my entire family and love Jennifer Wolf for always supporting me during this thesis and my whole time at university. Without their strong support, I would not be able to get so far and become a part of actual research in astronomy and particle physics.

Erklärung

Hiermit erkläre ich, diese Arbeit selbstständig und nur unter Verwendung der angegebenen Quellen und Hilfsmittel verfasst zu haben. Zudem versichere ich, diese Arbeit keiner anderen Prüfungsbehörde zur Erlangung eines akademischen Grades vorgelegt zu haben.

Würzburg, den 21. August 2015

Unterschrift: _____